Crystallization of Diammonium Tartrate Salts on Self-Assembled Monolayers of Cysteine on Au (111)

by

Kelly L. Hannah
B.Sc., University of Regina, 2001

A Thesis Submitted in Partial Fulfillment of the
Requirements for the Degree of

MASTERS OF SCIENCE

in the Department of Chemistry

University of Victoria

Supervisor: Dr. Alexandre G. Brolo

ABSTRACT

The properties of crystals formed in biological systems are regulated by organized organic surfaces of biopolymers (biomineralization). Self-assembled monolayers (SAMs) are highly organized systems that can be utilized as an organic interface to template the nucleation and growth of crystals, mimicking the biomineralization process. In this work, SAMs of L and DL-cysteine on ultra thin Au (111) films have been used to investigate the crystallization patterns of diammonium tartrate salts. Different aspects of the SAM, such as quality and geometry, have been characterized using a polarization modulation infrared reflection absorption spectroscopy (PM-IRRAS). Crystallizations using both the racemic and pure forms of diammonium tartrate have been undertaken to identify and distinguish between the various crystal types. Successful crystallization on SAMs has yielded numerous, well-defined crystals. Crystals grown on the monolayer covered slides were analyzed using X-ray powder diffraction (XPD), scanning electron microscopy (SEM) and polarimetry. Crystal growth simulations were conducted to model the growth from selected crystal faces. The specific interactions that occur between the diammonium tartrate salts and the cysteine monolayers were studied at the molecular level. Supramolecular bonding theories for the systems studied have been proposed herein. Preferential crystal growth favouring one enantiomer of diammonium tartrate has been identified by polarimetry and the reasoning for the separation is discussed.

Table of Contents

List of Tables

List of Figures

Acknowledgments

I would like to express my gratitude to Dr. Alexandre G. Brolo for his support in various aspects of my project. Thank you to Christopher Addison and Aaron Sanderson for their technical support. I wish to offer special thanks to Bryan Kovisto for his external insight.

Dedication

I would like to dedicate this thesis to all of my family and friends. To my mother for her constant emotional support, continued financial support, friendship and for being my biggest fan. To my brother for his encouragement, faith, and advice. To my grandmother, for her endless love and prayers. To my aunt, for cheering loud enough so I could hear from a distance and for always advising me on the next step. To my uncle, for loving me as teenager and respecting me as an adult. To Peter for his strength. To Jennifer for her love and perspective. To Dr. Tanya Dahms for her guidance.

1 Introduction

The hypothesis for the origin of life rely on the concept of homochirality[1,2]. “Most biomolecules are chiral, but only one enantiomeric form occurs in nature. Life is based on L-amino acids and D-sugars rather than the D-amino acids and L-sugars”[2]. “Among the most promising, yet little explored, avenues for chiral molecular discrimination is adsorption on chiral crystalline surfaces; periodic environments that can select, concentrate and possibly even organize molecules into polymers and other macromolecular structures”[3].

The objective of this research was to exploit the abilities of a chiral self assembled monolayer (SAM) to achieve enantiomer-selective crystallization of the organic salt diammonium tartrate. Another major goal of the research was to better understand the supramolecular system formed between crystals and amino acid monolayers. Background information on SAMs, crystallization, and on how they are related to each other is presented in Chapter 2. We demonstrated that SAMs can control the crystallization and whether or not enantiomer-selective crystallization could exist on the chiral monolayer.

The approach to the entire research project was to bring together ideas from many areas and combine them, as opposed to working in succeeding steps from one stage to the next. The design of the experimental aspect of this research is detailed further in Chapter 3. The principles of each experimental method, such as polarization modulation infrared reflection absorption spectroscopy (PM-IRRAS), scanning electron microscopy (SEM), and X-ray powder diffraction (XPD) are highlighted in Chapter 3.

Ultimately, to explain the supramolecular system as a whole, an understanding of the relationship between the SAMs and the diammonium tartrate crystals evolved. The spectra obtained from PM-IRRAS confirmed the presence and organization of the monolayers. The SEM images provided insight into the orientation of the crystals relative to the monolayer, which in turn was used to model the supramolecular interactions that occur between the crystal and monolayer systems. As well, SEM images provided a better visualization of the depth and direction of the visible crystal faces. An aspect crucial to understanding the supramolecular system in question was the orientation of the crystal relative to the monolayer. To accomplish this, the crystal faces from which the crystal growth occurs must be known. Therefore, an external laboratory carried out an X-ray diffraction study of the crystals formed on the Au (111) surface and those formed in solution. The X-ray data emphasize the effect the monolayer has on crystal growth.

With data acquisition and processing complete, the results were explained using crystal growth simulations. The XPD results provided insight into the relative growth rates of the individual crystal faces. The simulated crystals were cross referenced to the crystal images acquired through optical microscopy and SEM. The matching between the simulated data and the experimental data indicated the probable face of interaction between the crystals and the cysteine monolayers. Steric effects, hydrogen bonding and van der Waals forces were then considered when examining the face-selective crystallization of each supramolecular system relative to the unit cells for the compounds. Polarimetry experiments were conducted on the crystals removed from the slides. These experiments gave a final indication that the cysteine monolayers can selectively crystallize one enantiomer from a racemic solution. The results and a discussion pertaining to this analysis are presented in Chapter 4 and the conclusions drawn from this research are summarized in Chapter 5.

2 Background

2.1 Self Assembled Monolayers

Molecular self-assembly is defined as the spontaneous emergence of highly organized functional supramolecular architectures from single components of a system under certain external conditions[4]. Such conditions may include, for example, a suitable template, where molecules can adsorb. In contrast to molecular chemistry, which has established its power over the covalent bond, non-covalent intermolecular forces prevail in this field[5]. The energetic and stereochemical properties of non-covalent intermolecular forces such as electrostatic interactions, van der Waals forces and most prominently, hydrogen bonding, act in a manner such that they direct the monomeric building blocks spontaneously into supramolecular structures with inherent higher order. The two dimensional form of these higher order structures are known as self-assembled monolayers (SAMs), which have a variety of potential applications in fields ranging from biosensors to microelectrode arrays[6-11].

2.1.1 Introduction

Certain organic molecules spontaneously form a single layer of a well-organized and highly-oriented, two-dimensional system[12]. Organized monolayers can be fabricated by either spreading an amphiphilic molecule in an air-water interface (Langmuir-Blodgett method)[13] or by spontaneous adsorption (chemisorption) of thiols onto metallic substrates (self-assembled monolayer (SAM) method)[14]. SAMs are highly organized systems based on the interactions between organic chains of *n*-length of the type $HS-(CH_2)_n-X$ (ω-terminated alkanethiols) and metallic surfaces. Single crystal gold and silver surfaces are generally employed for the preparation of SAMs because they interact strongly with the thiol group. Each individual chain that makes up the SAM contains three parts. These are the head group, carbon linker and the tail group, as seen in Figure 2-1. The head group is a mercapto group (HS-) capable of binding to the metallic surface (gold or silver). The carbon linker (spacer) is a chain of methylene units (CH_2-). The tail, or terminal, groups (-X) may include several functionalities such as alcohols (-OH), carboxylic acids (-COOH), hydrocarbons ($-CH_3$) and amino ($-NH_3$) moieties. The reactivity and interfacial properties of these SAM-modified surfaces can be predetermined by controlling the chemical nature of the group –X. Therefore, selection of a SAM can be tailored to suit the specific needs of an experimental design or application through the variability of the length of carbon spacer and the tail group.

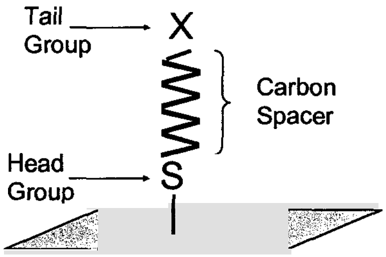

Figure 2-1 - Representation of a single ω-terminated alkanethiol adsorbed on a metallic substrate

The possibility of tailoring surface properties makes SAMs ideal model surfaces for fundamental surface chemistry investigation[15] and long range electron transfer[16,17]. "As model surfaces, self-assembled monolayers (SAMs) must fulfill at least three requirements: (1) to be strongly attached to the substrate, so that surfaces will withstand environmental chemical and physical effects; (2) to be homogenous and closely packed, so that model surfaces will have a given, well-defined composition, and (3) to allow for a diverse range of surface functionality groups to be present"[4]. These properties also render SAMs suitable for several possible applications in analytical chemistry (development of selective sensors) [6-11], electrocatalysis [18-20], corrosion [21-23] and nanotechnology [24-26].

2.1.2 Structure of Self Assembled Monolayers

The notation of Miller indices and overlayers is key to the understanding the structure of SAMs. The Miller notation will be discussed in detail in Section 2.2.6. The reader who is not familiar with Miller indices should consult Section 2.2.6 prior to the following introduction regarding SAMs' structure. Information on the notation used for overlayers can be found elsewhere [27].

2.1.2.1 Surface structure and overlayers

The surface of Au (111) consists of tightly packed hexagons of gold atoms. Once the surfaces are flame annealed, they show a (22 x √3) reconstruction. Although there have been a number of overlayer structures proposed for molecules adsorbed on Au(111), the most common and generally accepted arrangement for alkanethiols is the (√3 x √3)R30° hexagonal lattice with an average spacing of ~5.0 Å between the alkane chains[14] (this arrangement is shown in Figure 2.2). Variations in the twist of the alkane chains, a conformational change that will be discussed in section 2.1.2.2, can lead to extended superstructures[28]. The (√3 x √3)R30° adlayer has been identified through many techniques including infrared absorption (IR)[29], electrochemistry[30], low energy helium diffraction[31], scanning tunneling microscopy (STM)[32,33] and atomic force microscopy (AFM)[34].

2.1.2.2 *Sulfur/Gold Binding in Self Assembled Monolayers*

Monolayers comprised of long-chain hydrocarbons bound to a gold surface via a sulfur containing head group are perhaps the most widely studied of organic thin film systems. The properties of the gold substrate play an important role in determining the overall properties and performance of the monolayer systems [35-37]. These systems were widely investigated under electrochemical control, where the interfacial electric field influences such elements as molecular orientation, binding of head groups and adsorption properties[29].

The head group strongly attaches to the metallic surface so that the modified surface withstands environmental, chemical and physical effects. Evidence of this strong attachment can be seen quantitatively because the alkyl chains do not pack as densely as possible. Energetically, the bond formed between the gold and the sulfur head group is so strong that it is preferred over the situation where there are maximum interactions between alkyl chains due to a maximum packing density on the surface. The binding energies have been determined to be on the order of 120 kJ/mol[38], indicating a strong interaction with the surface. The self-assembly process of ω-terminated alkanethiols on Au is initiated by strong chemical interactions between the sulfur head group and the Au surface, and is believed to result in the chemisorption of the molecules, according to equation 2.1[39].

$$\mathrm{RSH} + \mathrm{Au} \rightleftharpoons \mathrm{RS\text{-}Au} + \mathrm{H}^{+} + e^{-} \quad (2.1)$$

As indicated in equation (2.1), the hydrogen atom of the thiol group is lost and the sulfur atom is oxidized by one electron upon adsorption at Au surfaces[40]. The basis for self-assembly of thiols on single crystal metallic surfaces is that the polar head groups specifically interact with the substrate or chemically bind to it. This, as well as the fact that the self assembly process is spontaneous, implies that such monolayers have an inherent stability[41].

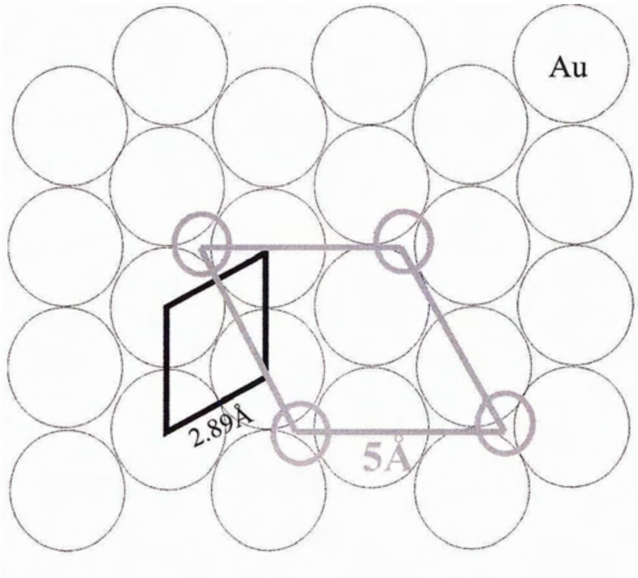

Figure 2-2 - Schematic representation of SAM on Au (111) surface. Grey circles indicate 3 fold hollow sites of sulfur adsorption. The SAM overlay is arranged in a (√3x√3) R30° structure and depicted in grey. The unit cell of the Au (111) is also indicated in black.

When the SAM binds to the surface it does so in a regular pattern dictated by the topography of the surface. The strong interaction of the thiol with the Au forces the alkyl chain to bind in a manner that is commensurate with the Au atoms of the surface[42]. The basic lattice spacing of Au (111) is 2.89Å while the head groups of the thiolate (S^-) groups will bind with a distance of 4.99 Å apart from one another[43]. Each thiolate of the SAM will spontaneously bind to a three fold hollow site on the Au (111) surface[44], as depicted in Figure 2-2. The thiolates will bind specifically to the hollow sites on Au (111), which are more energetically favored (~25 kJ/mol) than the "on top" sites[45]. In particular, a number of STM studies at the molecular level revealed that monolayers at saturation surface coverage have a simple hexagonal √3 x √3R30° overlayer on Au(111)[46].

2.1.2.3 *Intermolecular Interactions in Self Assembled Monolayers*

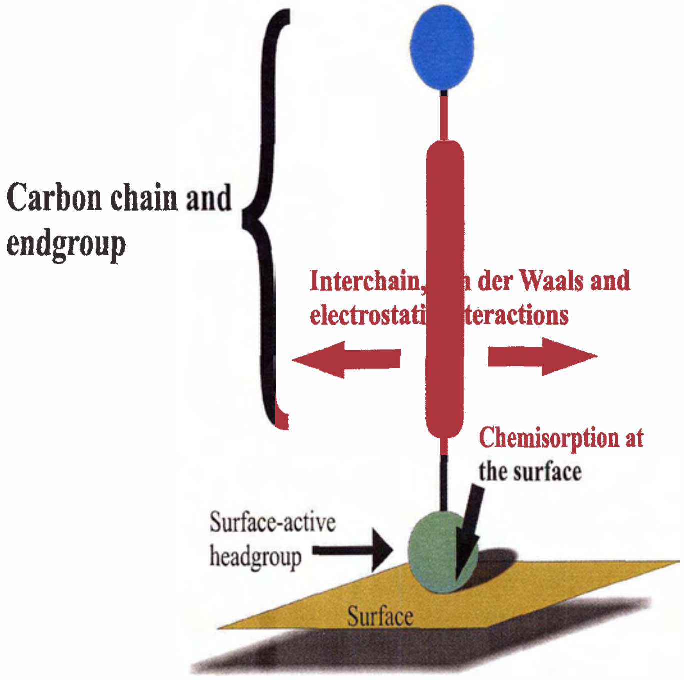

Figure 2-3 - Illustration of forces within a SAM

"In addition to surface-adsorbate interactions, the packing arrangement and ordering of ω-substituted thiols is influenced by the interactions between both the alkyl chains and the end groups"[47]. The spacing of the adsorbed head groups plays an important role in dictating the ability of the rest of the alkyl chain to interact. The spontaneous adsorption of molecules on the surface brings the alkyl chains close enough to allow for short range interactions including electrostatic, hydrogen bonding and other van der Waals forces. Steric effects are as well of significant importance to the packing arrangement of a SAM. A summary of the forces within a SAM is depicted in Figure 2-3. Evidence for the stabilization of a SAM through intermolecular interactions was obtained from a variety of approaches. Molecular modeling attributes the shift of the calculated pK_a of ω-carboxylalkanethiol monolayers to a stabilization due to hydrogen bonding between the terminal functional groups[48]. Evidence for an increase in monolayer stabilization in the adsorbed state of 0.65 kJ/mol per CH_2 group was presented by Jung et al[49].

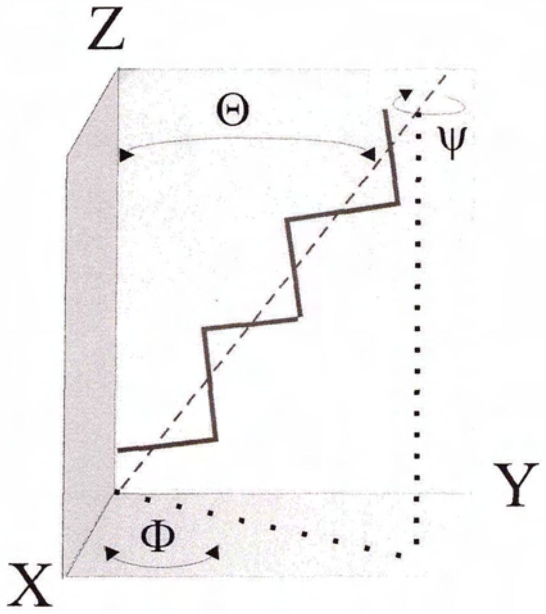

Figure 2-4 - Three dimensional representation of a single alkyl chain adsorbed to a surface. The orientation is defined by the angles tilt (Θ), cant (Ψ) and splay (Φ).

Figure 2-4 represents a schematic of a typical long chain alkanethiol molecule adsorbed on a metal surface in a SAM. As shown in Figure 2-4, the geometry of each alkyl chain contained within the monolayer and therefore the monolayer itself, can be described by a tilt angle, Θ, defined as the angle between the molecular axis and the normal to the surface in the plane containing the zigzag carbon, an angle of chain twist (or cant angle), Ψ, defined as the rotation of the plane containing the zigzag chain along the chain axis and the splay angle, Φ, defined as the rotation of the carbon chain in relation to the substrate.

The inter- and intra-chain forces depend on both the chain length of the alkyl group and on the packing density of the SAM. As the number of units in the alkyl chain increases, the overall interaction ability for forces such as van der Waals is directly increased. As indicated earlier, the energetic stabilization attributed to each CH_2 group in monolayer chain is 0.65 kJ/mol[49]. Although SAMs can have any chain length, a length of n = 10 is the lower limit for SAMs to form commensurate with the Au surface. Below this limit, the overall tilt direction of the SAM begins to shift further away from being commensurate with the surface, resulting in a more strained packing density.[50] The shift from commensurability is indicative of the role chain length has on tilt angle and subsequently the overall physical characteristics of the monolayer.

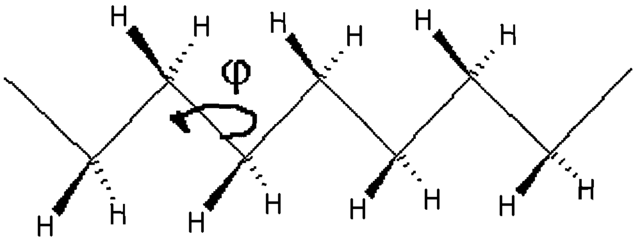

Figure 2-5 - Polyethylene in the all-trans conformation. The location of the dihedral angle, φ, is indicated.

Interchain interactions also play an important role in the values of the tilt (Θ) and splay (Φ) angles of each alkyl chain and subsequently, the overall monolayer structure. In the initial stages of monolayer adsorption, the sulfur head groups chemisorb to the surface in the preferential formation described above in 2.1.2.2, since this is the strongest individual force in the adsorption process. Once the sulfur groups are fixed to the surface, the alkyl chains will attempt to form the most energetically favorable conformation possible. Due to energetic processes, three main conformational forms, all-trans, gauche plus and gauche minus conformations, are possible. The all-trans conformation, as seen in Figure 2-5, occurs with a dihedral angle of $\varphi = 180^\circ$. SAMs made of flexible alkyl derivatives can rearrange the terminal-chains.[4] These are the gauche plus and gauche minus conformations, with $\varphi = 240^\circ$ and $\varphi = 120^\circ$. These conformational changes will enable the most desirable interactions to be formed. The most stable monolayer formed from long chain alkanethiols present the methylene chain tilted at $\theta \cong 30^\circ$.[51] The overall tilt of the monolayer allows for the maximization of van der Waals contact.

The moieties that are present at the end of each alkyl chain as well play an important role in defining the supramolecular structure of the monolayer. The size of the end group may directly affect the packing of the monolayer[52,53]. Any polar or aromatic end groups will result in attractions and repulsions based on either ionic properties, or π-bonding in the case of conjugated rings[54,55].

2.1.2.4 *Self Assembled Monolayers of cysteine in Au (111) surfaces*

In this work, the focus has been on SAMs of L-cysteine and DL-cysteine. Cysteine is a short chain amino acid with the composition $HS\text{-}CH_2\text{-}CH\ (COOH)\ NH_3$. In a SAM of cysteine, the amino and carboxyl groups exist in zwitterionic form at pH $\cong$ 7[56,57]. The surface structure of L-cysteine is interesting because it incorporates a variety *of intermolecular forces, such as hydrogen bonding and electrostatic interactions.* These intermolecular forces have the ability to govern the packing on the surface.

Electrochemical STM has been used by Dakkouri et al. to observe the adlayer structure of L-cysteine on Au(111)[33]. They found that the adlayer exhibits a $(\sqrt{3} \times \sqrt{3})$ R30° structure, as commonly observed for other SAMs. In addition to the $(\sqrt{3} \times \sqrt{3})$ R30° adlayer structure, a number of other adlayers have been identified for the cysteine monolayer adsorbed onto Au (111). Zhang et al. observed that the adlayers of L-cysteine exhibit highly ordered network-like clusters with a $(3\sqrt{3} \times 6)$ R30° structure[58]. Xu et al. have proposed that L-cysteine adsorbs to the surface with a (4×7)R19° adlayer[59]. It is clear that the structure of the cysteine monolayer is strongly dependent on the experimental conditions[33,60,61]. The $(\sqrt{3} \times \sqrt{3})$R30° surface structure for cysteine on Au(111) was proposed for experimental conditions that were similar to the ones used in this thesis[33].

2.2 Crystallization and Crystal Growth

The formation of a crystal depends on both thermodynamic (solubility of the compound) and kinetic properties (nucleation and growth roles)[62]. Crystal growth involves a phase change from either a gas or liquid to a solid. Crystal growth can be roughly divided into three stages: nucleation, growth and termination of growth.

2.2.1 Nucleation

The spontaneous appearance of a new phase, the solid phase in the case of crystallization, occurs when a system is in a nonequilibrium state and the departure from the equilibrium is sufficient for the appearance of such a phase. The formation of a new phase should bring the system to an equilibrium state[63]. In the initial stage in crystallization, formally called nucleation, the formation of aggregates occurs, to which more material will be added in subsequent steps. In the process of nucleation, newly formed aggregates are considered nuclei due to their definite volume and the boundary they form between the new and old phases. Prior to this stage, there is continuous formation and dissolution of ionic or molecular clusters in equilibrium.[64]

A submicroscopic nucleus will form by the chance association of several molecules in solution once enough molecules have come together to reach a "critical size". The critical size stage of crystallization is a period where the volume free energy of the aggregate begins to dominate over unfavorable surface energies resulting in a sustainable nucleus upon which crystal growth occurs[62]. The unfavorable surface energies arise because the molecules from the solution phase tend to dissolve back into the solution[65]. Once the attractions between the molecules in the aggregate energetically exceed the tendency for the dissolution of the cluster, nucleation will ensue. These molecules have approached each other in appropriate orientations and have formed an aggregate. Once nucleation occurs, irreversible crystal growth may ensue.[64] In crystallization from solutions, nuclei can only be formed from supersaturated solutions, which will be a topic discussed in section 2.2.3.

Further material can then be adsorbed and aligned on the surface of this nucleus, giving rise to ordered growth, and the formation of a crystal. The probability that this crystal will grow depends on several factors, including the concentration of the solute, the temperature, the nature of the chemical species that cause precipitation of material from solution, and the pH.

2.2.2 Growth

Crystal growth and nucleation are dynamic processes. This means that when a molecule or ion approaches the growing crystal, it may either remain there or leave. When additional components reach the surface, they must interact with this surface in the appropriate orientation if they are to remain adsorbed and support the formation of a crystal. The greater the number of specific interactions that each component forms as it settles on the growing crystal, the more tightly it will be bound, the lower the energy and the greater the stability of the conglomerate or crystal. A molecule or ion is particularly likely to remain if it is bound at steps or edges such as concave regions at the protrusions and pits on the surface of a crystal[62]. In this case there is the possibility of a larger number of interactions than would occur on a flat surface, as seen in Figure 2-6. It is easier for a molecule to add to and remain on the steps of partially formed layers than it is for it to attach itself to an edge or initiate the formation of a new layer.

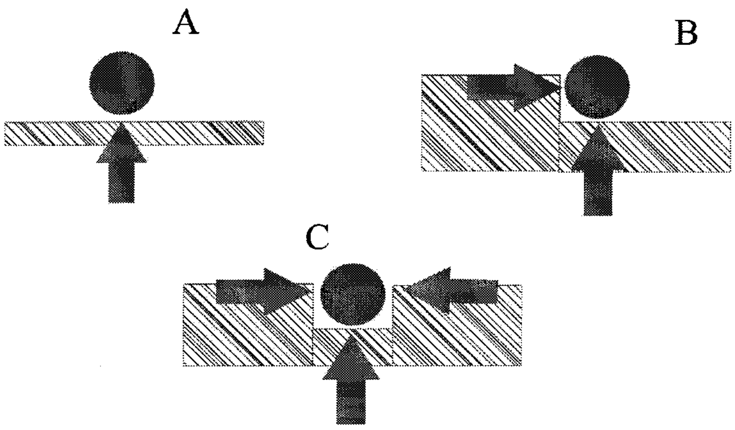

Figure 2-6 - Surface interactions (arrows) for a molecule (represented by a filled circle) preparing to bind to a surface. Image A shows little surface/molecule interaction. Images B and C show increased surface/molecule interaction and are the situation in which a molecule is likely to bind to the surface of a forming crystal.

High quality crystals are obtained when the rate of deposition of material from the solution is appropriately balanced with respect to several parameters such as time, temperature, etc. A high deposition rate may lead to crystal defects, rapid growth in too many directions, and the formation of dendritic (see section 2.2.4) crystals. The rate of diffusion of molecules into the region of crystal growth will influence the growth rate. When a new molecule is bound to a crystal face, energy is released and transferred to neighboring molecules. The rate at which this energy is dissipated is yet another factor in crystal growth. When material is deposited on a crystal face there is a temporary depletion of material in that region of the solution. Thus, while crystal growth is generally faster at lower temperatures, the solution often becomes too viscous at low temperatures; the growth rate will be decreased because molecular travel to growing crystal face is inhibited.

2.2.3 Supersaturated Solutions

If nucleation was thought of as a chemical reaction, then it would have an activation energy that would act as a barrier to crystal formation. So in order to achieve spontaneous crystal formation, this barrier must be overcome. One way to do this is the creation of supersaturated solutions as a crystallizing medium.[64] A solution whose concentration is higher than that of a saturated solution is said to be supersaturated at a given temperature. In contrast to normally stable unsaturated and saturated solution, supersaturated solutions tend to be very unstable.

In crystallization from solutions, the formation of nuclei occurs only in the supersaturated state[66]. One method of crystallization from supersaturated solutions involves the slow cooling of a solution that has been heated to increase the solubility of the solute. This method can be effective in producing crystals if the compound is more soluble at higher temperatures. If the rate of cooling is too rapid then microcrystals may form because an increased number of nuclei will be favored thermodynamically due to energy loss of the solution to the surroundings in the form of heat. In comparison, with a slow rate of cooling, diffusion controlled crystal growth will be favored and larger crystals will be the result. Another method that is useful in producing high quality crystals, especially in the case of small molecules, is slow solvent evaporation from a solution[62]. Single component solvent evaporation methods depend on the removal of solvent in order to obtain the nearly supersaturated solution required for crystallization to occur. A third method of crystallization is achieved through vapor diffusion[62]. In this method, a solution is placed in a small, open container that, in turn, is placed in a larger container with a small amount of a miscible, volatile nonsolvent. The nonsolvent diffuses via the vapor phase into the solution, and saturation or supersaturation is achieved, producing crystals of the newly formed phase. An alternative method is to allow the two liquid phases (the solution and a nonsolvent) to diffuse directly into each other[62]. These three methods are amongst many experimental methods that employ subtle changes to solution conditions to produce high quality crystals.

2.2.4 Dendritic Crystal Growth

Under certain conditions, frequently when growth is rapid, some substances develop a branching tree-like structure referred to as dendritic growth[67]. If a growing crystal cannot dissipate heat fast enough, it can adjust its surface area to optimize heat dissipation and hence, takes on the dendritic form[64]. A common example of a crystal growing in this form is the snowflake, in which the "arms" of the snowflake branch out contributing to each snowflake's individuality. Dendritic crystal growth plagues the crystal engineering process and is evidence of unfavorable crystallization conditions.

2.2.5 Enantiomorphs and Chirality

Isomers are different compounds that have the same molecular formula. They can be divided into two main groups: (a) structural isomers, in which the constituent atoms are connected differently; (b) stereoisomers, which differ only in the spatial arrangement of their constituents. Stereoisomers can be further divided into two groups: enantiomers and diastereomers.

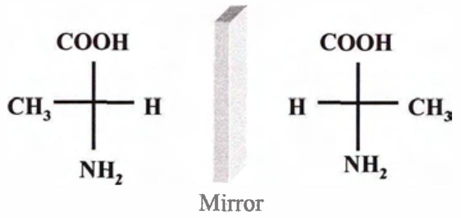

Enantiomers of alanine

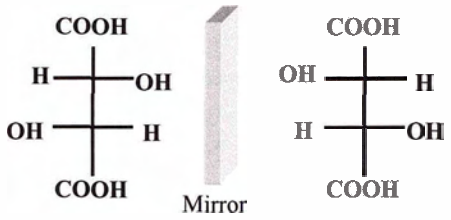

Enantiomers of tartaric acid

Figure 2-7 - Fischer projections of chiral enantiomers for alanine and tartaric acid

Enantiomers are mirror images of one another and diastereomers are not. Enantiomers have identical physical properties with one another with the exception of optical activity, the ability to rotate the plane of polarization of plane-polarized light. One form will rotate to the right (dextrorotatory) and the other to the left (laevorotatory). Molecules and substances that exhibit optical activity are generally described as chiral. Chiral crystals have neither planes of symmetry nor a center of symmetry. Examples of compounds which have chiral enantiomers are highlighted in Figure 2-7 and indicate the mirror image relation present between enantiomers. Diastereoisomers are stererisomers that are not related as mirror images. An example of a diastereoisomer is present in Figure 2-8.

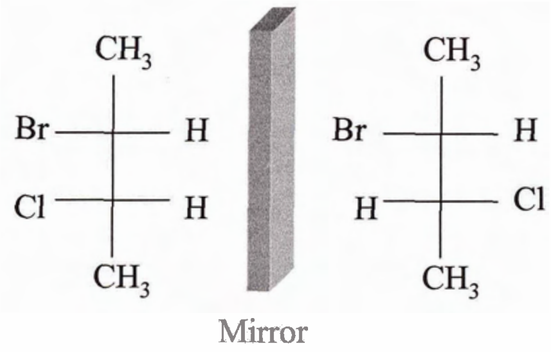

Diastereomers of 2-bromo-3-chlorobutane

Figure 2-8 Fischer projections of diastereomers for 2-bromo-3-chlorobutane

2.2.6 Crystal Classification

The method of classifying a crystal shape, including its faces and the angles between them, is called morphology. The formation of the faces on a crystal depends on the internal atomic structure and the interaction of the surface of the crystal with other molecules during growth. The internal atomic structure is more closely related to the crystal form, "form" is a term that describes a group of crystal faces, all which are related by the elements of symmetry and display the same chemical and physical properties because all are underlain by like atoms in the same geometrical arrangement. The form of a crystal is denoted by being placed between a set of brackets. For example, the 111, 1-11, 11-1, -111, and -11-1 planes in a crystal can all be labeled with the notation (111).

The term crystal habit is used to denote the external shape of a crystal. The shape is influenced by the need to attain a minimum total surface free energy for the volume of the crystal. This is the reason that a small drop of liquid will be spherical. A crystal may tend toward a spherical shape if all faces of the crystal grow with exactly equal rate. This is not generally the case and the development rates of various crystal faces are affected by experimental conditions. However, these rates are significant because they will determine the overall shape of the crystal, which illustrates the relation between the thermodynamic and kinetic factors in crystal growth. A crystal is bounded by the faces that grow the most slowly. If the crystal grows more rapidly in a direction perpendicular to small corner faces than in a direction perpendicular to the other faces, the small corner faces will eventually disappear, as shown in Figure 2-9.

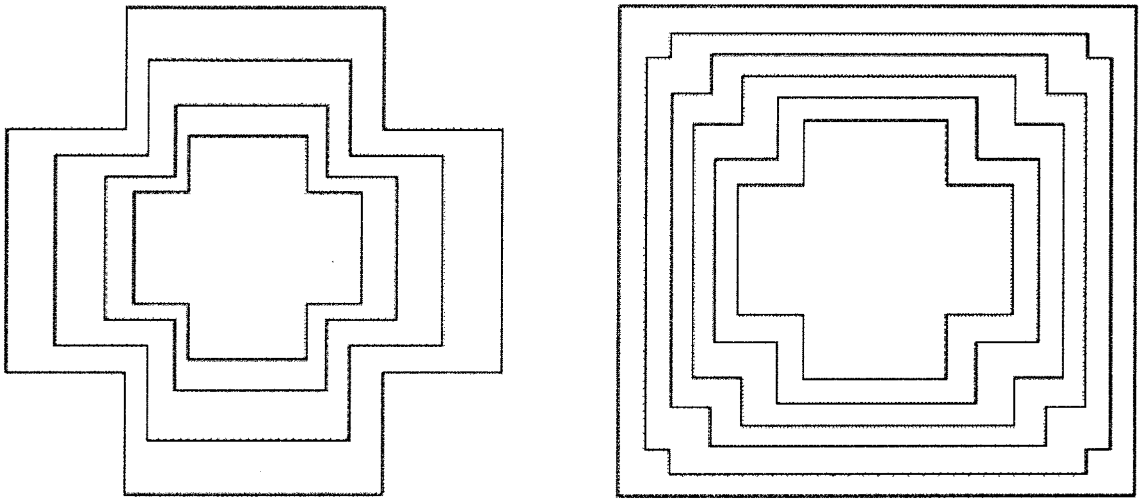

Figure 2-9 - These images depict the growth rings of crystals due to rates of growth. On the left, all faces of the crystal have grown at the same rate and the crystal shape remains the same. On the right, the faces that are initially larger grow slower than the corner crystal faces, which eventually disappear.

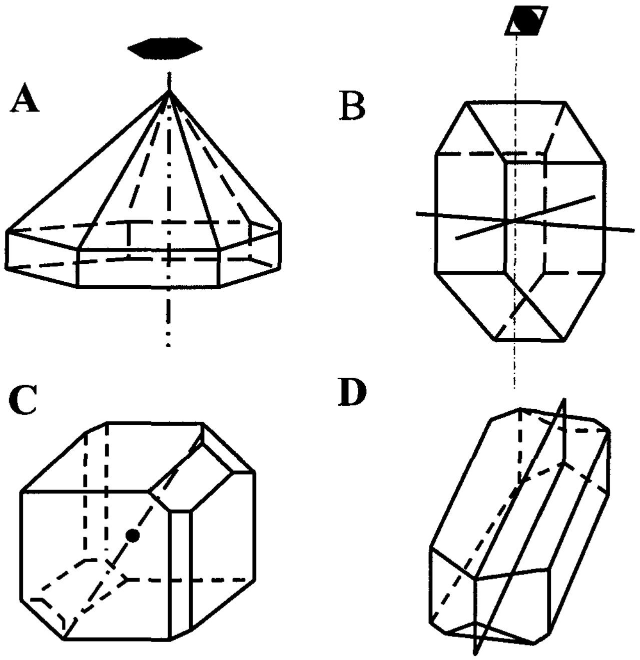

Figure 2-10 - Translation free symmetry elements as expressed by the morphology of crystals. (A) 6-fold axis of rotation (B) 4-fold axis of rotoinversion (C) center of symmetry (D) mirror plane

In the classification of crystals, there are elements of symmetry which govern the crystal classes. They are rotation axes, rotoinversion axes, centres of symmetry and mirror planes, as indicated in Figure 2-10. An axis of rotation is an imaginary line through a crystal about which the crystal may be rotated and repeat itself in appearance 1, 2, 3, 4, or 6 times during a complete rotation. An axis of rotoinversion combines rotation about an axis with inversion through the centre. A center of symmetry is present in a crystal if an imaginary line can be passed from any point on its surface through its center and an identical point is found on the line at an equal distance beyond the center. The center of symmetry is represented in Figure 2-10(C) by a filled circle. A mirror plane is an imaginary plane that divides a crystal into halves, each of which, in a perfectly developed crystal, is the mirror image of the other. This symmetry element, designated in Figure 2-10(D), is sometimes referred to as the symmetry plane.[68]

Table 2-1 - The seven crystallographic crystal systems and their respective unit cell information

Crystal System	Unit Cell Symmetry	
Triclinic	$a \neq b \neq c$ $\alpha \neq \beta \neq \gamma$	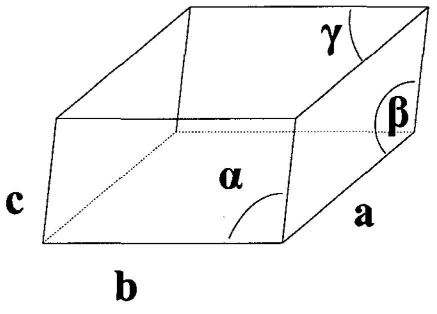
Monoclinic	$a \neq b \neq c$ $\alpha = \gamma = 90° \neq \beta$	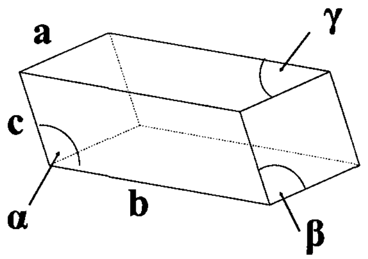
Orthorhombic	$a = b \neq c$ $\alpha = \beta = \gamma = 90°$	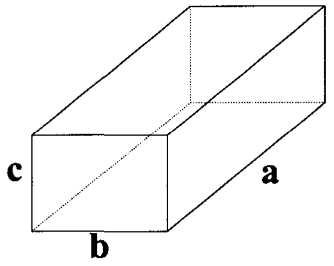
Tetragonal	$a \neq b \neq c$ $\alpha = \beta = \gamma = 90°$	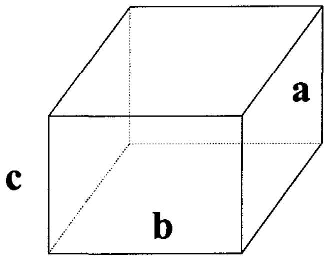

Hexagonal	$a = b \neq c$ $\alpha = \beta = 90^\circ$ $\gamma = 120^\circ$	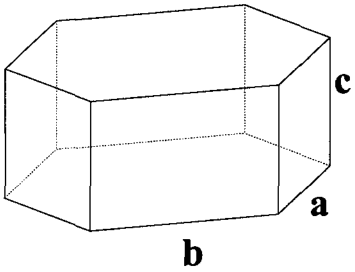
Cubic	$a = b = c$ $\alpha = \beta = \gamma = 90^\circ$	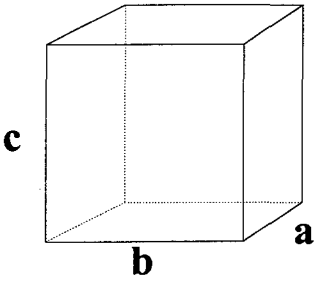
Trigonal	$a = b = c$ $\alpha = \beta = \gamma \neq 90^\circ$	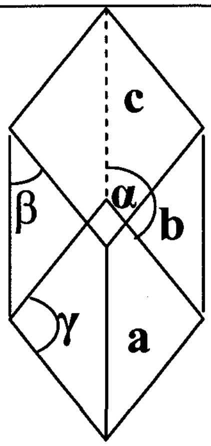

Combinations of different symmetry elements determine 32 point groups or crystal classes. These point groups, uniquely defined by their symmetry, have been given names derived from the general form in each crystal class. The point groups are divided among seven crystal systems. This secondary level of classification groups together the most similar classes, but still allows for each system to have its own specific properties, as seen in Table 2-1.

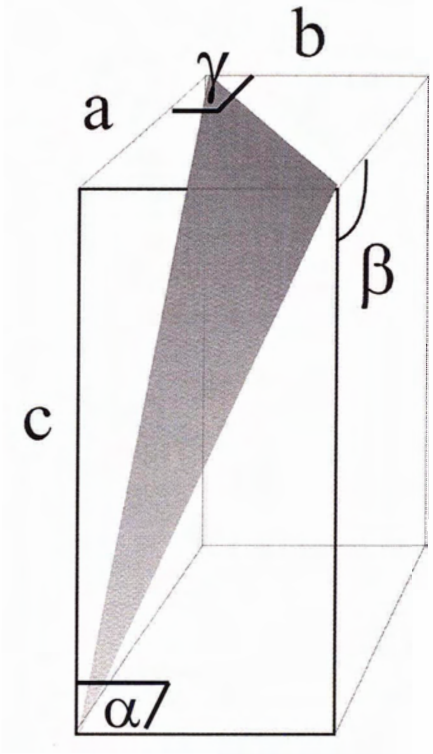

Figure 2-11 - Monoclinic unit cell with the (111) plane highlighted

To distinguish the individual units that a crystal is grown from, it is necessary to distinguish the pattern these units form. One can consider an atom, ion or molecule as the asymmetric unit of crystal structure. The space lattice is "the pattern formed by points representing the locations of the asymmetric units"[69]. The space lattice can be thought of as a "three-dimensional, infinite array of points, each of which is surrounded in an identical way by its neighbors"[69]. This infinite array of points can be thought of as repeating units of a smaller, more basic pattern. The latter units are referred to as the unit cell and can be considered "the fundamental unit from which the entire crystal may be constructed by purely translational displacements"[69]. A primitive unit cell is formed by joining neighboring lattice points by straight lines. As seen in Figure 2-11, the length of the sides of a unit cell are denoted *a*, *b*, and *c* and the angles between them are denoted α, β, and γ. In determining the unit cell for a crystal, the crystallographic axes are as well laid out. The crystallographic axes are imaginary reference lines that are generally taken in parallel to the intersection of major crystal faces and are labeled identically to the sides of the unit cell.[68]

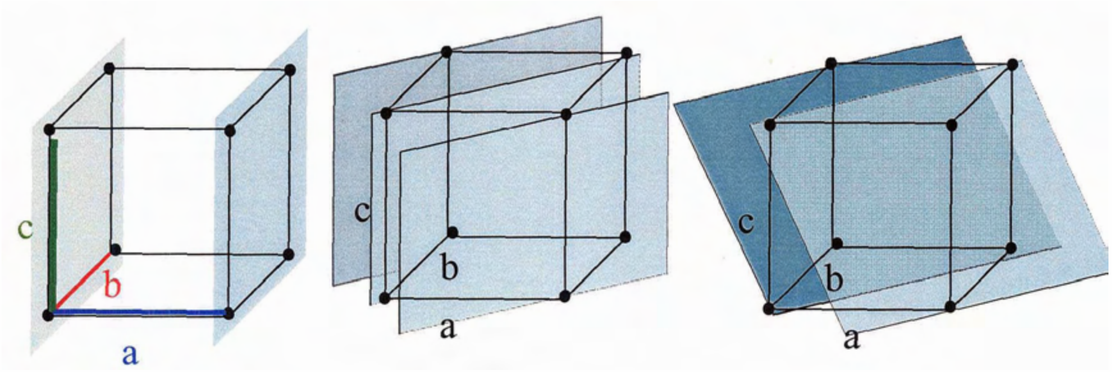

Intersections of the *a* *b* *c* axes in multiples of the length of the unit cell:

1 1 ∞ 1 1 1 1 ∞ ∞

Take the reciprocals of the intersection distances to produce Miller indices:

(1 1 0) (1 1 1) (1 0 0)

Figure 2-12 - Example calculation and spacing of Miller indices. Relationship between the unit cell planes of intersection and Miller indice label is highlighted.

The orientation of faces contained within crystals is most commonly classified by Miller indices. Miller indices are used for expressing the separation of planes because they consist of a series of whole numbers that have been derived from their inversions and, when necessary, the subsequent clearing of fractions. The general symbol for a Miller index is *(hkl)*, in which the letters *h*, *k* and *l* each refer to *a*, *b* and *c* axes respectively. The Miller indices can be calculated for a plane from its axial intercepts as follows: axial intercept values are inverted; fractions are cleared; ∞ becomes 0 upon inversion.[70] It is useful to remember that the *(hkl)* planes divide *a* into *h* equal parts, *b* into *k* parts and *c* into *l* parts. Moreover, the smaller the value of *h* in *(hkl)*, the more nearly parallel the plane is to the *c* axis.[71] An example calculation is presented in Figure 2-12. The parentheses enclose the resulting Miller index. For faces that intersect negative ends of crystallographic axes, a line is placed over the appropriate number.

2.3 Crystallization on Monolayers

The morphological properties of inorganic crystals formed in biological systems are regulated by organized surfaces of biopolymers (biomineralization)[72]. SAMs can be utilized as an organic interface to template the nucleation and growth of inorganic crystals, mimicking the biomineralization process[72]. Therefore, these systems can be utilized as models for gaining a better understanding of this important biological phenomenon.

The overall reasoning for crystal growth of SAMs stems from the generally accepted rule that heterogeneous nucleation on surfaces is energetically more favorable then homogenous nucleation[73,74]. Homogenous nucleation is very rare and requires high supersaturation to surmount the activation barrier. For a fixed supersaturation, the activation barrier can be lowered by decreasing the surface energy of the aggregate by, for instance, introducing a foreign substance or surface[73]. This foreign substance can include SAMs immersed into the supersaturated solution. By introducing the SAM into the crystallizing medium, heterogeneous nucleation is induced. This form of crystallization can provide interfacial interactions with prenucleation aggregates that lower their surface energy, resulting in a smaller critical size of the corresponding nuclei and a more rapid nucleation rate[75].

The drive for the growth of crystals in a very specific direction by SAMs can be explained considering the epitaxial match between the crystal and the organic material or monolayer used as template[76]. For instance, rationalization for the preferential plane of nucleation can be obtained by considering the analysis of the possible interactions between the unit cell of the crystal and the organized surface structure. The process of providing a two dimensional interface to an aqueous crystallizing medium in order to influence crystal growth in the direction of a particular plane by structural mimicry is considered stereochemical matching. Specifically, stereochemical matching is molecular recognition between the molecular arrays of the SAM's functional groups extending into the sub-phase and molecular motifs in incipient nuclei of the crystallizing phase. Alternatively this can be viewed as nucleation driven by structural mimicry by the monolayer of a specific crystal phase[77]. This type of information can be extremely valuable in explaining features in a much more complex biological environment.

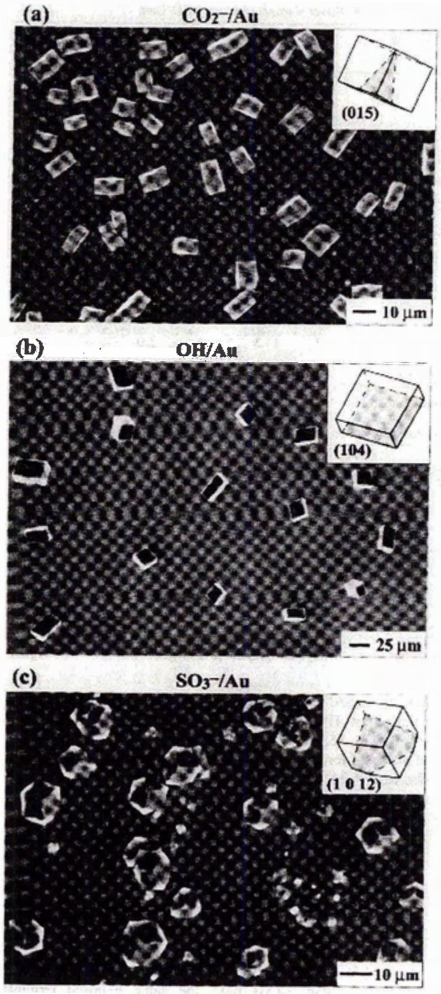

Figure 2-13 - Scanning electron micrographs showing the face-selective nucleation of calcite crystals mediated by SAMs adsorbed on silver: (a) HS-$(CH_2)_{15}$-CO_2^- (b) HS-$(CH_2)_{11}$-OH (c) HS-$(CH_2)_{11}$-SO_3^- reprinted with permission from[78] ©2004 American Chemical Society.

A flexible hydrogen bond network may play a key role in the nucleation of crystals. Hydrogen bonding can occur between two suitable molecules as long as the angle of interaction exceeds 90°[79] and the distance between the oxygen/nitrogen and hydrogen atoms active in hydrogen bonding is no greater than 3.5 Å[80]. Previous work has demonstrated that monolayers of ω–terminated alkanethiols immobilized on solid substrates influence nucleation, orientation, and polymorph selection of crystals by chemical recognition, in some cases hydrogen bonding, between the monolayer terminal functional groups (-X, as in Figure 2-13) and complementary functionalities of incipient nuclei[72,75,77]. In these systems, favorable interactions between the modified surface and individual species of the crystallizing phase facilitate the formation of incipient nuclei by reducing the steric repulsion and by lowering the surface free energy[77,81]. Other examples of directed polymorphism through use of SAMs include the changes in D_2O crystals from amorphous to polycrystalline by varying the temperature and SAM composition[53] and polymorph selectivity of salts through ledge-directed epitaxy on succinic acid[74]. The relationship between the templating substrate and the organic phase lies in the epitaxial matching of lattice spacings of specific crystal planes with some ordered arrangement of molecular units in the template.

Other model studies on orientated crystallization of inorganic and organic materials through the use Langmuir monolayers,[77,82] biological macromolecules,[83,84] and functionalized polymer surfaces[85-87] have failed to produce high yields of face-selective nucleation. On the other hand, face-selective nucleation effects on SAMs have been documented for the crystallization of calcium carbonate[78]. The use of functionalized alkanethiols provided a high level of control over orientation in the crystallization of calcite that had been lacking using other methods[78]. Different calcite orientations were also produced by a variety of different terminal groups on alkanethiols, as shown in Figure 2-13. The ability to attain previously unavailable crystal faces of calcite shows the remarkable promise of thiol SAMs as a crystallization tool[78].

Different ω-terminated alkanethiols hold the potential to interact differently with various types of crystalline salts. The objective of this project was to use SAMs as a template for the crystallization of ammonium tartrate salts. The van der Waals forces readily available to an organic salt as it nucleates and grows can have fundamental effects on its shape, size and orientation. Control of crystal characteristics such as the morphology, size and polymorphism are important to many commercial crystallization processes as they can influence solid flow, solubility, filterability, mechanical properties, aggregation behavior, dispersability, colour and bioavailability[88]. The potential impact of changing crystal forms during late-stage of drug development, in terms of cost and product delay, justifies systematic and early characterization of polymorphism[89]. Aside from its impact on drug quality, it is important to characterize polymorphism because certain forms of crystals may proceed to the costly step of being patented, even when they are not the most stable or optimal form.

Another aspect that we explored is the possibility of enantioselective crystallization. Chiral molecules also play an important role in biological systems. Chiral organic molecules were used in self-assembly processes to form asymmetric surfaces[90]. These chiral surfaces presented distinct catalytic effects for different enantiomers[91]. The preferential interactions between chiral molecules and enantiomeric surfaces may also help explain the origin of the chiral bias in biological systems[92].

Recently, advances have been made in the effort to achieve enantioselective crystallization on a SAM. Banno et al. reported the crystallization of leucine onto SAMs of leucine[93]. While the group did not report enantioselective crystallization from a racemic solution, they detailed X-ray diffraction results for homomeric crystallization. Results of leucine crystallization on leucine/MUA SAMs were presented by Eun and Umesawa[94]. The selective crystallization of L-leucine over DL-leucine was detected with the use of a quartz crystal microbalance (QCM). Other similar attempts towards enantioselective separation using QCMs for detection were also reported elsewhere[95,96].

3 Experimental

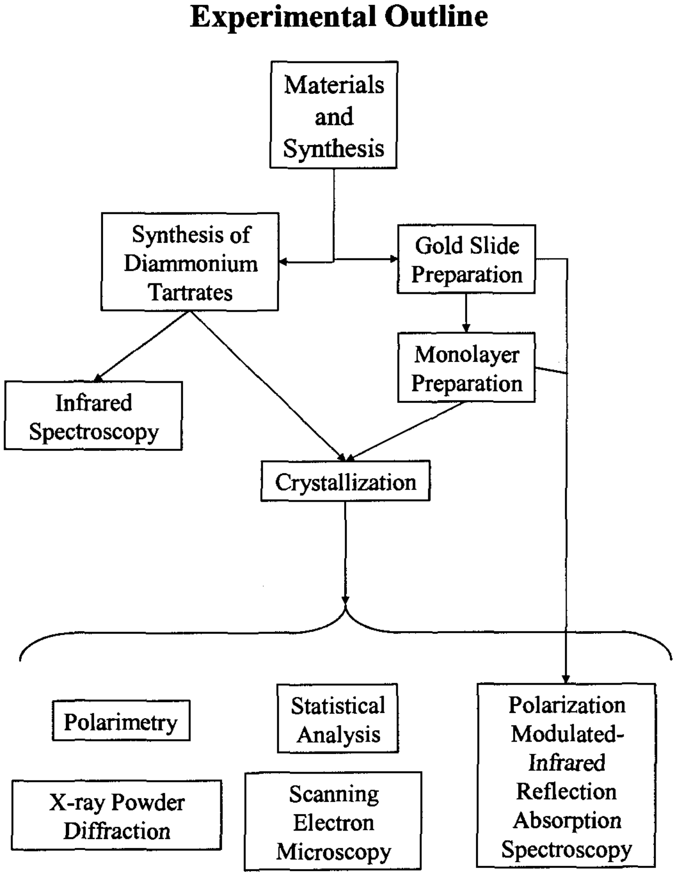

Figure 3-1 - Flowchart of the experimental process.

The overall process of experimental data collection for this thesis consisted of (a) experimental trials and (b) characterization and imaging. A flow chart of the experimental procedure is shown in Figure 3-1. The experimental trials themselves contained the necessary steps to produce monolayers and synthesize the diammonium tartrates which eventually led to the crystallization procedure. Once the Au slides with crystallized materials had been obtained, five different characterization and imaging techniques were completed. Further detail as to the experimental procedures and characterization techniques will be introduced in the upcoming sections. Any data collected pertinent to experimental process will as well be presented in this section, with the exception of the monolayer characterization, which will be presented in Chapter 4.

3.1 Materials and Equipment

3.1.1 Chemicals and Substrates

D-tartaric acid, L-tartaric acid, D,L-tartaric acid, L-Diammonium tartrate, L-cysteine, and D,L-cysteine were purchased from Sigma-Aldrich. Ammonium hydroxide was purchased from Anachemia. Solvents (ethanol) were purchased from Commercial Alcohols Inc. Ultra pure water (18 MΩ cm^{-1}) was obtained from a Diamond Nanopure water purification system from Barnstead Brand Water Systems©. Au coated glass slides were purchased from Evaporated Metal Films. The 2.54mm x 2.54mm x 1 mm slides were coated with 5nm of chromium and 100nm of gold.

3.1.2 Synthesis of D, L and DL-Diammonium Tartrates

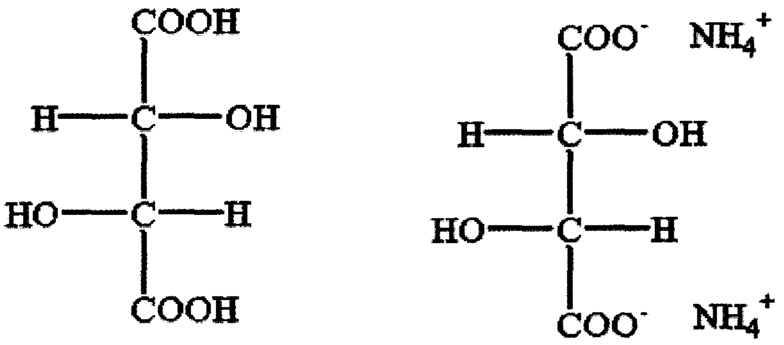

Figure 3-2 - Molecules of tartaric acid (left) and diammonium tartrate (right)

Diammonium tartrates were synthesized by first preparing a ~.05 M solution of tartaric acid in absolute ethanol. Solutions were sonicated to aid in tartaric acid dissolution. Ammonium hydroxide (17%) was added to the solutions, allowing for a 2:1 molar ratio of ammonium to tartaric acid. A cloudy white precipitate was formed upon addition of ammonium hydroxide, according to equation (3.1).

$$(3.1)\ \mathrm{HOOCCH(OH)CH(OH)COOH} + 2\mathrm{NH_4OH} \rightarrow \mathrm{(OOCCH(OH)CH(OH)COO)(NH_4)_{2(s)}} + 2\mathrm{H_2O}$$

Solutions were thoroughly mixed to allow for complete reaction of ammonium hydroxide with tartaric acid. The solutions were then filtered and a sample of the solid taken for Fourier Transform Infrared (FTIR) analysis using the total internal reflection accessory (Pike) on a Bruker Equinox 55 equipment. The diammonium tartrate was then recrystallized using absolute ethanol as a salting out agent. Example spectra of the synthesized diammonium tartrates are shown in Figure 3-3 and Figure 3-4. The agreement of the characteristic vibrational frequencies to literature values[97] is presented in Table 3-1.

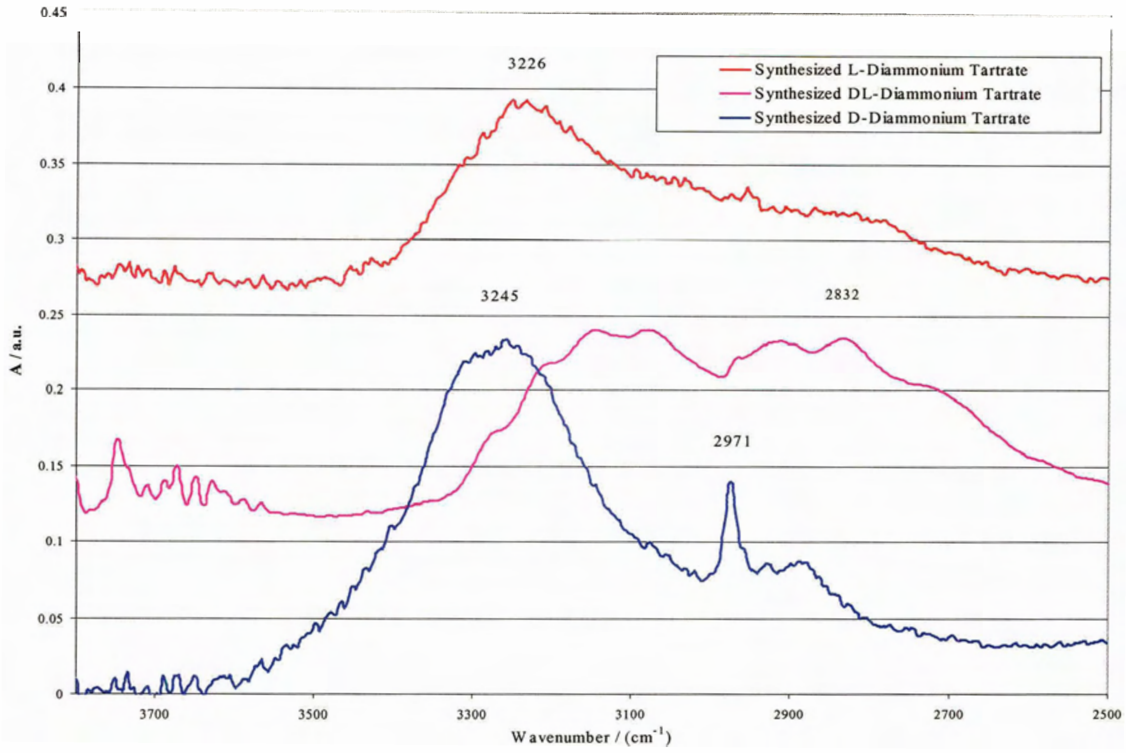

Figure 3-3 - FTIR Spectra (from 2500 cm^{-1} to 3800 cm^{-1}) of synthesized diammonium tartrates.

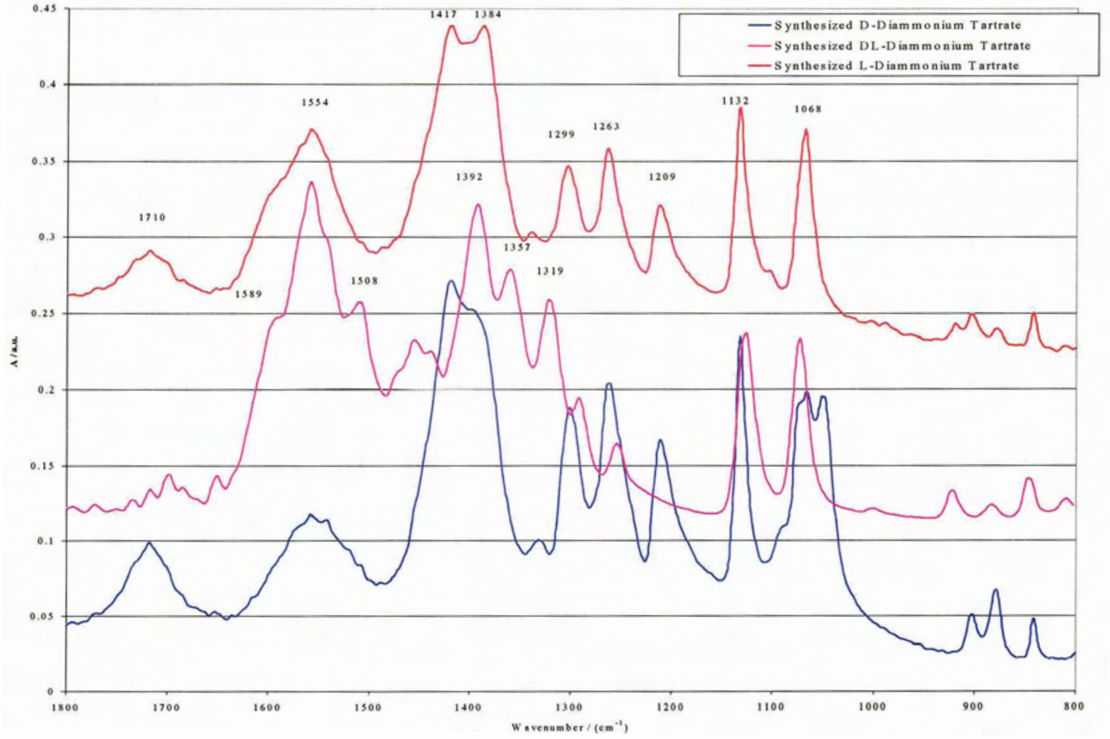

Figure 3-4 - FTIR Spectra (from 800 cm^{-1} to 1800 cm^{-1}) of synthesized diammonium tartrates.

Table 3-1- FTIR Analysis of Synthesized DL-Diammonium Tartrate

Peak Frequencies (cm^{-1})				
FTIR Values for Synthesized L-Diammonium Tartrate	FTIR Values for Synthesized D-Diammonium Tartrate	FTIR Values for Synthesized DL-Diammonium Tartrate	Literature Values[97] for DL-Diammonium Tartrate	Band Assignment
3226	3245		3382	$\mathrm{NH}_{\mathrm{str}}$
		2832	2835	$\mathrm{NH}_{\mathrm{str}}$
1710	1716	1697	1716, 1703	$\mathrm{CO}_{2\ \mathrm{str}}$
1579	1583	1589	1578	$\mathrm{NH}_{\mathrm{bend}}$
1558	1557	1558	1560	$\mathrm{CO}_{2\ \mathrm{str\ ass}}$
		1508	1487	$\mathrm{NH}_{\mathrm{bend}}$
1417,1384	1417	1392	1392	$\mathrm{CO}_{2\ \mathrm{str\ sym}}$
1299	1295	1319	1313	$\mathrm{CH}_{\mathrm{bend}}$
1263	1261	1253	1269	$\mathrm{CO}_{\mathrm{str}}$
1132	1131	1127	1120	$\mathrm{CO}_{\mathrm{str}}$
1068	1066	1073	1078	$\mathrm{CO}_{\mathrm{str}}$

3.2 Monolayer Formation

3.2.1 Preparation of Gold Slides

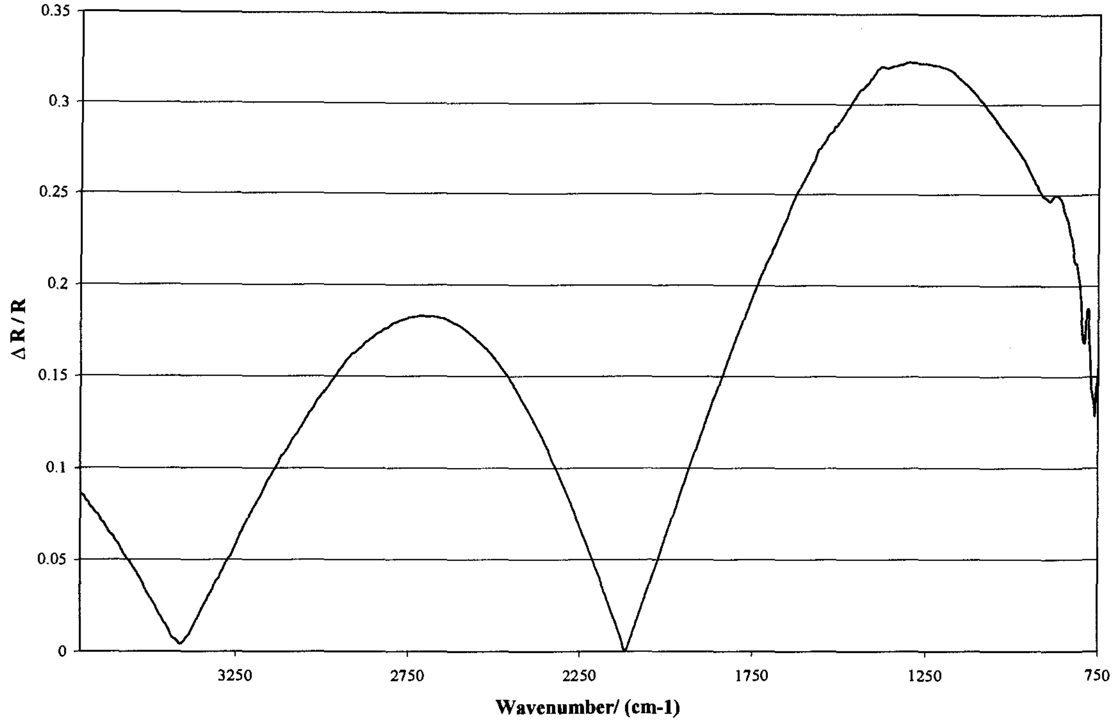

Figure 3-5 - PM-IRRAS Spectra of Au (111) Slide after Cleaning

Au coated glass slides were initially flamed using a hydrogen torch to clean and anneal the surface[98]. To further cleanse the slides, they were placed in a Harrick plasma oven on high for ~ 10 minutes. Cleaning by the plasma oven is effected by the formation of reactive plasma that chemically interacts with carbonaceous materials on the gold surface. Although 1-2 minutes of plasma bombardment is usually sufficient to cleanse metallic slides of carbon material, a longer time was chosen to ensure a completely uncontaminated surface[99]. PM-IRRAS spectra were then acquired. A typical PM-IRRAS spectrum of a clean gold slide surface is shown in Figure 3-5. The effectiveness of the cleaning procedure is shown in Figure 3-5. The broad features of the PM-IRRAS are due to the modulation procedure[100] and will be discussed in Chapter 3.4.1. The spectrum of the clean slide was used as a background and subtracted from the PM-IRRAS spectra obtained for slides modified with monolayers.

3.2.2 Monolayer Preparation

The procedure for monolayer formation followed the usual method used in the literature [36,38,61,78,101-110]. Solutions of MUA in ethanol (~.05M) and cysteine in water (~.1M) were prepared. Cleaned gold slides were placed into Petri dishes with the glass side facing down and then covered with the prepared monolayer solutions. The systems were allowed to sit for ~24 h to ensure complete monolayer adsorption and to allow sufficient monolayer ordering. The slides with the monolayers were then withdrawn from the solution and rinsed with appropriate solvent. PM-IRRAS spectra were collected to confirm the monolayer formation.

3.3 Crystallization Trials

3.3.1 Crystallization

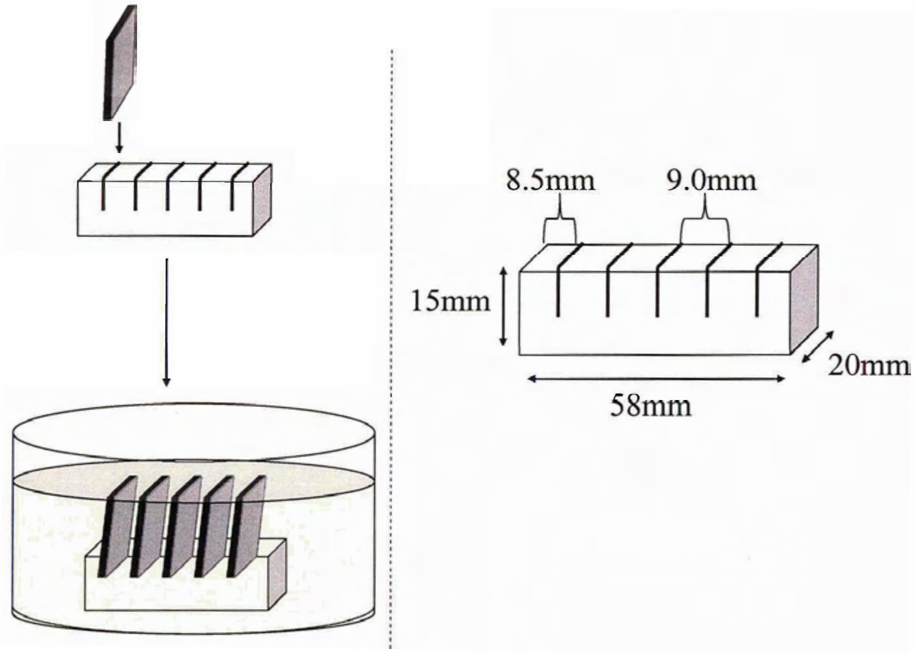

Figure 3-6 - Schematic of Crystallization Setup

Monolayer covered slides were placed with the monolayer perpendicular to the surface using a fabricated Teflon slide holder, as seen in the right of Figure 3-6. The gold slides fit snugly into the holder.

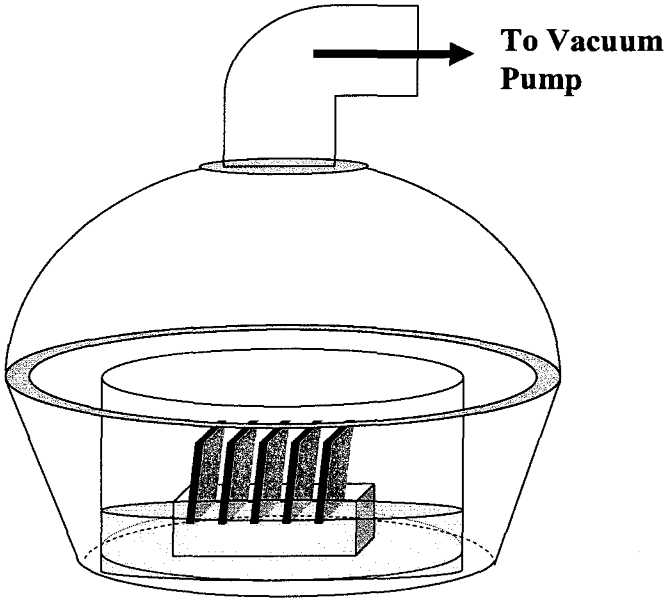

Figure 3-7 - Crystallization apparatus

Once solutions of diammonium tartrate were prepared (~.1 M), sets of five slides were lowered into the prepared crystallizing solutions. The samples were then placed into desiccators and placed under vacuum in order to extract the water vapor, as seen in Figure 3-7. A Leeson (Model# NE4C17DH7A) rotatory pump was used. The pressure inside the desiccators can be estimated as around 30 mTorr.

The systems were kept under vacuum until all of the water from the diammonium tartrate solution was evaporated, which took approximately 5 days. As the solvent from the crystallizing solution evaporates, the solution becomes more concentrated, slightly shifting the crystallization equilibrium so that crystal nucleation is more likely to reach "critical size". If the nuclei interact favorably with monolayer, then nucleation on the surface will be facilitated.

The perpendicular positioning of the monolayer slides ensured that crystals on the surface would be those that had nucleated with an interaction with the SAM surface and not those that had simply nucleated in solution. Clean gold slides were also placed in the crystallizing tray as blanks to confirm that surface crystallization was being facilitated by monolayer interactions.

Once the crystallizing solution had evaporated, the slides were removed from the system and imaged using an MDPlan 10x microscope objective lens of an Olympus BHT optical microscope. The crystals were also photographed using an Olympus PM-6 camera, adapted to fit the observation tube of the ocular eyepiece of the optical microscope.

3.3.2 Crystallization Statistical Data

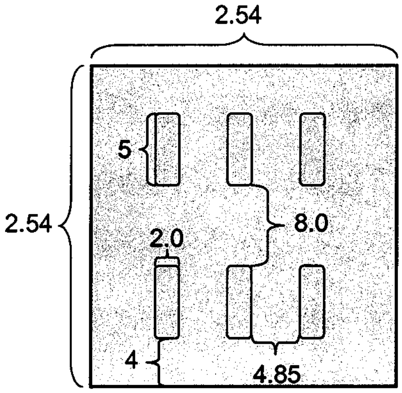

Figure 3-8 - Schematic of the stainless steel mask. All internal dimensions are in millimeters. All external dimensions are in centimeters.

In order to acquire a representative population for statistical analysis, a stainless steel mask was fabricated as shown in Figure 3-8. The statistical mask is 2.54 cm x 2.54

cm x 1 mm, corresponding to the size of the gold slides. Six slots, with each having an area of 10.0 mm^2, were cut out of the mask, making the viewable area of the gold slide 60.0 mm^2.

3.3.2.1 *Crystal Classification*

Crystals were classified according to their shape and size. Only crystals that were fully visible within the six slots of the statistical mask were counted. Classification of crystal shape involved organizing the crystals into seven categories, as indicated by Table 3-2. Shape was determined by viewing crystals through an optical microscope and photographing the crystals by means of a camera adapted to fit the ocular eyepiece of the microscope. The visible faces of the crystals, most commonly found perpendicular to surface normal, were used for shape classification. Classification of crystals was done in two dimensions. Crystals that did not appear to fit into a preset category were labeled as indistinguishable. For size measurements, crystals were measured by hand from photographs. All crystal measurements indicate the length of the crystals from the edges that were situated furthest apart from each other.

Table 3-2 - Crystal Classification Descriptions

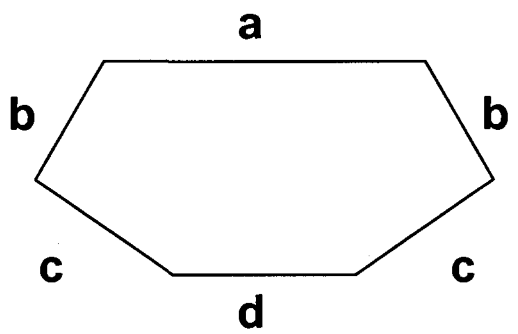	Class A Six sides $a \neq b \neq c \neq d$

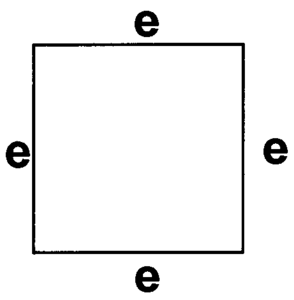	Class B Four sides All sides, e, are = or ≅ in length
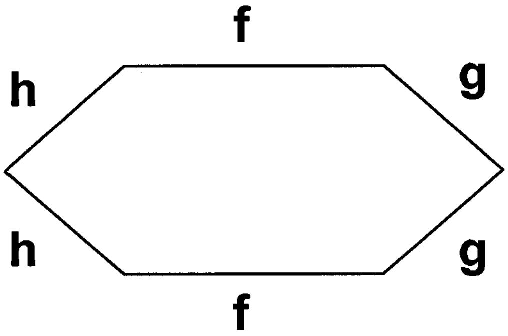	Class C Six sides Four sides, g ≅ h Two sides, f >> g ≅ h
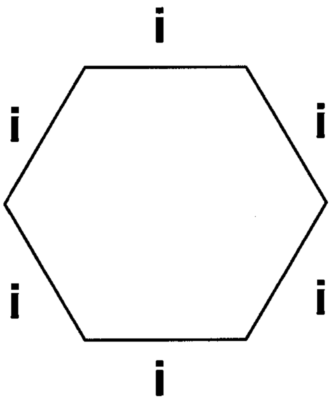	Class D Six sides All sides, i, are = or ≅ in length
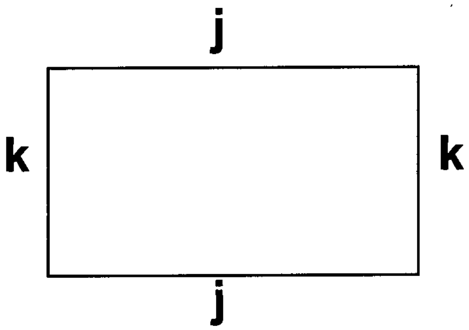	Class E Four sides Sides j are = or ≅ in length Sides k are = or ≅ in length All angles are = or ≅ 90°

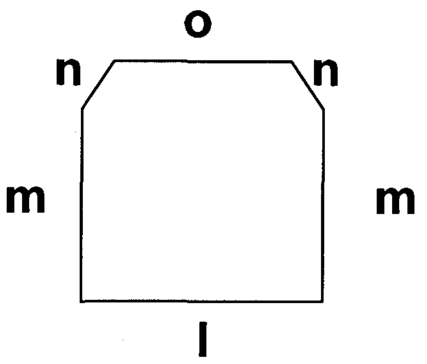 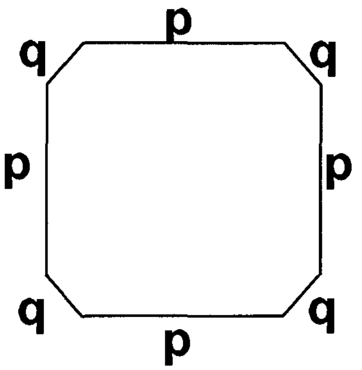	In some cases, two sides appear to form blunted corners Sides m ≅ in length Sides n ≅ in length One side, o, shortened by blunted corners $m \neq n \neq o$ In some cases, four sides appear to form blunted corners Sides p, ≅ in length Sides q, ≅ in length $p \neq q$
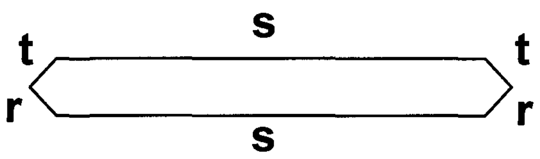	Class F Similar to Class C, except that elongation in sides $r \approx t \ll s$

3.4 Characterization and Imaging

3.4.1 Polarization-Modulated Infrared Reflection-Absorption Spectroscopy

Direct analysis of polarization-modulated infrared reflection-absorption spectroscopic (PM-IRRAS) spectra can yield important information at the vibrational level on the nature and orientation of the surface molecules [111,112]. Therefore, this technique was used to characterize the formation of the monolayer and assess its quality. The PM-IRRAS data was collected on a Bruker PMA 37 Equinox 55 FTIR and manipulated with OPUS (V4.0) software. Figure 3-9 shows a schematic of the experimental setup for PM-IRRAS.

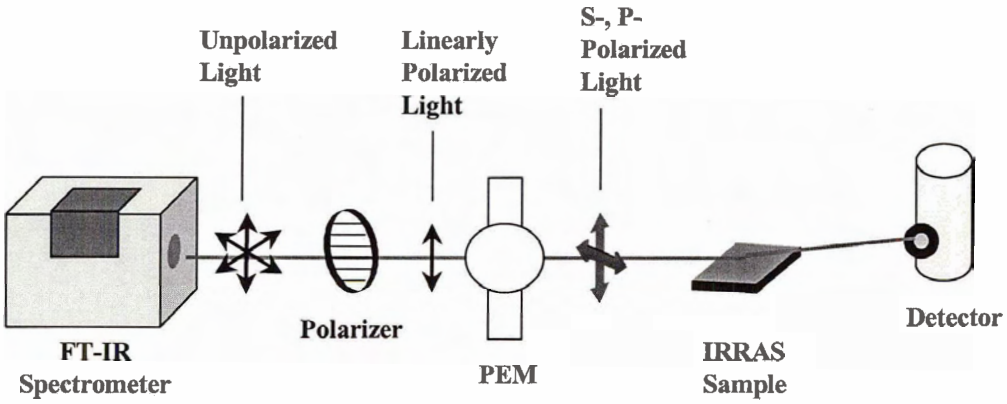

Figure 3-9 - Schematic Set-up of PMIRRAS

The PM-IRRAS technique and its applications are being widely used to investigate processes involving adsorbed molecules. A detailed review of the method and its application can be found elsewhere [113]. Here we will briefly describe the experimental setup used in this dissertation. As shown in Figure 3-9, the unpolarized infrared (IR) light is first passed through a linear polarizer. Next the linearly polarized light travels through the photoelastic modulator (PEM)[113,114]. The PEM (from Hinds ZnSe) consists of a piezoelectric transducer and houses a quartz plate. The ZnSe plate oscillates along its dimension at a frequency of 50 kHz. The transducer is tuned at the same frequency and driven by electronics controlling the amplitude of the vibration. The ZnSe plate exhibits birefringence, which will cause a continuous wave retardation as shown in Figure 3-10.

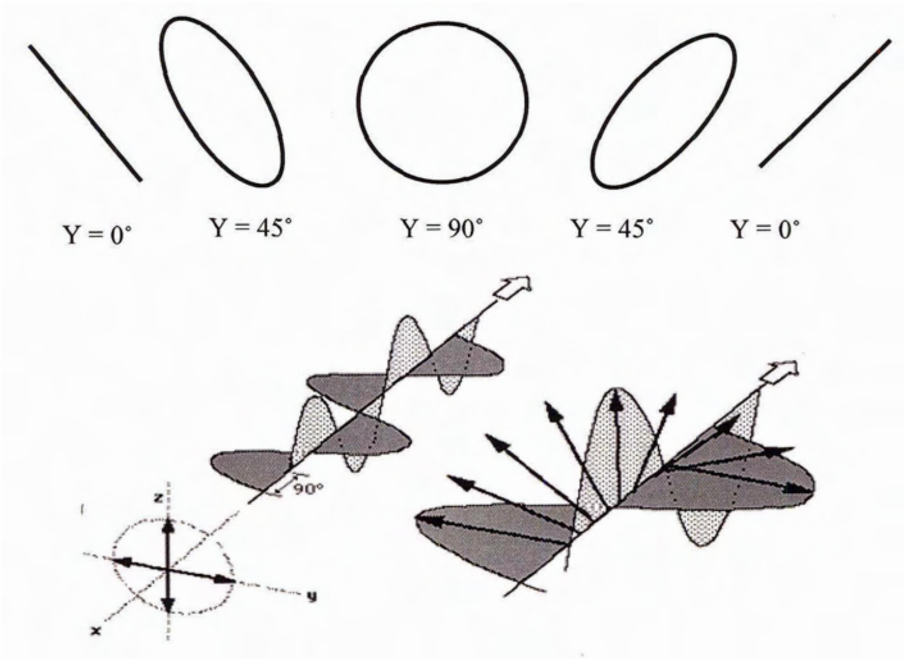

Figure 3-10 - Illustration of the continuous wave retardation effect of the PEM. The transition from linearly polarized light to circularly polarized light is indicated at the bottom. Shape of the retarded light at various degrees in the y direction is indicated along the top

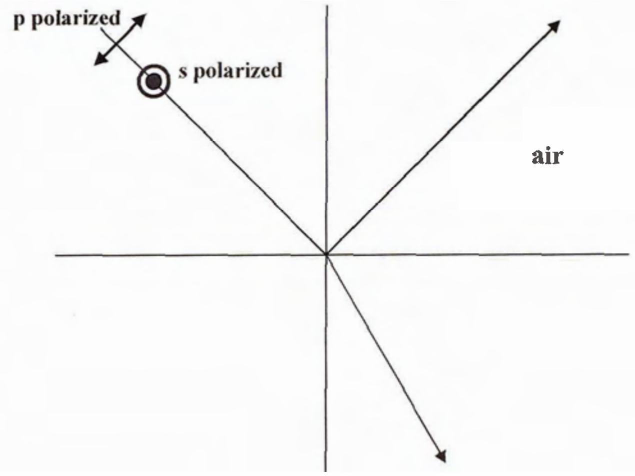

Figure 3-11 - Rays of s polarized and p polarized light as they interact with the surface. The p polarized light which is parallel to the propagation direction is reflected and the s polarized light, which is perpendicular to the propagation direction is refracted.

The plane polarized components of the light field that propagates parallel and perpendicular to the plane of incidence are defined as the p-polarized and s-polarized components of the light, respectively; as illustrated in Figure 3-11[113,115].

The s and p components of the polarized light are reflected from the surface of the metallic sample (Au (111)) placed in the sample holder. Finally, a detector (Liquid nitrogen cooled MCT with BaF_2 window model D313/Q from Bruker) collects the light and a signal is transmitted to the proper electronics for demodulation [116] and recorded by a computer.

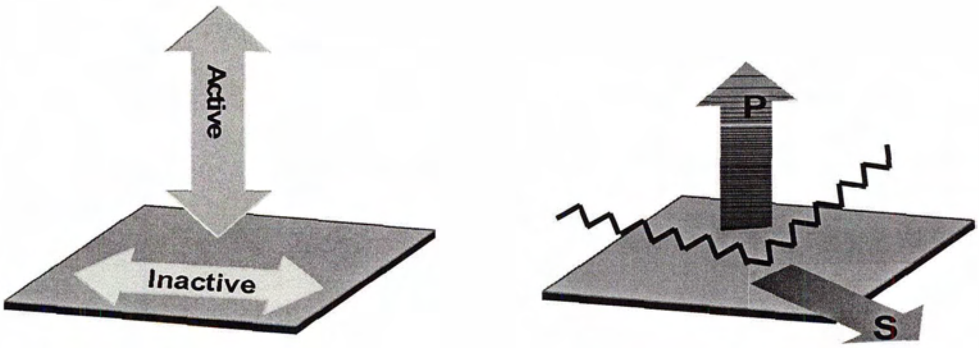

Figure 3-12 - Interaction of s and p polarized light with metallic surface

The principal reason to employ PM-IRRAS in monolayer analysis is that the vibrations of the adsorbed molecules have components normal and parallel to the surface. Due to surface selection rules[100,113,117], only components normal to a metal surface are IR active, as depicted in Figure 3-12, because the dipoles of the s component oscillate in the plane of the substrate and are screened by the delocalized electrons in the metal. This fact tells us that that the only active infrared modes will be those where the change in dipole moment due to the vibrational motion has a component normal to the substrate. Therefore, at an incident grazing angle, the s component of the IR light will become negligible and the p component will enhance in intensity. This surface selection rule allows for the vibrational detection of adsorbates on the surface without the interferences.

3.4.2 Powder X-Ray Diffraction

Powder x-ray diffraction (XPD) spectra were produced using a Siemens D5000 powder X-ray diffractometer. The samples were sent to Dr. Mati Raudsepp from The Department of Earth and Ocean Sciences at the University of British Columbia. X-ray diffraction was used to identify the various planes of the powdered crystalline samples produced in our experiments.

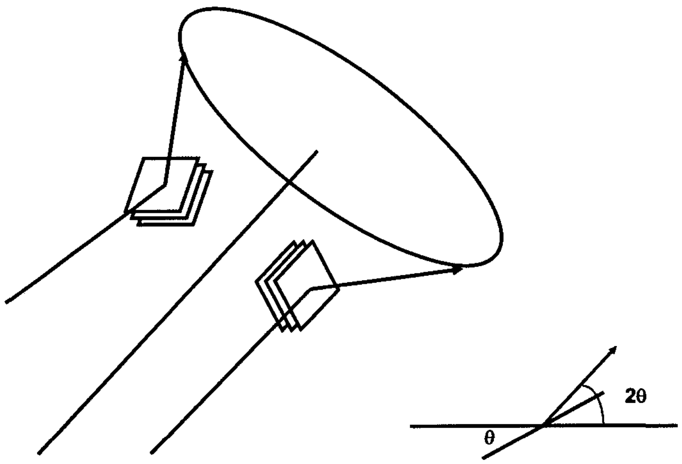

Figure 3-13 - Upper left, depiction of the diffracted incident beams forming conical rings from various *hkl* planes in a XPD sample. Bottom right, indication of the grazing angle used to determine sample planes.

The basis of X-ray diffraction techniques relies on the concepts of reflection and interference. When an incoming beam of X-rays enters a crystal, they are reflected by the planes contained inside. If the path length difference of the incoming and reflected x-rays is not equal to an integer number of wavelengths, then the waves interfere largely in a destructive manner. If the path length difference does equal an integer number of wavelengths, then Bragg's law, shown in equation 3.2, is satisfied, the waves will interfere with each other constructively and a bright reflection will occur. "The primary use of Bragg's law is in the determination of the spacing between the layers in the crystal lattice, once the grazing angle (θ) corresponding to a reflection has been determined, *d* may be readily calculated"[69].

$$(3.2) \quad n\lambda = 2d \sin \theta$$

In a XPD experiment, sharp peaks arise in the spectra once the conditions for constructive interference are satisfied. The powdered sample is spread on a flat plate and the diffraction pattern is monitored electronically as the detector is rotated around the sample in a plane containing the incident monochromatic ray, as shown in Figure 3-13. The crystallites in the sample will be oriented so that different planes in the sample will give rise to diffracted intensity at different grazing angles. The crystallites with this grazing angle will lay at all possible angles around the incoming beam, so the diffracted beams will lie on a cone around the incident beam of half angle 2θ. Each set of planes in the powdered sample will give rise to a cone of diffracted intensity with a different half-angle.

L and D-diammonium tartrate reference spectra were available through The International Centre for Diffraction Data (ICDD). Diammonium tartrate spectra unavailable in the ICDD were simulated using teXsan for windows© (V1.06).

3.4.3 Scanning Electron Microscopy

Scanning electron microscopy (SEM) is a form of microscopy which uses electrons rather than light to produce an image. The resolution capability of SEM is superior to that optical microscopy. Any signal that arises from SEM is from interaction of the sample with the incident electron beam and will subsequently produce a final image with greater contrast and detail[118]. For this dissertation, scanning electron microscopy images were gathered using a Hitachi SM-3500N variable pressure scanning electron microscope with energy dispersive X-ray microanalyser. This system is available at UVic's Department of Biology.

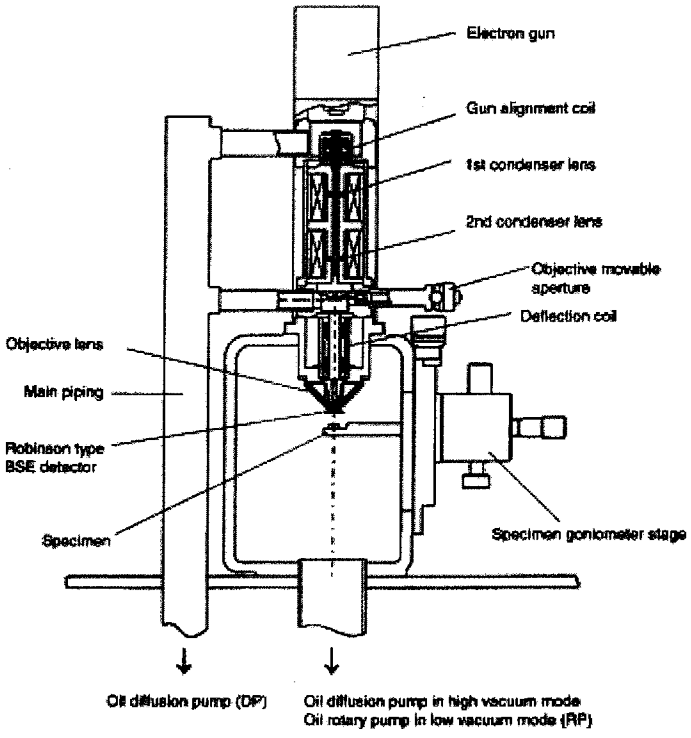

Figure 3-14 - Schematic of a Hitachi SM-3500N Scanning Electron Microscope

As seen in the SEM schematic obtained from the instrument's manual, Figure 3-14, a beam of electrons is generated in the electron gun, located at the top of the column. This beam is directed through the anode and a series of condenser lenses, and finally focused precisely on the sample by the objective lens. The scan coils are energized (by varying the voltage produced by the scan generator) and create a magnetic field which deflects the beam back and forth in a controlled pattern. The varying voltage is also applied to the coils around the neck of the Cathode-ray tube (CRT) which produces a pattern of light deflected back and forth on the surface of the CRT. The pattern of deflection of the electron beam is the same as the pattern of deflection of the spot of light on the CRT. The electron beam hits the sample, producing secondary electrons from the sample. These electrons are collected by a secondary detector or a backscatter detector, converted to a voltage, and amplified. The amplified voltage is applied to the grid of the CRT and causes the intensity of the spot of light to change. The image consists of thousands of spots of varying intensity on the face of a CRT that correspond to the topography of the sample.

3.4.4 Polarimetry

Anisotropic crystalline solids, and liquid samples containing an excess of one enantiomer of a chiral molecule, can rotate the orientation of plane-polarized light[69]. Such substances are said to have optical activity. Measurement of this change in polarization orientation is called polarimetry, and the measuring instrument is called a polarimeter. The set up of an example polarimeter is illustrated in Figure 3-15. These measurements are useful for studying the structure of anisotropic materials, and for checking the purity of chiral mixtures. A sample that contains only one enantiomer of a chiral molecule is said to be optically pure. The enantiomer that rotates light to the right, or clockwise when viewing in the direction of light propagation, is called the dextrorotatory (D) or (+) enantiomer, and the enantiomer that rotates light to the left, or counterclockwise, is called the levorotatory (L) or (-) enantiomer. A nomenclature system which takes into account the absolute configuration (R- S- system) is generally preferred in the chemical literature[119]. For this dissertation, polarimetry measurements were taken using a Rudolph Research Autopol III automatic polarimeter.

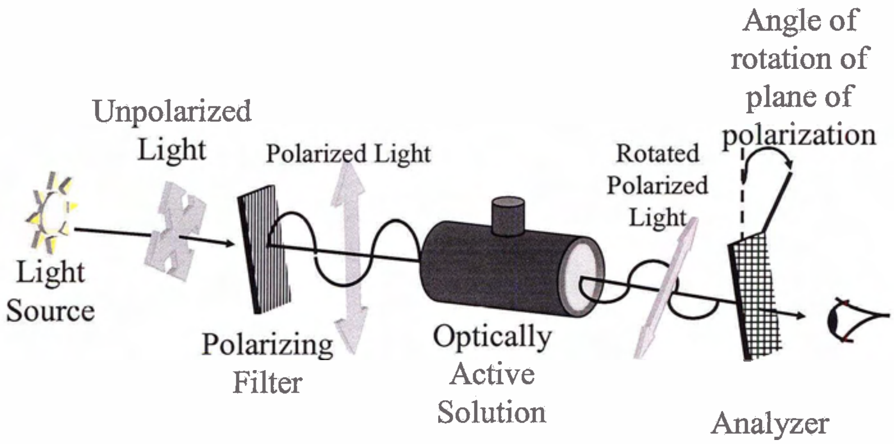

Figure 3-15 - Polarimetry schematic showing the pathway of light

Optical rotation occurs because optically active samples have different refractive indices for left- and right-circularly polarized light[69]. Another way to make this statement is that left- and right-circularly polarized light travel through an optically active sample at different velocities. This condition occurs because a chiral center has a specific geometric arrangement of four different substituents, each of which has a different electronic polarizability. Light travels through matter by interacting with the electron clouds that are present. Left-circularly polarized light therefore interacts with an anisotropic medium differently than does right-circularly polarized light.

Linearly or plane-polarized light is the superposition of equal intensities of left- and right-circularly polarized light[69]. As plane-polarized light travels through an optically active sample, the left- and right-circularly polarized components travel at different velocities. This difference in velocities creates a phase shift between the two circularly polarized components when they exit the sample. Summing the two components still produces linearly polarized light, but at a different orientation from the light entering the sample.

4 Results and Discussion

4.1 Polarization-Modulated Infrared Reflection-Absorption Spectroscopy for Cysteine Monolayers

Figure 4.1 shows the PM-IRRAS spectra for cysteine species adsorbed on Au (111) surfaces.

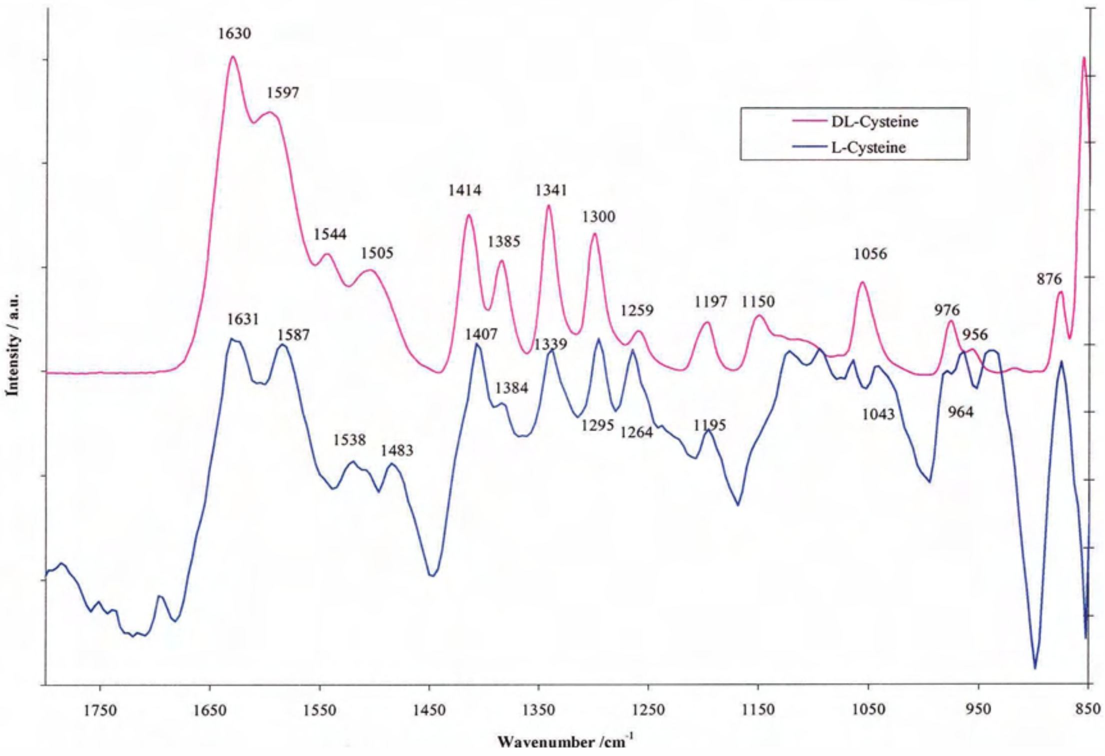

Figure 4-1 - Representative PM-IRRAS spectra of L-cysteine (blue) and DL-cysteine (pink) adsorbed on Au(111) surfaces

The strong peaks in Figure 4-1 confirms the presence of the cysteine adsorbed at the gold surface. The good quality of the IR spectra is an indication that the cysteine molecules are well-organized[120]. The assignment for some of the vibrational bands indicated in Figure 4-1 is presented in Table 4-1. The assignment were based on previous work[57,97,121,122]

Table 4-1 - Vibrational assignments for cysteine adsorbed on Au(111) surfaces

L-cysteine		**DL-cysteine**	
Peak	Assignment	Peak	Assignment
1631	NH_3^+ deg def	1630	NH_3^+ deg def
1587	CO_2^- asym str	1597	CO_2^- asym str
1407	CO_2^- sym str	1414	CO_2^- sym str
1392	CO_2^- asym str	1385	CO_2^- asym str
1339	CH bend	1341	CH bend
1264	CO bend in plane	1259	CO bend in plane
975	CO asym str	976	CO asym str
964	CC str	956	CC str

L-cysteine occurs in the zwitterionic form in the bulk solid phase and neutral solution. The CO_2^- asymmetric and symmetric stretching modes are assigned to the bands at 1587 and 1394 cm^{-1} in the solid state, respectively. As seen in both Figure 4-1 and Table 4-1, the bands at 1587, 1407 and 1392 cm^{-1} for L-cysteine and 1597, 1414 and 1385 cm^{-1} for DL-cysteine have been assigned to the CO_2^- asymmetric and symmetric stretching modes. The presence of these bands shows that the adsorbed cysteine is also in its zwitterionic form. Additional evidence for a zwitterionic monolayer is the in-plane bending and asymmetric stretching assigned to the 1260-970 cm^{-1} region. The lack of a broad OH peak in the 3500-3000 cm^{-1} range also provides evidence for the zwitterionic monolayer form. Thus, it is concluded that the cysteine is absorbed on the surface in the zwitterionic form. The presence of the NH_3^+ groups is in fact supported by the assigned band at 1631 cm^{-1} for L-cysteine and 1630 cm^{-1} for DL-cysteine. The bands at 1195 cm^{-1} for L-cysteine and 1197 cm^{-1} for DL-cysteine, as well support the presence of the NH_3^+ group.

4.2 L-Diammonium Tartrate on L-Cysteine Monolayers

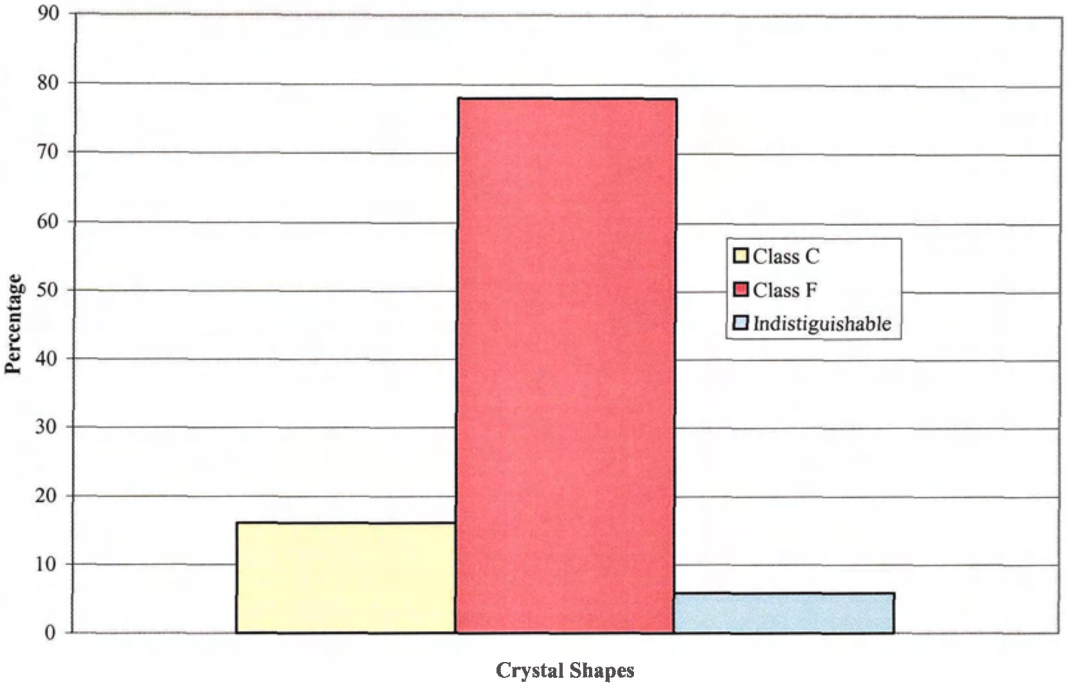

Figure 4-2 - Percentage distribution of shapes for L-diammonium tartrate crystals on L-cysteine monolayers

An overwhelming majority of crystals in this system were placed in Class F, as defined in Table 3.2. As indicated by Figure 4-2, from a statistical population of 1024 crystals, 799 L-diammonium tartrate crystals were classified as Class F. Crystal sample sizes for Class C and Indistinguishable categorizations were 60 and 165, respectively. The average length of the crystals, 83 ± 32 μm, is small in comparison to the other statistical data sets that will be presented in the next sections. The density of the L-diammonium tartrate crystals on the surfaces with L-cysteine monolayers was 1.1×10^{-2} crystals/μm^2. The average size and density figures point to a high amount of nucleation on the monolayer / L-cysteine-modified Au (111) surface. The strong presence of well defined crystals and a weak presence of irregularly shaped crystals indicate a favorable interaction with the monolayer. Polarimetry data for L-diammonium tartrate crystals from L-cysteine monolayers produced an angular rotation of polarized light to +0.201°. A strong rotation of the polarized light is expected because of the homomeric qualities of the system. The actual orientation of the tartrate on the surface and the molecular groups which provide the favorable interaction can be better visualized by analyzing the orientation of the crystals themselves.

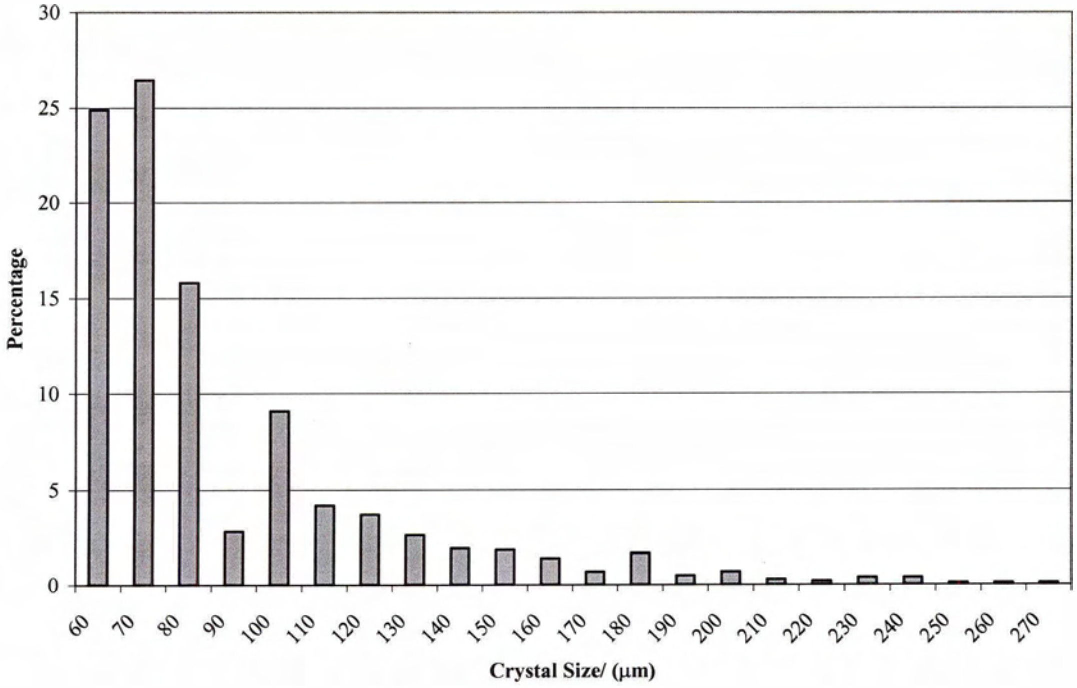

Figure 4-3 - Size percentage distribution of L-diammonium tartrate crystals on L-cysteine monolayers

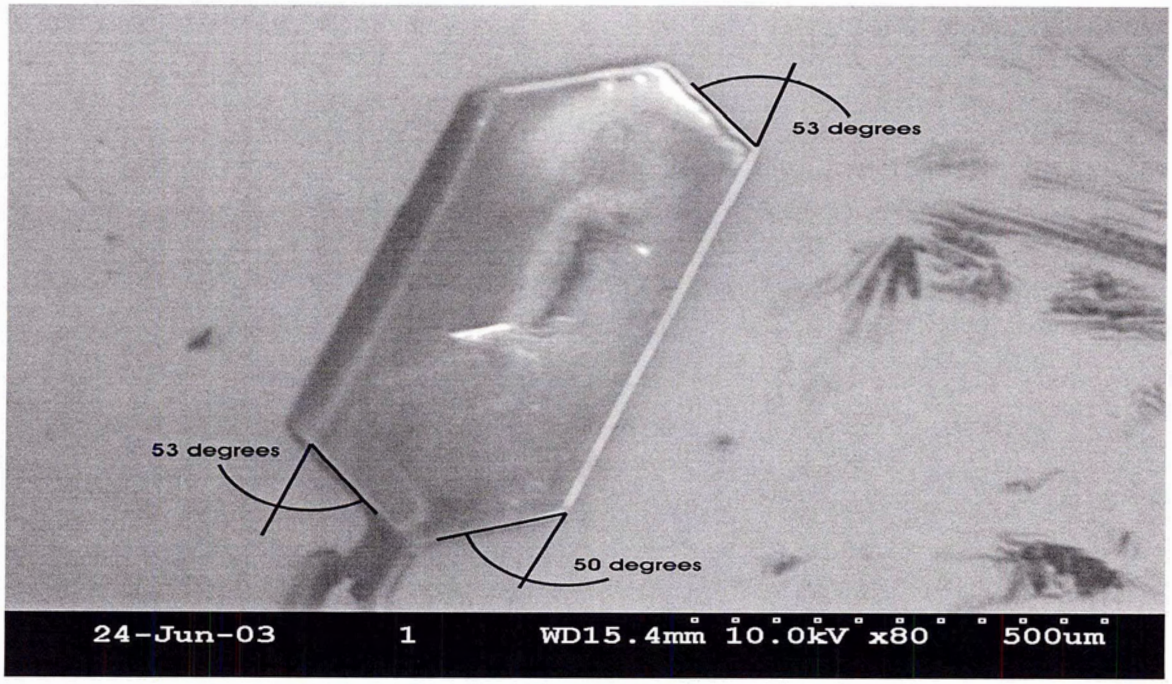

Figure 4-4 - SEM image of a L-diammonium tartrate crystal on an L-cysteine monolayer

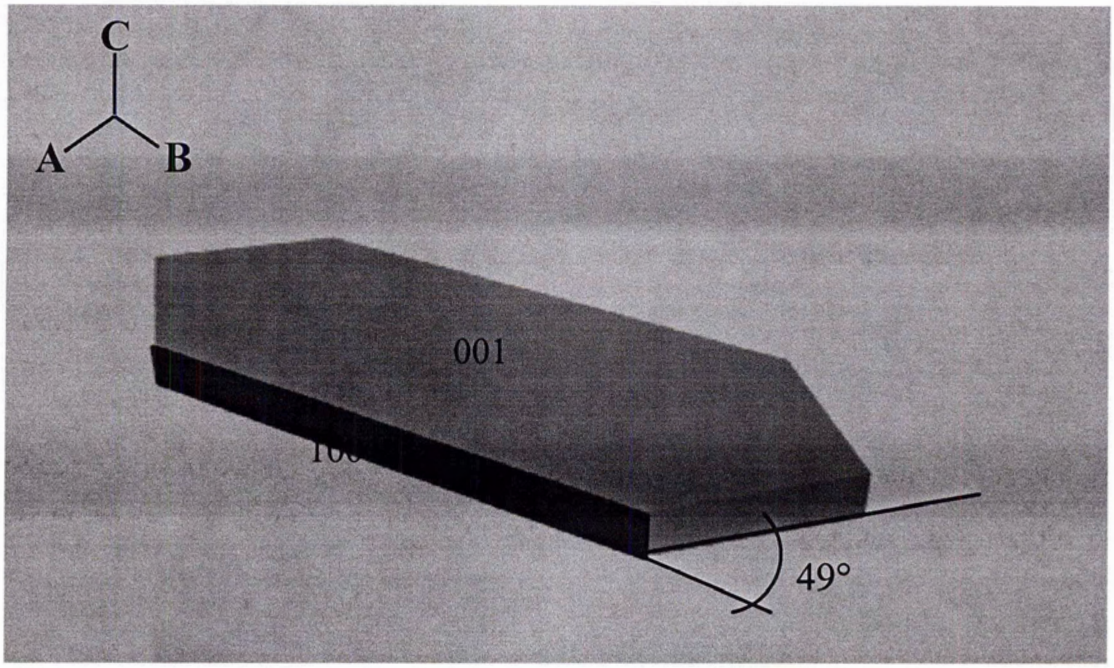

Figure 4-5 - Pictorial representation of an L-diammonium tartrate crystal on a L-cysteine monolayer calculated from Shape® software. The (001) face is the large, elongated face on the surface of the crystal. The side face, (100), is shown highlighted.

The shape description of the Class F crystals matches the majority of the L-diammonium tartrate crystals in the statistical survey. An example is shown in Figure 4-4. A simulated depiction of an L-diammonium tartrate crystal, calculated from crystal parameters (CCDC REFCODE: AMTART11[123]) and applying varying growth rates, is characterized in Figure 4-5. The large surface face corresponds to the (001) face, as shown by the representation of the calculated Shape® graphic. The elongated sides of the crystal relate to (100) faces. Angle measurements calculated from Shape®, as seen in Figure 4-5, lie within a few degrees of the angles measured on SEM images, as seen in Figure 4-4.

Table 4-2 - Ratio of growth rates used in Shape® software to simulate L-diammonium tartrate crystal on L-cysteine monolayer

Crystal Form	Growth Rate Ratio
(001)	1
(100)	4
(10-1)	6
(101)	6
(01-1)	19
(110)	12

The ratio of rate constants used in Shape® to simulate the Class F crystal of this system is given in Table 4-2.

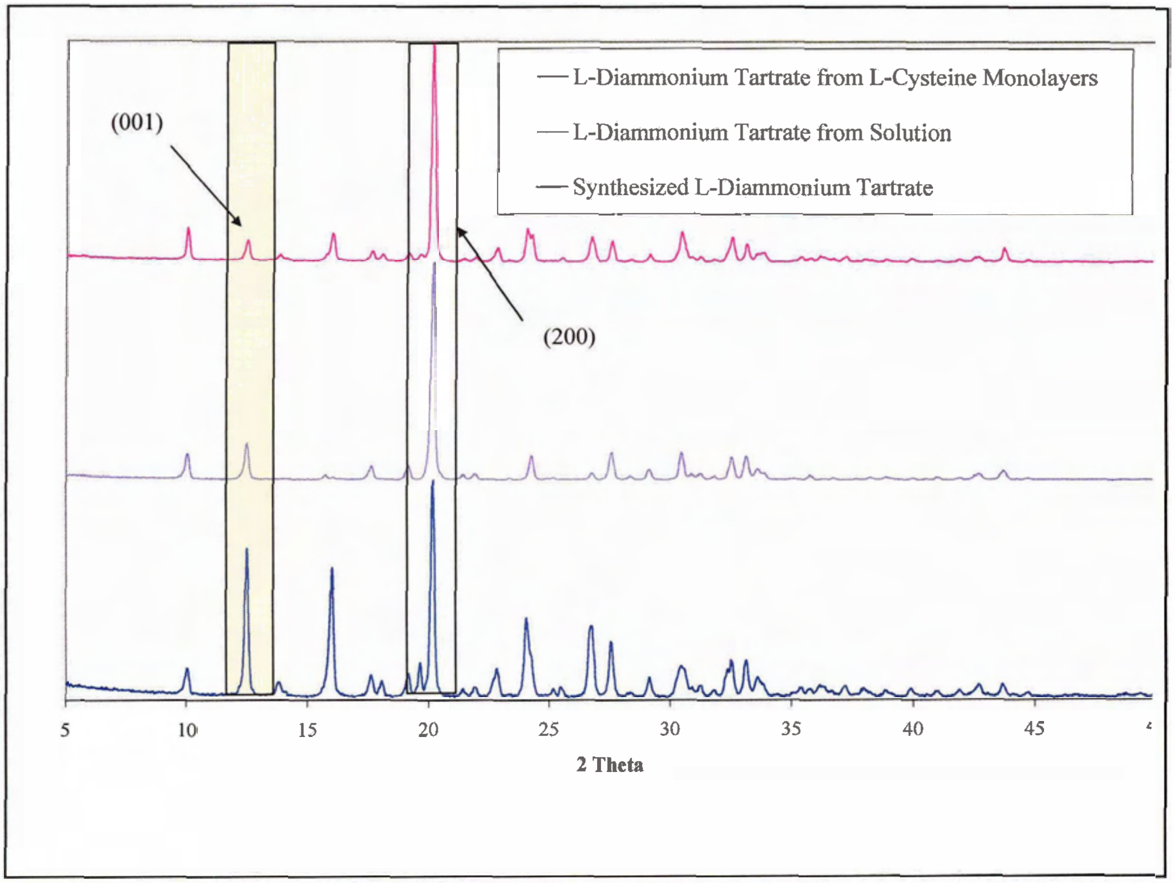

Figure 4-6 - Comparison XPD spectra of L-diammonium tartrate from three stages of experimental work.

Figure 4-6 is a comparison of the XPD spectra of the crystals scraped from the slides with monolayers, crystals taken from the crystallizing tray, and crystals of synthesized L-diammonium tartrate. The top spectrum is attained by collecting the XPD data from crystals that were physically removed from the Au (111) slides. The middle spectrum is comprised of XPD data from excess bulk crystals that were removed from the crystallizing tray after evaporation trials were concluded. Finally, the bottom spectrum is an XPD spectrum of the synthesized diammonium tartrate after recrystallization. Simulated XPD for the bulk diammonium tartrates were also produced for comparison (see Figure 4-18).

The yellow highlighted area in Figure 4-6, corresponding to the (001) crystal planes, indicates a decrease in strength of signal between the synthesized L-diammonium tartrate and both of the crystals from monolayer and crystals from solution. This indicates that in both of the latter cases; the face corresponding to the peak would be larger in viewable area due to a slower growth rate and, ultimately, fewer planes of that specific direction for x-ray diffraction. This finding is supported by previous evidence from optical techniques that L-diammonium tartrate crystals are extremely needlelike in appearance[124] rather than the observed crystals of this system which featured flat elongated faces in plate like crystals. Similar evidence has been cited to explain the visible changes to the crystal structure of calcium carbonate, between calcite and argonite, have been attributed to the growth of the crystals in the presence of compressed Langmuir monolayers[125]. Control over the crystallographic orientation of crystallized calcite from solutions of calcium chloride by using different functional groups and substrates to produce crystals with an altered orientation has been reported by Aizenberg and coworkers[126].

The simulated XPD for L-diammonium tartrate crystals has a relative intensity of 55 for the (001) peak which corresponds with the intensity of 68 for the (001) peak of the synthesized L-diammonium tartrate. In comparison, the crystals from the monolayers and crystals recovered from the evaporated solution have relative intensities of 10 and 17, respectively. Further verification is provided by the statistical survey that showed overwhelming majority of L-diammonium tartrate crystals grown on L-cysteine monolayers followed a Class F resemblance, as indicated in Figure 4-2, with a large surface parallel to the surface.

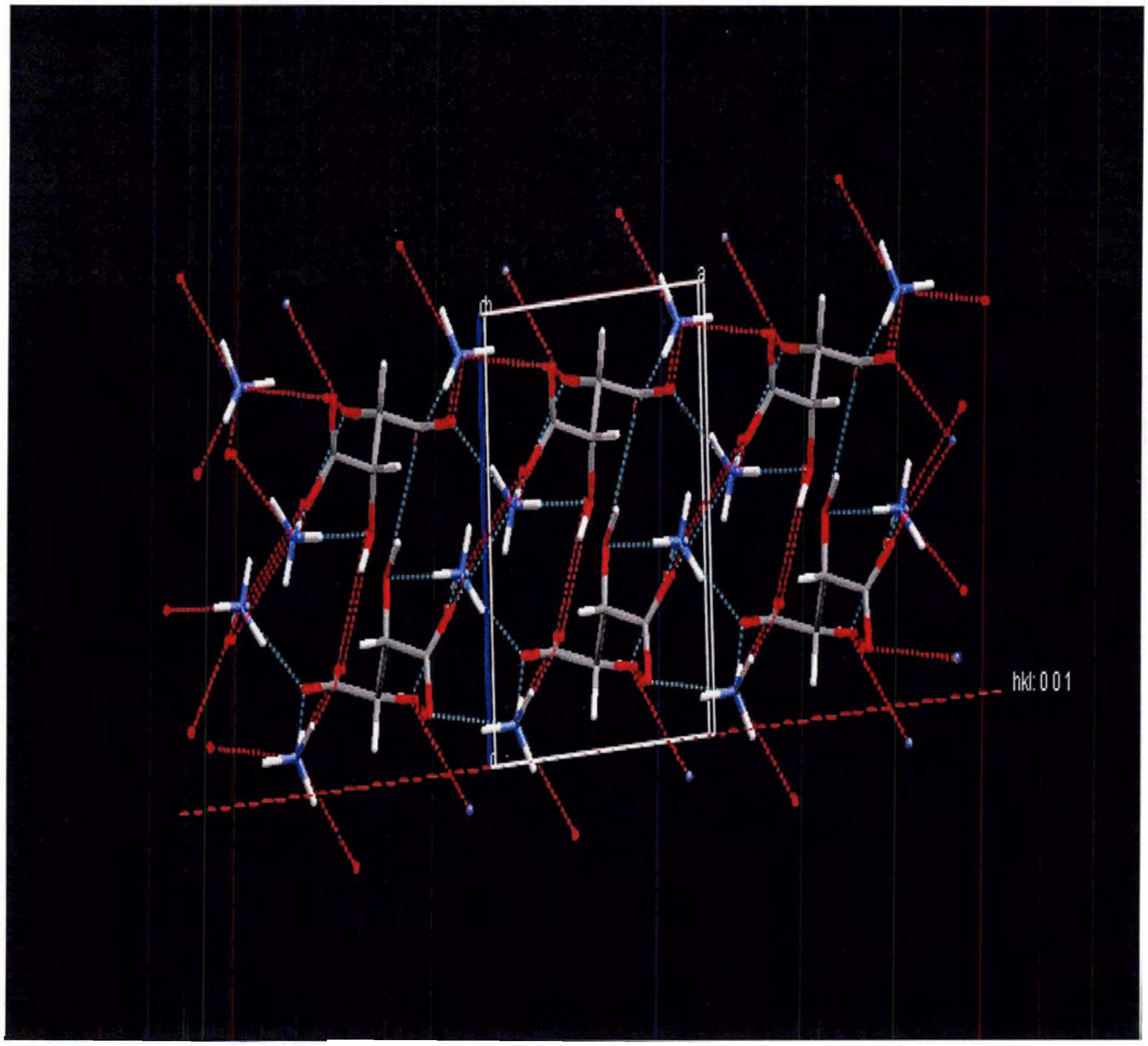

Figure 4-7 – Expanded L-diammonium tartrate unit cell. Unit cell is viewed along the (001) plane.

SEM images (Figure 4-4), crystal modeling through Shape® (Figure 4-5), and the statistical analysis (Figure 4-2) have indicated that the interactive crystallographic face for the L-diammonium tartrate with the L-cysteine monolayer is the (001). XPD data (Figure 4-6) presented a strong peak for the (002) plane. Examining the unit cell for L-diammonium tartrate it is clear that the (002) and the (001) faces would interact with the monolayer in an identical fashion. The molecular arrangement of the tartrate and ammonium ions in the unit cell can be viewed in Figure 4-7. When viewing the L-diammonium tartrate unit cell along the *a* or *b* axis, there is a high probability for supramolecular interactions along this plane. Due to the chirality of both the crystallizing substance and SAM, molecular interaction models will be similar for homomeric systems when considering specific planes.

The *a* and *b* dimensions of the L-diammonium tartrate unit cell are 7.083 Å and 6.128 Å, respectively. This indicates a strong possibility for four full cysteines to interact with each L-diammonium tartrate unit cell, as the sulfur headgroups are ~5 Å apart on the Au surface[33]. This 4:1 molecular interaction ratio, indicated in Figure 4-8, also supports the intramolecular theory that chiral SAMs adsorb to the energetically favorable bilayer formation[127-129]. The close knit bilayer formation of the monolayer may also lead to some partial hydrogen bonding from the neighbors of the two cysteines that are expected to interact with the diammonium tartrate.

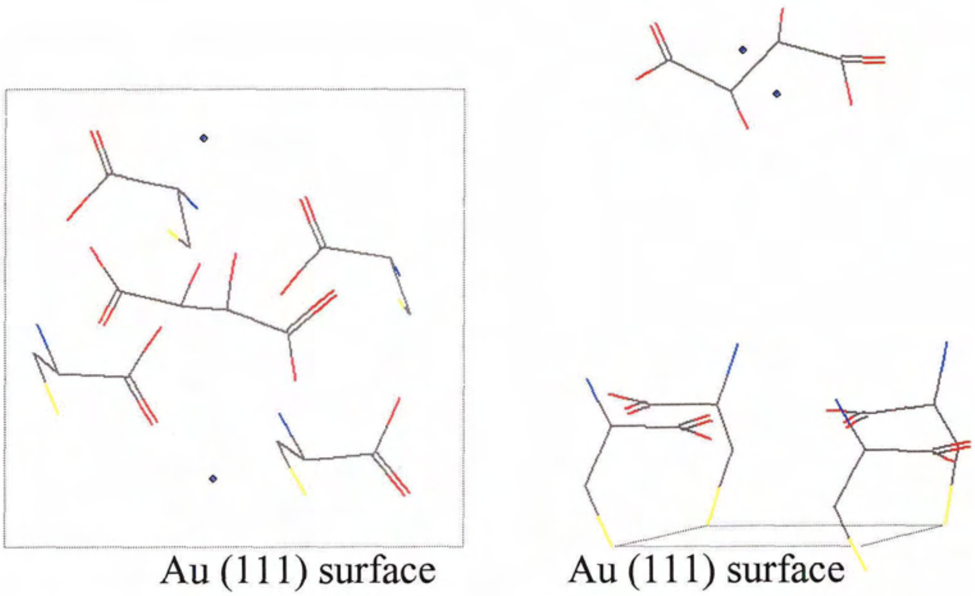

Figure 4-8 - Top and side views of L-cysteine adsorbed on the surface on Au (111) with the relative position of L-diammonium tartrate indicated. The distance between the tartrate and monolayer has been exaggerated in order to simplify viewing of the model. The h

The arrangement of the molecules in the L-diammonium tartrate unit cell at the (001) plane is also sterically appropriate for intermolecular bonding with the adsorbed L-cysteine. This is because the molecules that are directly capable of bonding are lying within the restrictions for hydrogen bonding in terms of distance. The upper limits for CH----O hydrogen bonding is around 4 Å, and for NH---O and OH---O bondings the limit is 3.5 Å. This was as well noted in the case of calcium carbonate crystallization[125]. The change in the nucleation face which ultimately interacted with the compressed Langmuir monolayer and caused the shift between calcite and aragonite crystallization, was attributed to the sterically determined match between the groups in the crystallizing substance and the various tail groups of the monolayer[125].

The moieties capable of hydrogen bonding are all located approximately within the same plane, allowing for interactions of the (001) plane of the L-diammonium tartrate crystal with the L-cysteine monolayer. The even offset of hydrogen bonding atoms from the cell edge allows generous space for both the carbon tartrate backbone and the ammonium molecule to achieve a hydrogen bond network between the hydrogen atoms and nitrogen or oxygen atoms, within the optimum value of ~2.6 Å[130]. Bearing these conditions in mind, a suitable match between the (001) plane of the L-diammonium tartrate and four adsorbed L-cysteine molecules can be modeled in 3D, as indicated in Figure 4-9.

The possible hydrogen bonding interactions between the (001) crystal plane of L-diammonium tartrate and the L-cysteine SAM can be broken down into three essential groups. These are (1) interactions making use of the deprotonated tartrate carboxyls, as hydrogen bond acceptors (HBAs), and the protonated amino groups of the cysteine, as hydrogen bond donors (HBDs), (2) intermolecular interactions employing the deprotonated cysteine carboxyl as the HBA and the ammonium ion as a HBD and (3) bonding between the hydroxyl group of the tartrate backbone as the HBD and the deprotonated carboxyl of the cysteine monolayer as the HBA. However, there is a hydrogen bond network required for the growth and stability of the crystal. This indicates that the hydrogen bonds with the cysteine monolayer will form to replace bonds that would have formed to the next molecule in the crystal, had the crystal continued in the direction of the (001) plane.

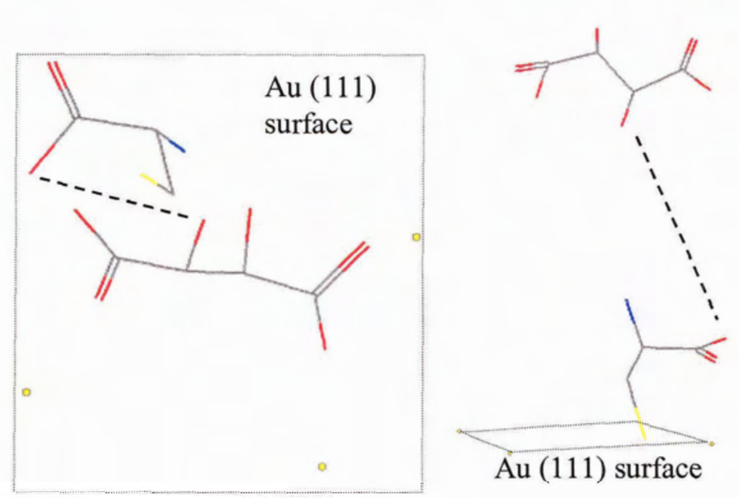

Figure 4-9 - Partial view of L-diammonium tartrate (in the (001) plane) on L-cysteine SAM. Carboxylate-hydroxyl hydrogen bonding is indicated with black dashed line. The distance between the tartrate and monolayer has been exaggerated in order to simplify viewing of the model. Yellow circles indicate sulphur atoms of the other L-cysteine molecules of the unit cell. The hydrogen atoms were omitted for clarity.

The last of the interactions is the most important to the system and provides reasoning for chiral separation by crystallization. There are two hydroxyl groups on the tartrate backbone, but only one is positioned with the hydrogen atom facing the monolayer, as indicated in Figure 4-9. In the case of L-diammonium tartrate, the hydroxyl that faces the monolayer is sterically positioned to interact with a carboxylate from L-cysteine. It is the positioning of these two moieties, which is ultimately based on chirality that determines the enantioselectivity of the system. The intermolecular interaction, specifically hydrogen bonding, was attributed to the preferential crystallization of malonic acid on monolayers functionalized with a carboxylic acid group[73]. Hydrogen bonding between the CO_2^- and NH_3^+ of glycine and the hydroxyl groups of the SAMs were also accredited with the preferential crystallization of glycine[81].

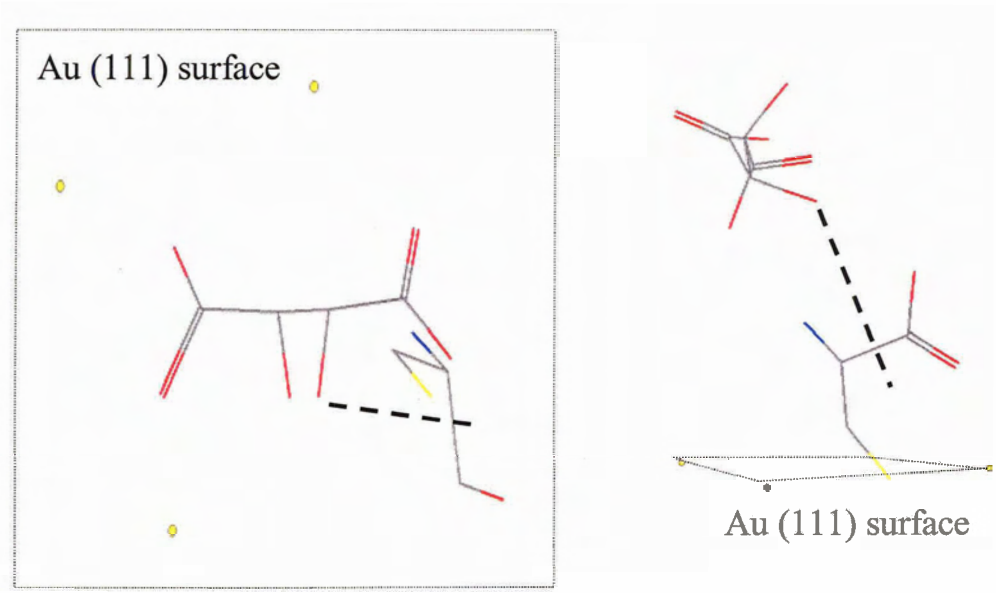

Figure 4-10 - Interaction model of L-diammonium tartrate on D-Cysteine. Lack of hydroxyl group hydrogen bonding is highlighted with dashed arrow. The distance between the tartrate and monolayer has been exaggerated in order to simplify viewing of the model. Yellow circles indicate sulphur atoms of the other L-cysteine molecules of the unit cell. The hydrogen atoms were omitted for clarity.

For comparison purposes, the interaction between the L-diammonium tartrate and D-cysteine was modeled and is shown in Figure 4-10. In the first case, there is no hydroxyl to carboxylate hydrogen bonding. This indicates that the hydroxyl interaction is specific to a better match. Other homomeric specific crystallization systems have been reported elsewhere[93]. The comparison interaction scheme (L-diammonium tartrate on L-cysteine) summarized in Figure 4-8 and Figure 4-9 provides evidence of the major role of the hydroxyl orientation on the crystallization of L-diammonium tartrate on cysteine monolayers.

This model of interaction for L-diammonium tartrate on L-cysteine monolayers is also in agreement with previous STM work that indicated that the sulfur headgroups are ~ 5 Å apart[58]. The arrangement of cysteine molecules on the surface also supports attractive interactions between the tail groups of the cysteine molecules. This proposed model is in good agreement with all system analysis techniques, satisfies the steric requirements for hydrogen bonding and on the most basic level, provides reasoning for crystal growth on monolayer prepared slides when compared to bare gold slides.

4.3 D-Diammonium Tartrate on L-Cysteine Monolayers

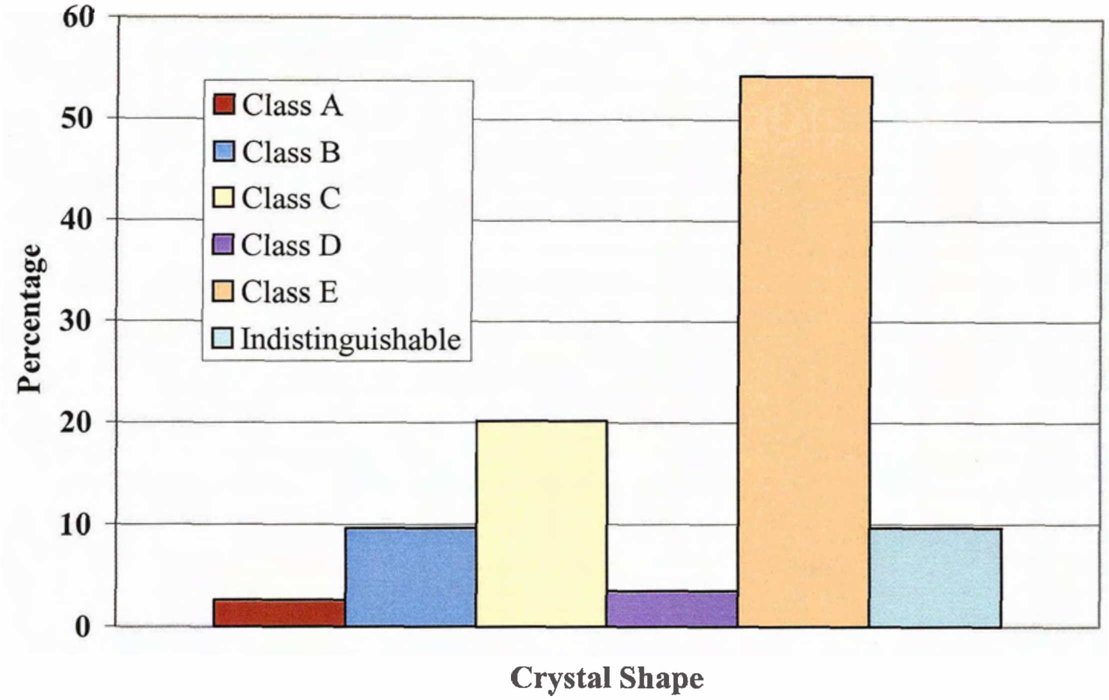

Figure 4-11 - Percentage distribution of shapes for D-diammonium tartrate crystals on L-cysteine monolayers

Over half of the classified crystals in this system fell under the Class E category. The characteristics of Class E crystals are defined in Table 3.2. From an overall statistical population of 114 crystals, 62 of the D-diammonium tartrate crystals were classified as Class E, as denoted by Figure 4-11. The second most populated statistical bin was that of Class C crystals, which held 23 crystals. A mere 11 D-diammonium tartrate crystals from the population were classified as Indistinguishable. Noting that over 90% of the crystals included in the statistical survey grew with a well-defined overall shape indicates a strong level of interaction between the molecules in the crystal and the monolayer. The average crystal size was 344 ± 288 μm and the crystal density was found to be 1.2×10^{-3} crystals/μm^2. Polarimetry analysis of the crystals in this system produced a result of -0.048°; this direction of the rotation of the plane polarized light is expected since the crystallizing substance was a pure enantiomer form. The histogram of crystal sizes, shown in Figure 4-12, revealed no obvious statistical distribution. As Figure 4-12 indicates, statistical bins for 220-240 μm and 280-300 μm both contained the largest quantity of crystals. The average crystal size in this system exceeds that of crystals in other tartrate/monolayer systems. The larger average size per crystal does account for the decreased population size of the D-diammonium tartrate crystals when compared to the other crystal systems studied. An increased crystal growth rate can be attributed to the agreement between the monolayer and the crystalline phase[73]. However, as discussed in section 4.1, this agreement there may be fewer interaction points between the tartrate molecules and the monolayer in the heteromeric system – see Figure 4-10. The intermolecular match between D-diammonium tartrate and L-cysteine will be investigated further in this section.

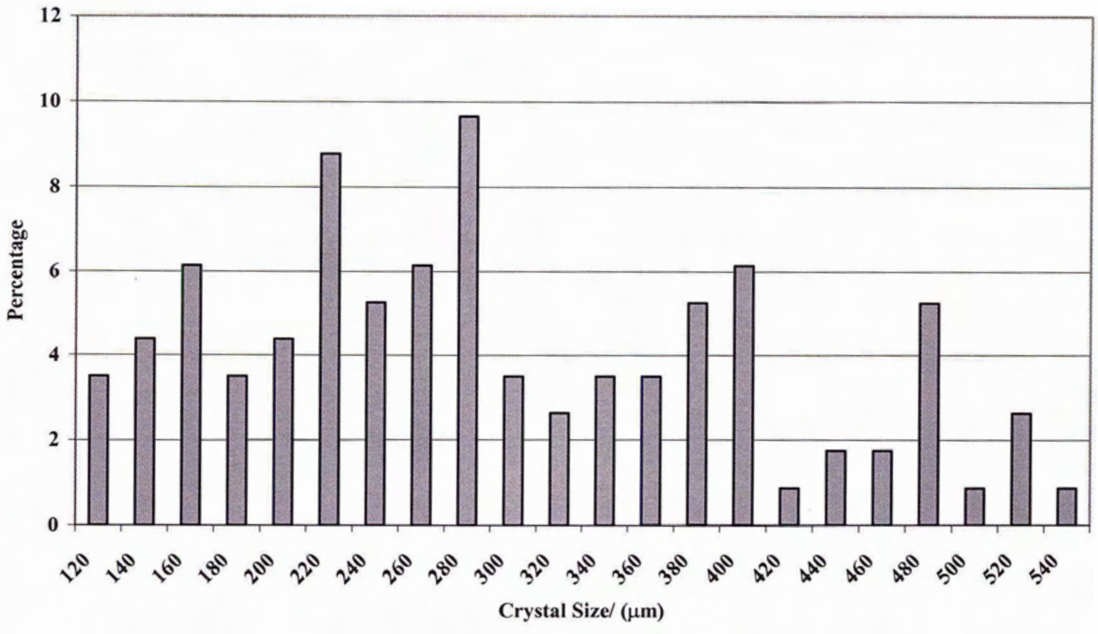

Figure 4-12 - Size percentage distribution for D-diammonium tartrate crystals on L-cysteine monolayers

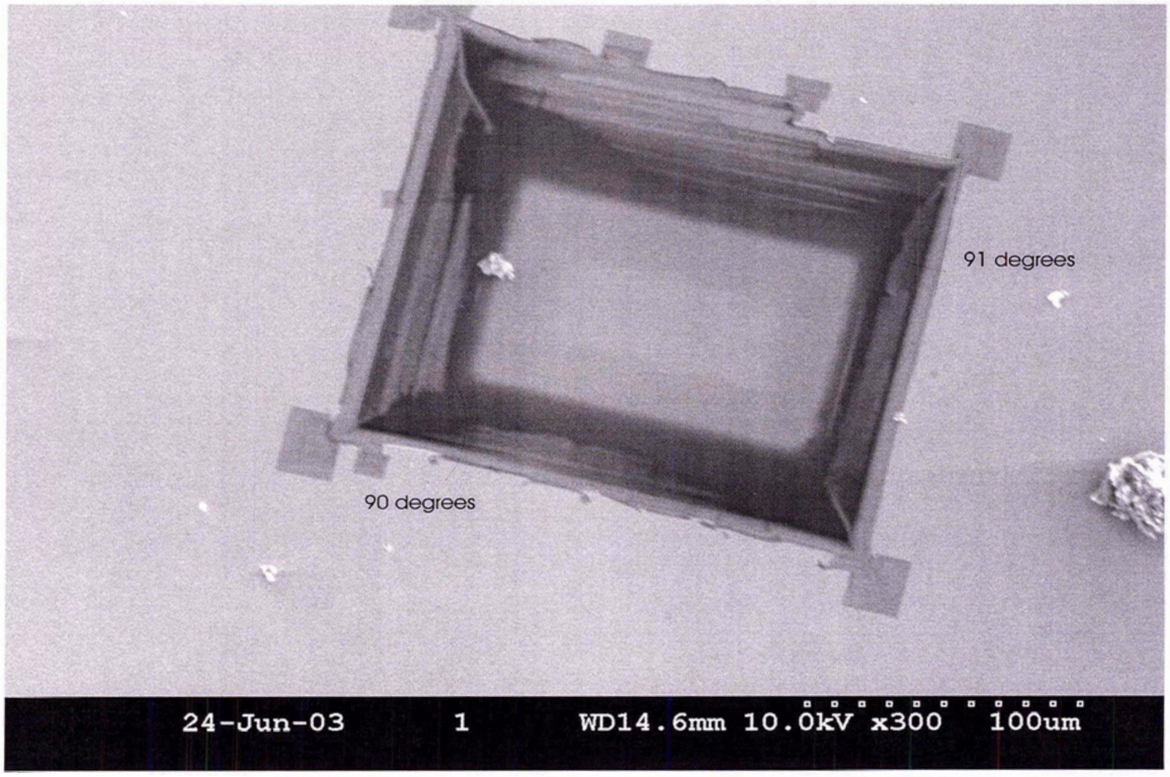

Figure 4-13 – SEM image of an D-diammonium tartrate crystal on L-cysteine monolayer

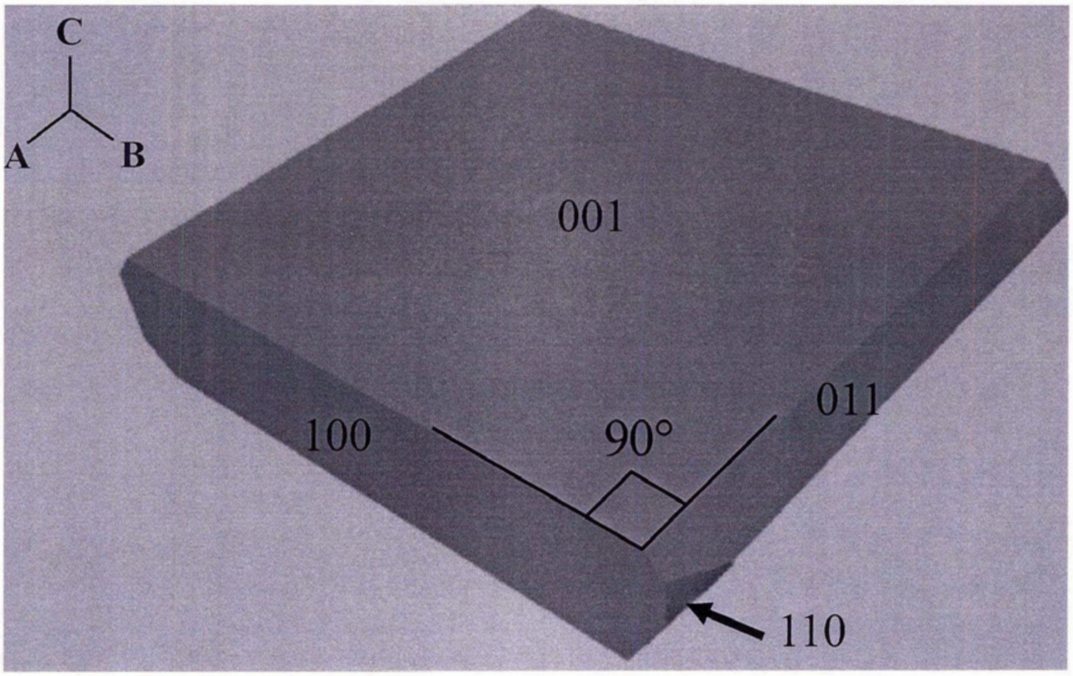

Figure 4-14 - Depiction of Class E crystal from Figure 4-13.

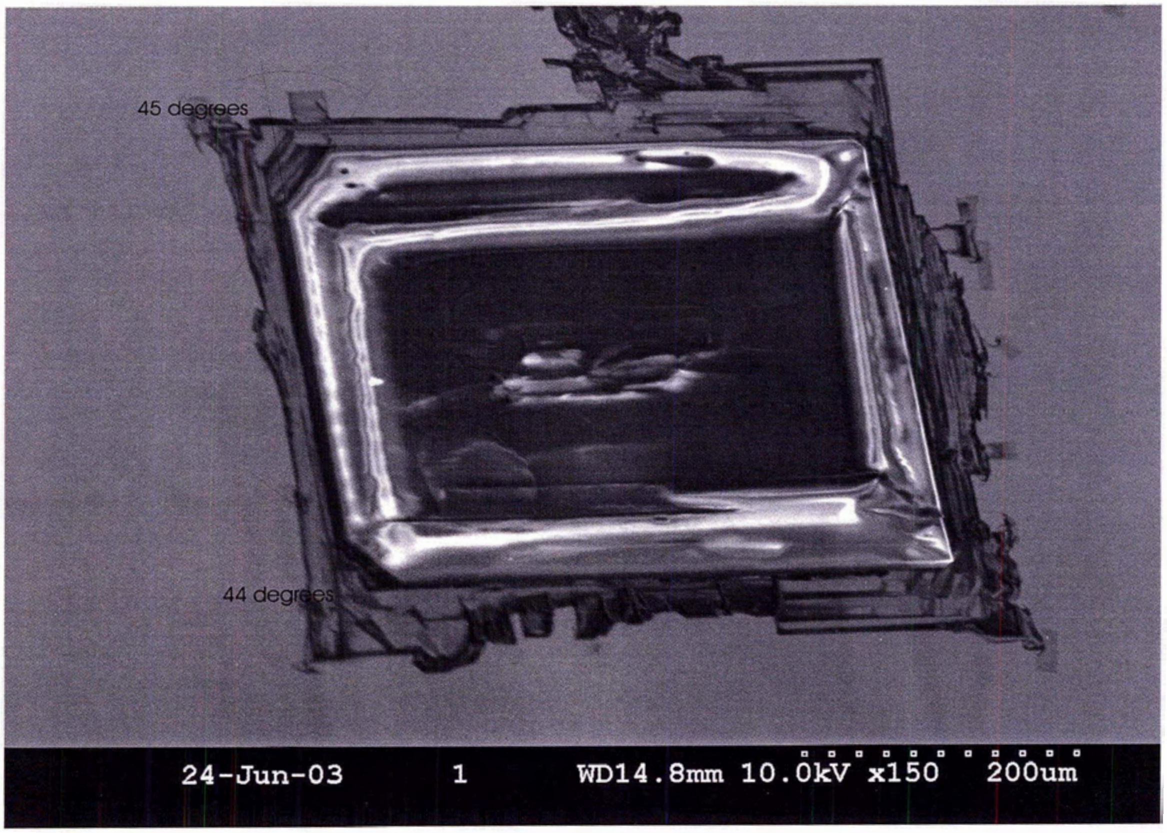

Figure 4-15 – SEM image of an D-diammonium tartrate crystal from L-cysteine monolayer

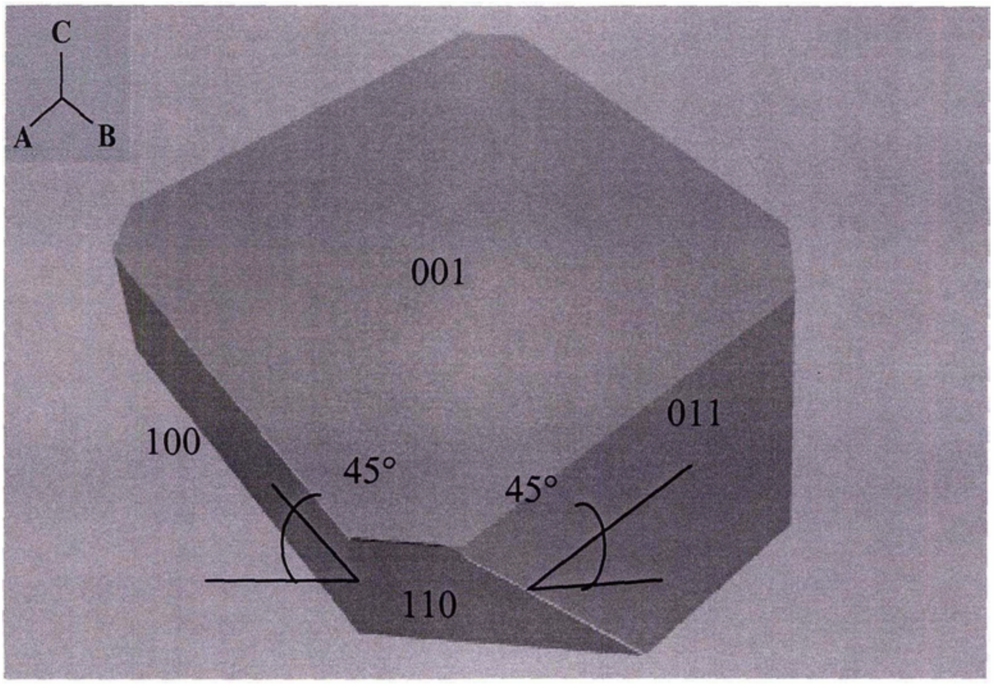

Figure 4-16 - Depiction of Class E crystal from Figure 4-15.

While Class E crystals dominated this statistical set, two of the Class E subcrystal types were present. Figure 4-13 is a SEM image of one of the two subclassifications identified. The four corners of these crystals are ~ 90°, which are indicated in Figure 4-13 and on the simulation of the crystal in Figure 4-14. The other subclassification of the dominant Class E is represented by the crystal in the SEM image Figure 4-15. This subclass is related to the first in that it has the same overall shape with the exception being that the corners are now blunted with interfacial angles of ~ 45°. The blunted crystals corners are indicated in Figure 4-15 and exaggerated in Figure 4-16.

Table 4-3 - Ratio of growth rates used in Shape® software to simulate D-diammonium tartrate crystal on L-cysteine monolayer

Crystal Form	Growth Rate Ratio	
(00-1)	1	
(100)	3	
(10-1)	12	
(101)	12	
(01-1)	3.5	
(0-11)	3.5	
(110)	5 (Figure 4-14)	4.5 (Figure 4-16)
(-1-10)	5 (Figure 4-14)	4.5 (Figure 4-16)

The effect of the blunted corners can be visualized by applying various growth rates to the faces of the crystal simulated in Shape® (crystal parameters referenced in CCDC REFCODE: AMTART11[123]). The ~ 90° angles of Figure 4-13 and Figure 4-15 are attained by applying a faster growth rate to the (110) face. The ratio of the growth rates used to simulate the crystals in Figure 4-14 and Figure 4-16 are shown in Table 4-3. Decreasing the growth rate for the (110) face to 4.5 in Table 4-3 yields Figure 4-16. The (110) face then becomes visible and accounts for the ~ 45° angles measured in Figure 4-15.

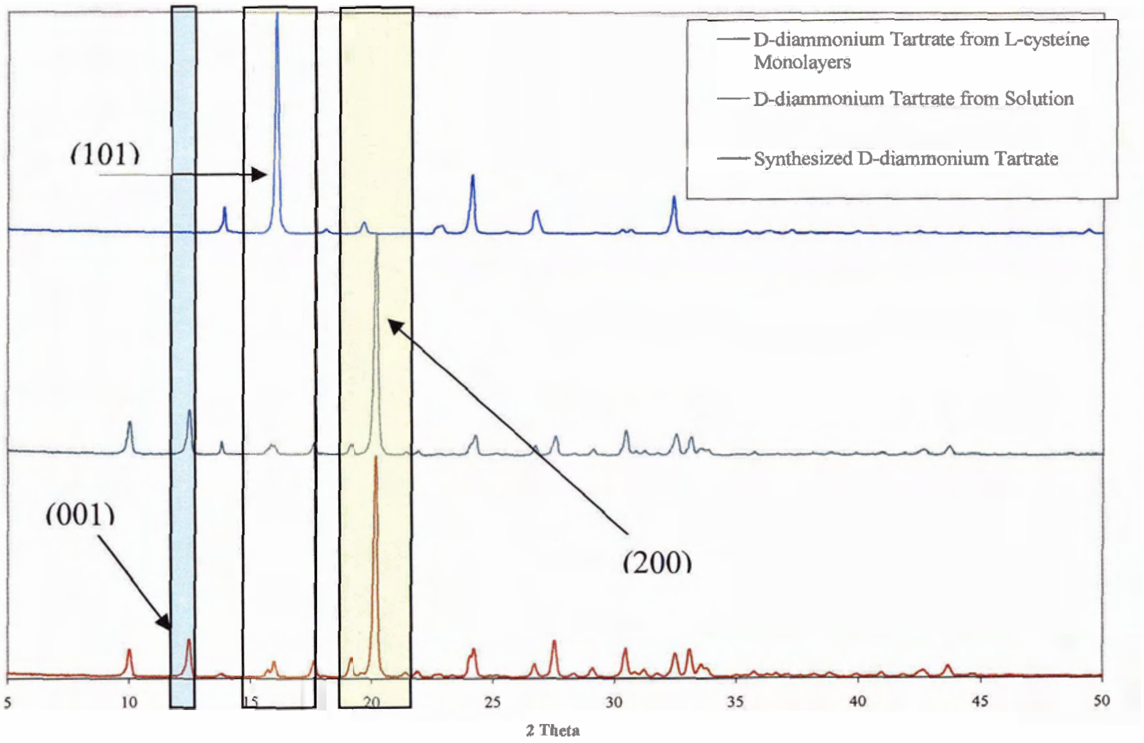

Figure 4-17 - Comparison XPD spectra of D-diammonium tartrate from three stages of experimental work

Figure 4-17 is a comparison of the XPD data collected, showing spectra of the crystals scraped from the slides with monolayers, crystals taken from the crystallizing tray, and the synthesized D-diammonium tartrate. The peaks at ~ 20° corresponds to the (200) planes of diammonium tartrate and is by far the strongest peak in both of the spectra for synthesized D-diammonium tartrate and D-diammonium tartrate from solution. However, taking note of the yellow highlighted portion of Figure 4-17 for the same two spectra, the peak indicating a strong presence of (101) planes is absent. Instead, in this area of Figure 4-17, the strongest peak corresponds to a (101) plane for D-diammonium tartrate from L-cysteine monolayers. The simulated crystals in both Figure 4-14 and Figure 4-16 were produced using comparatively high growth rates for the (101) face, as shown in Table 4-3.

The SEM images and modeling suggest that the (001) face is viewed when looking perpendicular to the monolayer surface normal. The XPD data confirms this suggestion in that the blue area corresponding to the (001) region in Figure 4-17 lacks a peak at ~ 12° for the D-diammonium tartrate crystals from L-cysteine slides where a peak would be expected. This peak is expected in the top spectrum of Figure 4-17 due to its presence in both the synthesized D-diammonium tartrate and the D-diammonium tartrate recovered from solution. The disappearance of this peak in the top spectrum of Figure 4-17 can be explained if there are few of these planes in each of the crystals. This explanation also accounts for the dendritic growth in the SEM images, which is present around the crystal in Figure 4-13 and Figure 4-15. The growth rate in directions parallel to the surface is faster in comparison to the perpendicular growth ((001)-direction) which leads to dendritic crystal growth. In order to explain the growth of the crystals from the (001) plane, the intra- and intermolecular interactions between D-diammonium tartrate and L-cysteine must be examined.

Crystal modeling, SEM and XPD all point to the (001) plane as being the interactive plane with the SAM. The intermolecular interactions between the D-diammonium tartrate unit cell and the L-cysteine SAMs are similar to the interfacial interactions outlined earlier in section 4.1 for the L-diammonium tartrate on D-cysteine (Figure 4-10).

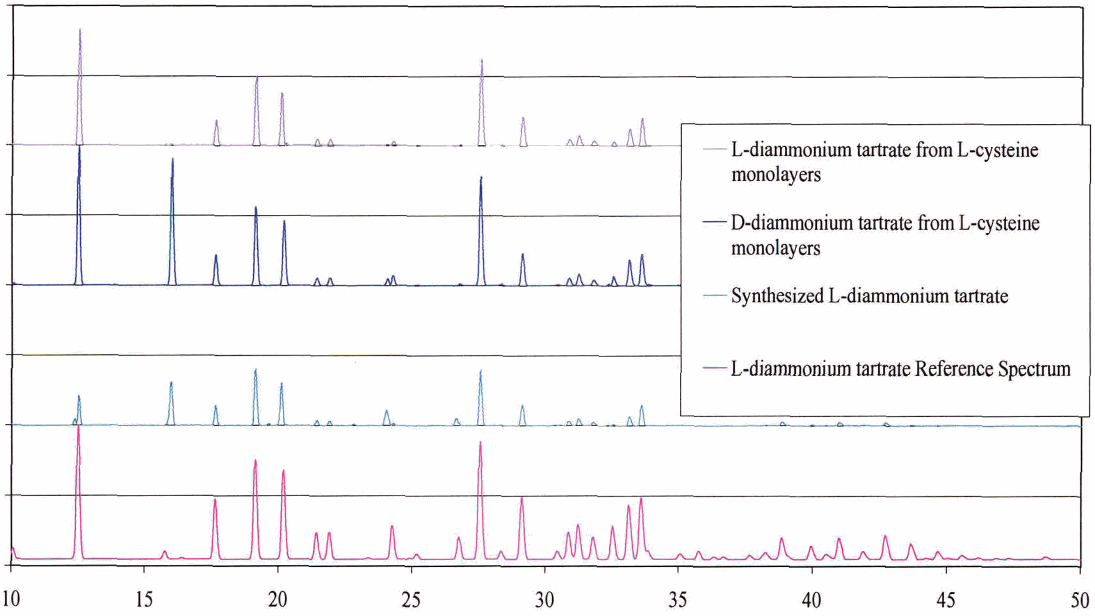

Figure 4-18 - Comparision of XPD spectra from all enantiomers of diammonium tartrate various stages of experimental procedure.

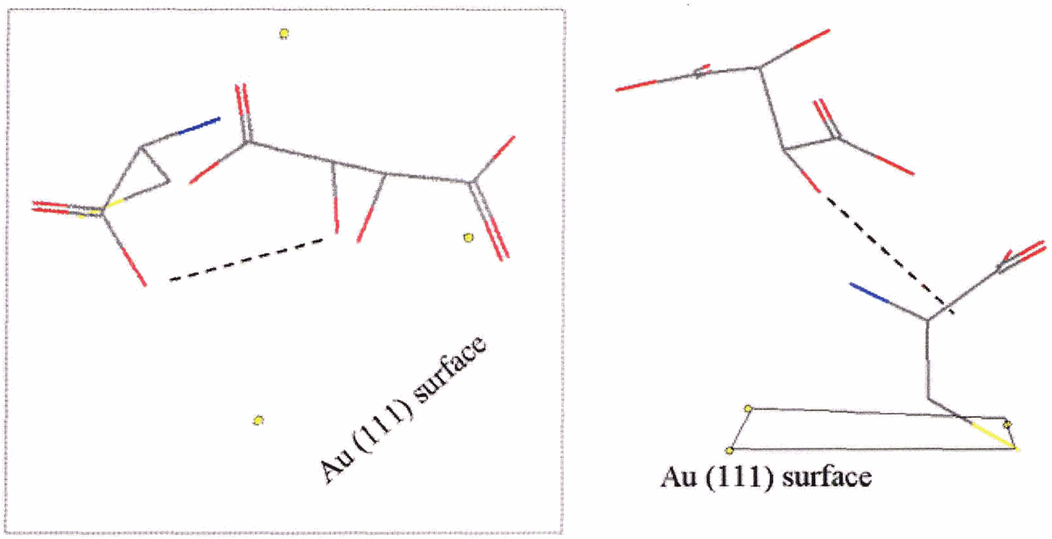

Figure 4-19 - Three dimensional molecular interaction model for D-diammonium tartrate on L-cysteine. Hydroxyl group hydrogen bonding is indicated by a dashed line. The distance between the tartrate and monolayer has been exaggerated in order to simplify viewing of the model. Yellow circles indicate sulphur atoms of the other L-cysteine molecules of the unit cell. The hydrogen atoms were omitted for clarity.

The spectra in Figure 4-18 indicate that the D-diammonium tartrate unit cell dimensions are very similar for L-diammonium tartrate because the pattern of the spectra for one matches the pattern for the other. The discrepancy between these spectra occurs at ~ 16° (16.4° for the L-diammonium tartrate reference spectrum and 16.0 for the synthesized L-diammonium tartrate/ D-diammonium tartrate from L-cysteine monolayers), which is more than likely due to a small contamination. The specific dimensions of L-diammonium tartrate on L-cysteine have been discussed previously. The interaction model proposed for D-diammonium tartrate on L-cysteine follows a similar pattern to that of L-diammonium tartrate in D-cysteine (Figure 4-10) and can be identified by the number of appropriate interactions that can occur between the tartrate and the monolayer based on steric orientation. Figure 4-19 depicts the proposed interaction between the D-diammonium tartrate and the L-cysteine monolayer.

In comparing this interaction system to that proposed for L-diammonium tartrate on L-cysteine (Figure 4-10), it is apparent that as a result of the differences in the interactions and in the specific orientation of the tartrate salt on the L-cysteine monolayer that a change in the overall crystal shape is possible. It is also important to note that even though the interaction face of the unit cell remains consistent in both systems, a change in the dominant crystal shape occurs. These results are supported by XPD, modeling and SEM images. The superior quantity of interactions in the homomeric systems, compared to the heteromeric systems, offers support to the results obtained by others, such as the preferential binding of D-leucine to D-leucine on a SAM of 11-mercaptoundecanoic acid[93].

4.4 DL-Diammonium Tartrate on DL-Cysteine

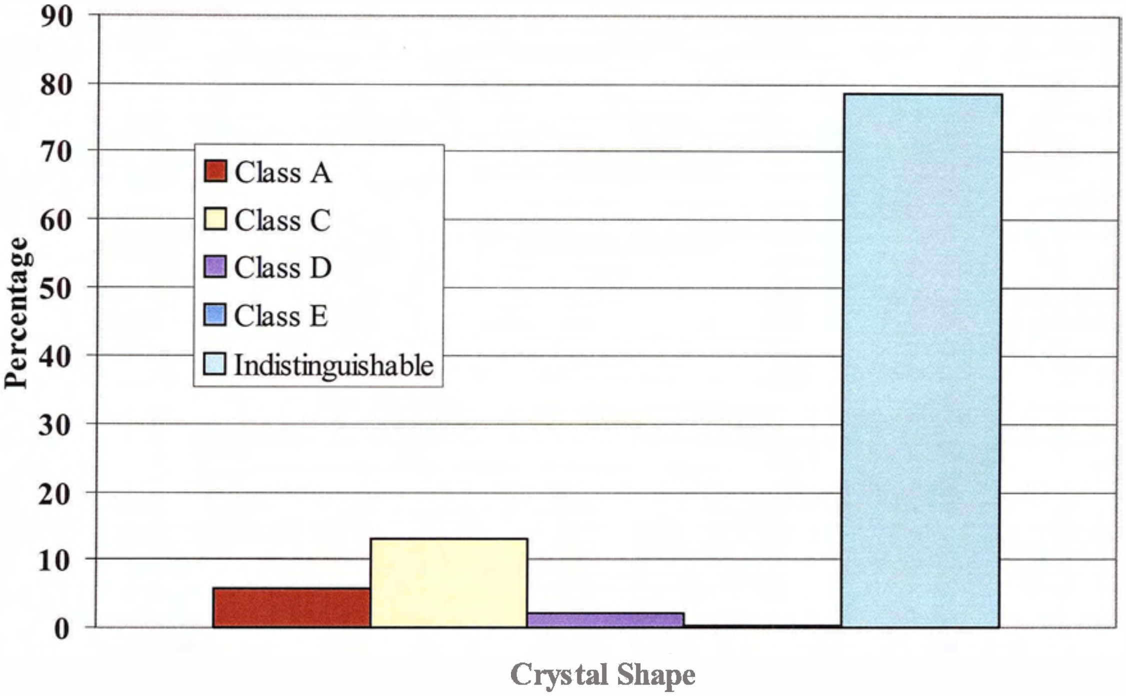

Figure 4-20 - Percentage distribution of shapes for DL-diammonium tartrate crystals on DL-cysteine monolayers.

An overwhelming percentage of the crystals in this system were indistinguishable in shape, as seen in Figure 4-20. The population size for this system was 1187 crystals. Of these, 933 were classified as Indistinguishable and the next most populated category was Class C with 155 crystals. This indicates the interaction between the monolayer and the molecules of the tartrate is weak and does not produce a relatively large number of crystals with a defined orientation. As shown in Figure 4-21, the majority of crystals populated the 70-80 μm size range, with an average crystal size of 101 ± 42 μm. The small average size of the crystals and the large amount of crystals suggests that nucleation was favored in the crystallization process of the tartrate crystals.

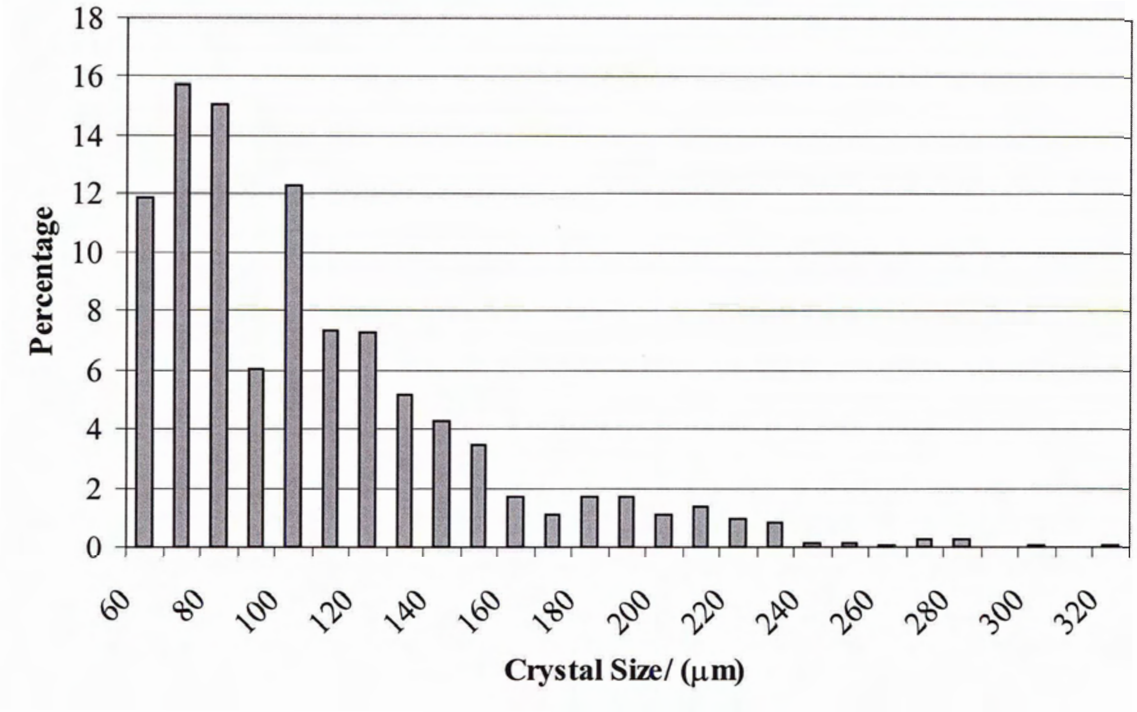

Figure 4-21 - Size percentage distribution of DL-diammonium tartrate crystals on DL-cysteine monolayers

Enantiomers of a racemic monolayer will tend to adsorb onto the surface in clusters to decrease strain on the overall monolayer. On the surface, if like enantiomers adsorb together in small domain areas, the overall energy of the monolayer will be decreased due to the compatibility of the intramolecular interactions[131]. This as well will create regions where the monolayer is organized and boundaries between these organized domains where defects are predominant. When pure enantiomers adsorb onto a surface, the conformation of the substituents is the same and the monolayer can organize itself easily to the lowest energy possible.

The overall small average size of the crystals in this system presented an unexpected hurdle. While removal of the crystals from the gold substrates was possible to a certain degree despite the small size, collection of a usable amount was impossible. Therefore, no XPD analysis could be performed on this system.

Although XPD data was unavailable, the characteristics of the crystals and the growth rates of the faces within them were scrutinized using Shape® software and properties provided by the Cambridge Crystallographic Database (CCDC REFCODE: ZZZJII01[132]). The majority of the crystals in this system were misshapen and indistinguishable from one another, but the crystals that were classified provided a range of various shapes.

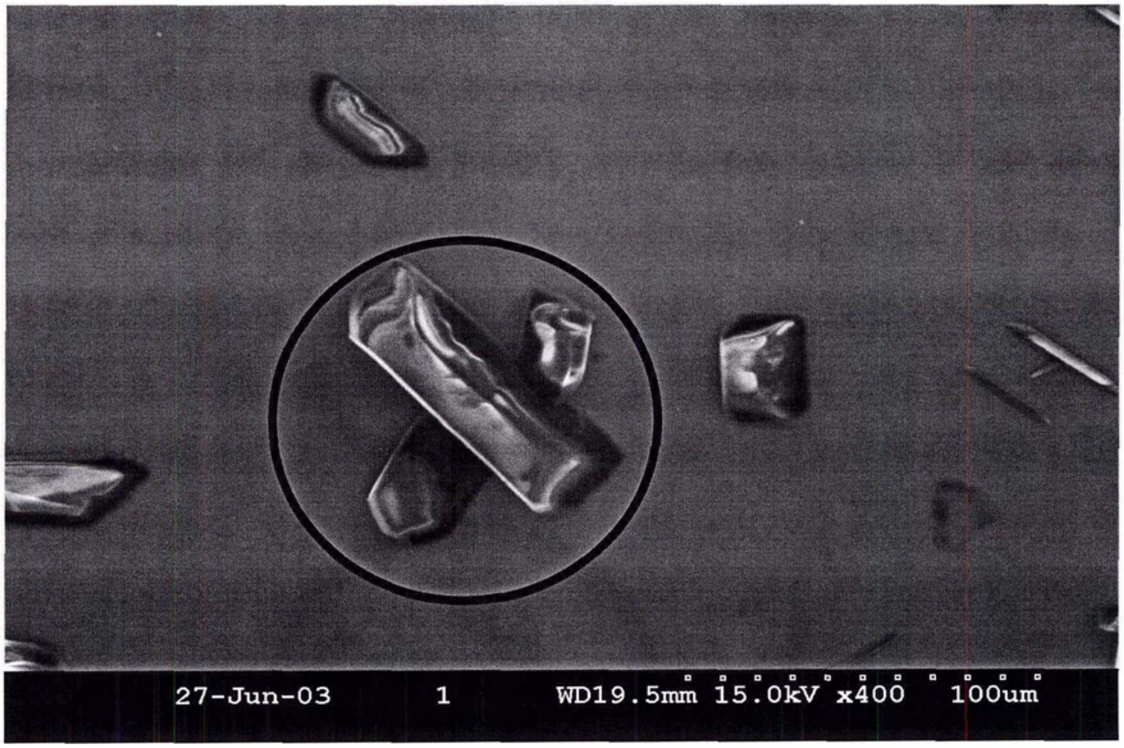

Figure 4-22 - Class E representative DL-diammonium tartrate crystal from DL-cysteine monolayer.

The crystal highlighted by a circle in Figure 4-22 is representative of a Class E crystal. The crystal was simulated in Shape® using the growth rate ratios in Table 4-4.

A depiction of this can be seen in Figure 4-23 along with notation as to the faces identified during manipulation.

Table 4-4 - Ratio of growth rates used in Shape® software to simulate Class E DL-diammonium tartrate crystal on DL-cysteine monolayer.

Crystal Form	Growth Rate Ratio
(01-1)	1
(020)	0.75
(02-1)	3.5
(100)	0.5
(00-2)	8.1
(03-1)	8.6
(110)	0.5
(01-2)	9.1

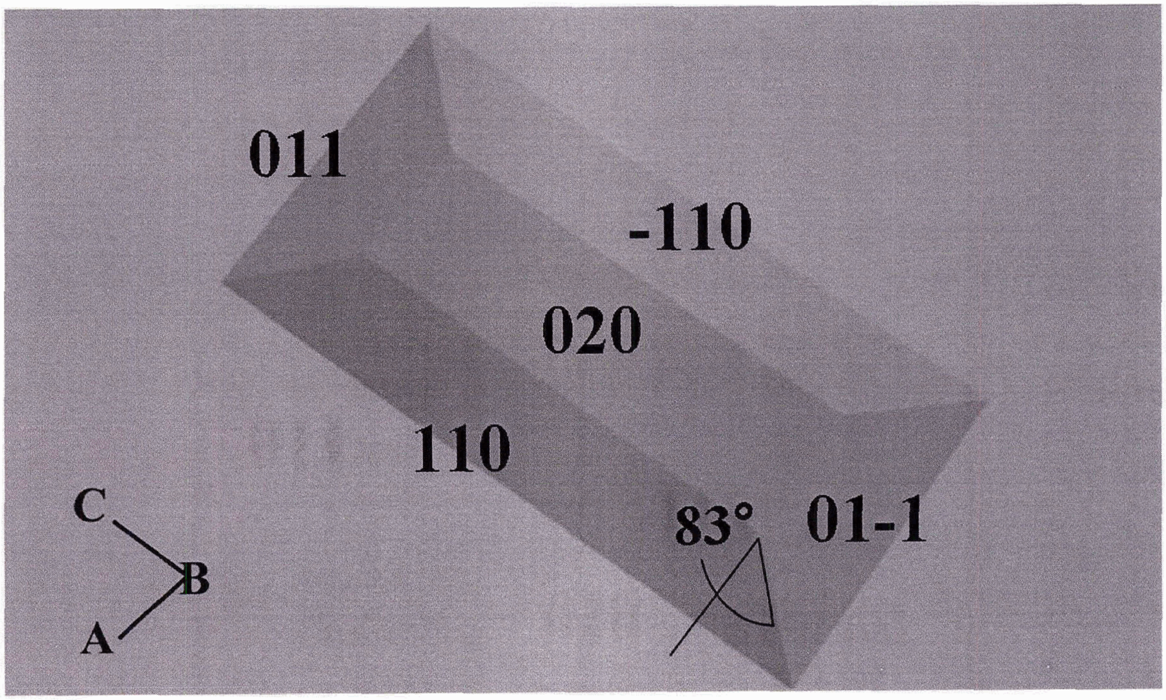

Figure 4-23 - Depiction of Class E crystal from Figure 4-22.

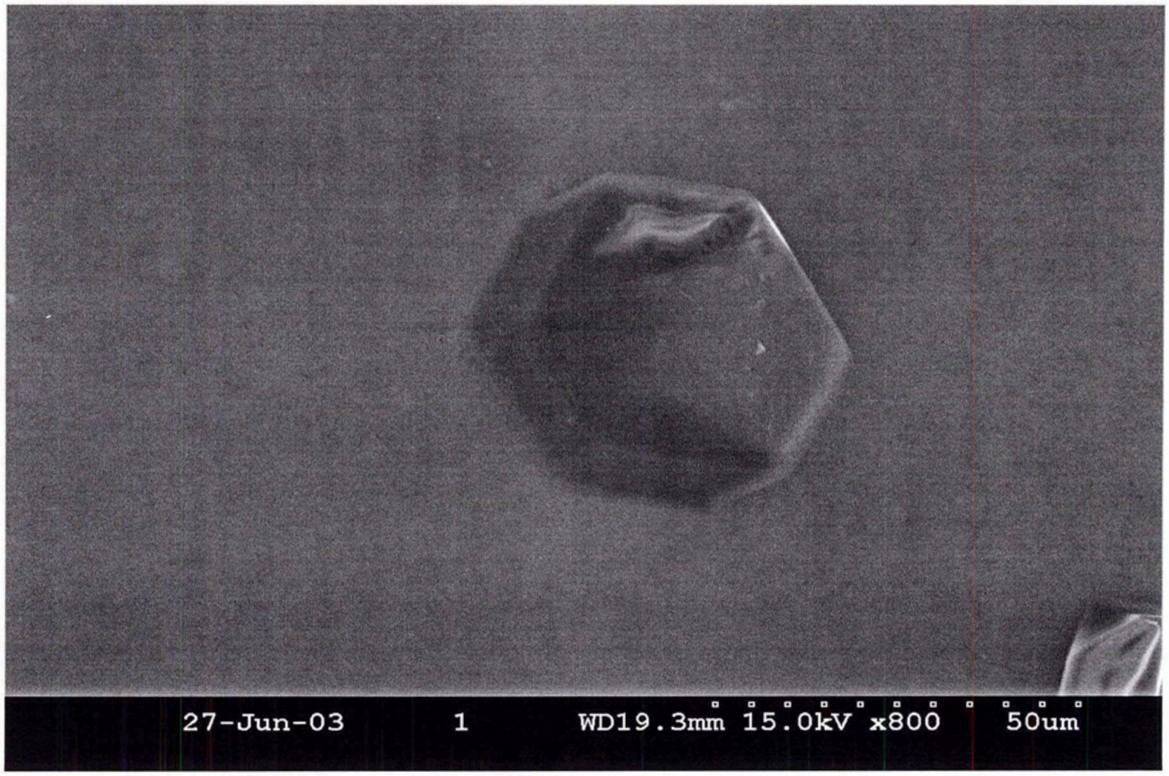

Figure 4-24 - Class D representative DL-diammonium tartrate crystal from DL-cysteine monolayer.

The second form of crystal identified within this set of data was classified as Class D and a representative of this is seen in Figure 4-24. Because these crystals appear to be growing on a "tilted" axis which is not completely perpendicular and parallel to the surface, angular data was not measured from the SEM images. The faces and general shape were reproduced using the growth rate ratios in Table 4-5 and a depiction of this can be seen in Figure 4-25.

Table 4-5 - Ratio of growth rates used in Shape® software to simulate Class D DL-diammonium tartrate crystal on DL-cysteine monolayer.

Crystal Form	Growth Rate Ratio
(01-1)	1
(020)	1.1
(02-1)	3.5
(100)	0.5
(00-2)	8.1
(03-1)	8.6
(110)	9.1
(01-2)	9.1

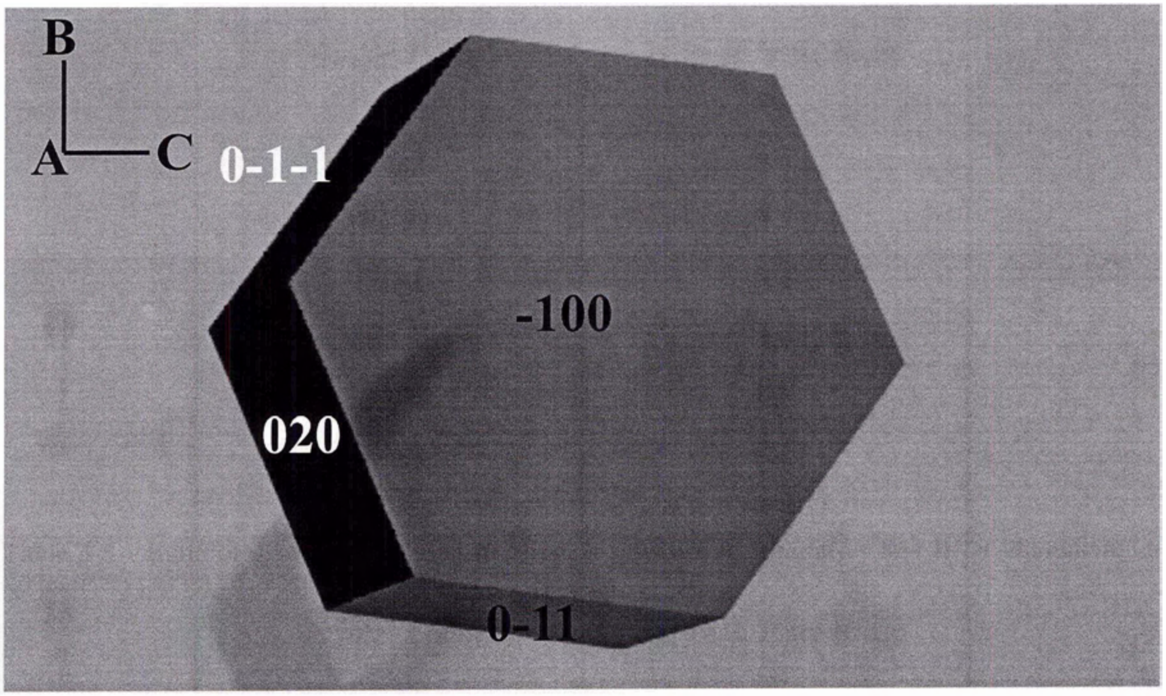

Figure 4-25 - Depiction of Class E crystal from Figure 4-24.

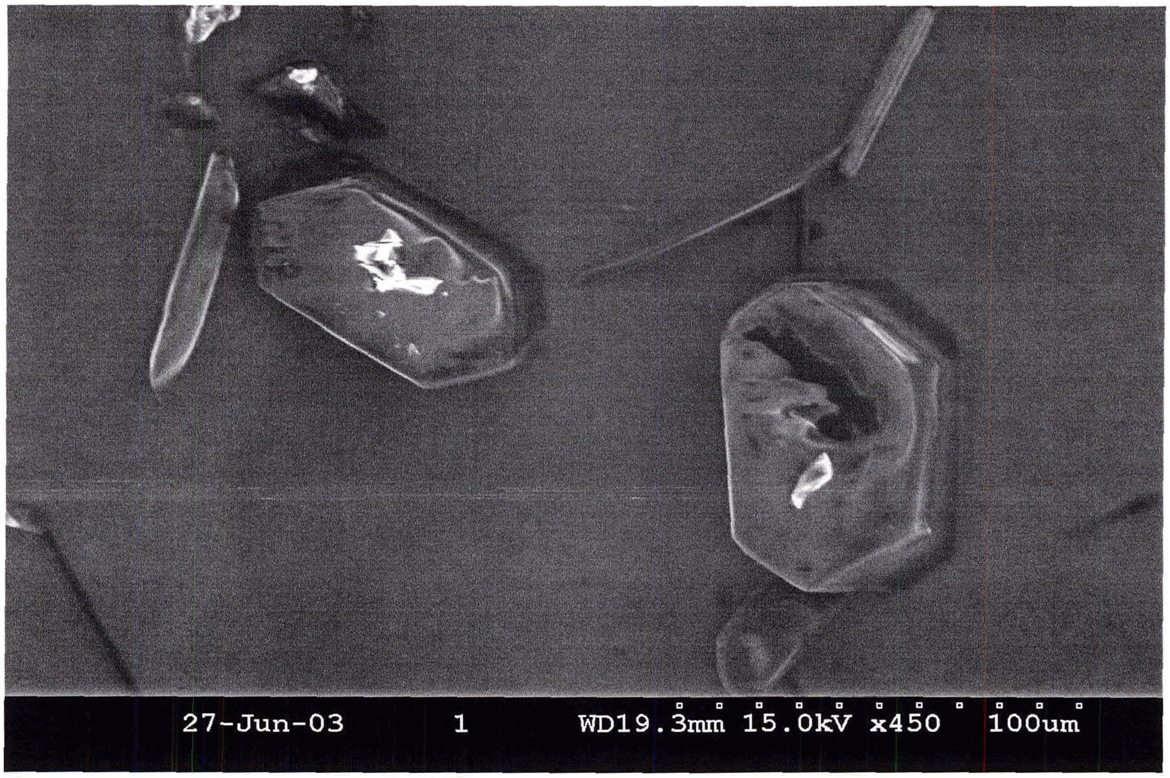

Figure 4-26 - Class C representatives of DL-diammonium tartrate crystal from DL-cysteine monolayer.

Two crystals falling under the Class C categorization can be seen in Figure 4-26. The "tilted" axis once again impeded the measurement of angular data. The shape of crystal class was replicated in Shape®, as seen in Figure 4-27, using the DL-diammonium tartrate properties and the growth rate ratios of Table 4-6.

Table 4-6 - Ratio of growth rates used in Shape® software to simulate Class C DL-diammonium tartrate crystal on DL-cysteine monolayer.

Crystal Form	Growth Rate Ratio
(01-1)	1
(020)	0.5
(02-1)	3.5
(100)	0.5
(00-2)	8.1
(03-1)	8.6
(110)	9.1
(01-2)	9.1

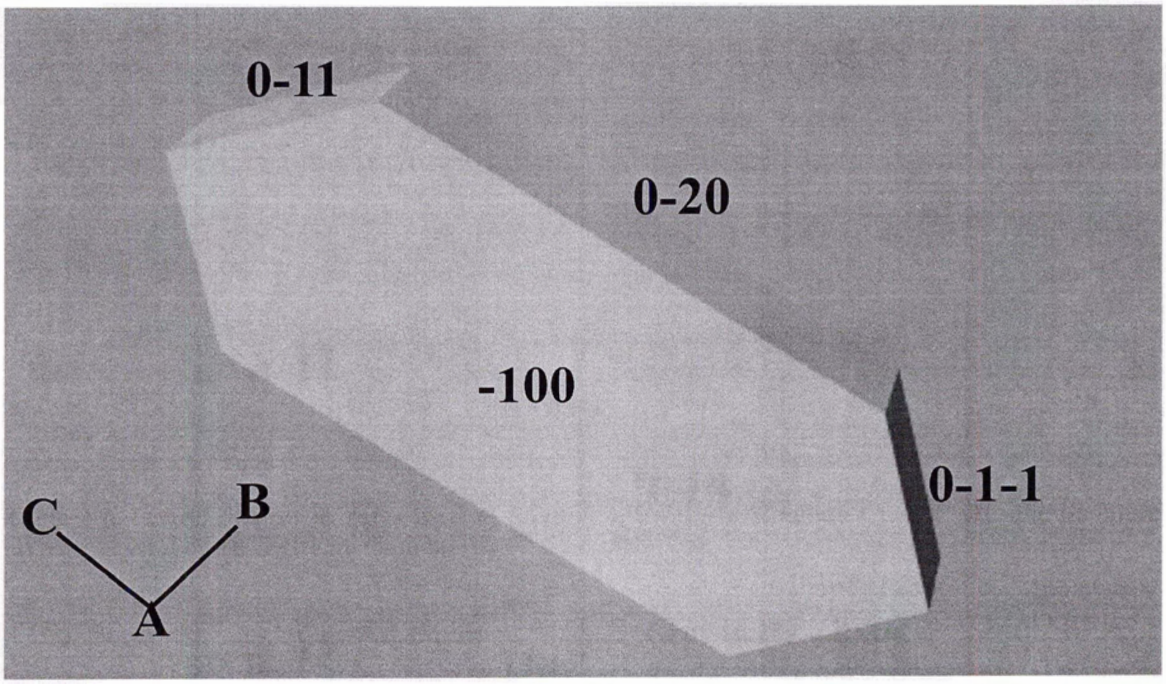

Figure 4-27 - Depiction of Class C crystal from Figure 4-26.

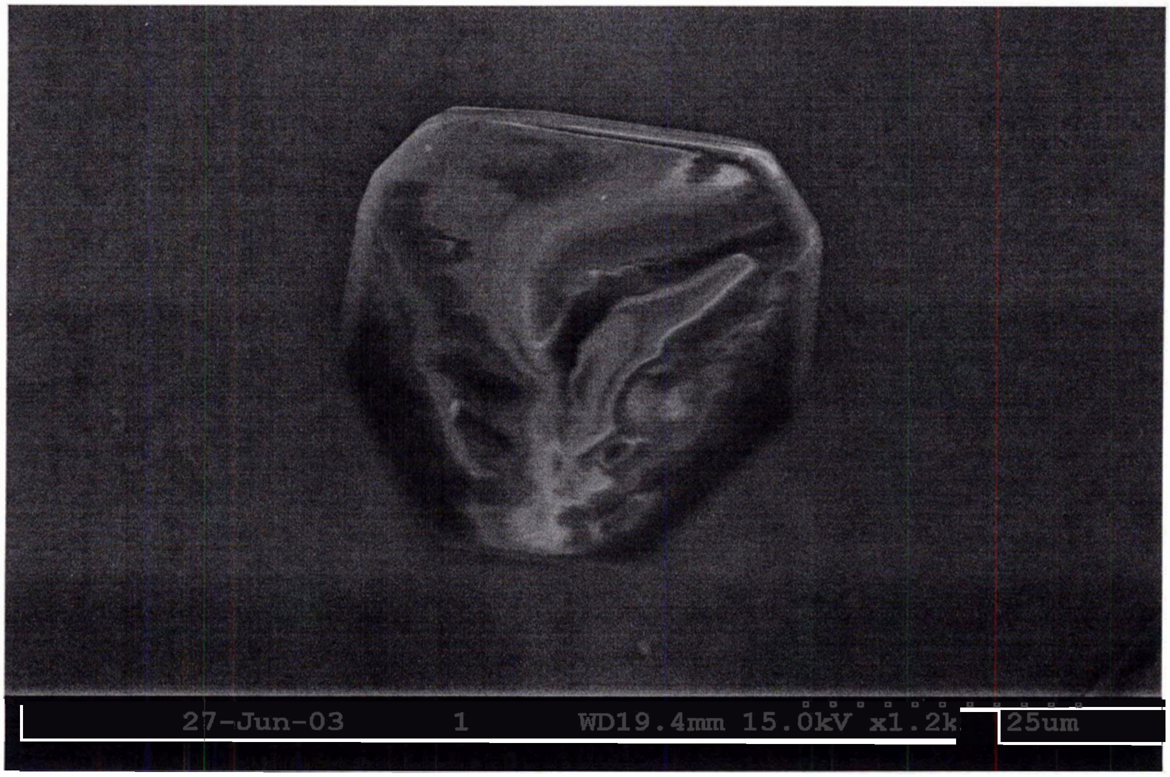

Figure 4-28 - Class A representative of DL-diammonium tartrate crystal from DL-cysteine monolayer

The final identifiable crystal type of this system can be seen in Figure 4-28. To find crystals of this nature for this system is most unusual because of the skewed hexagonal nature of the recognizable face, categorizing them as Class A. No combinations of growth rate ratios tested could reproduce this crystal from the DL-diammonium data provided by the CCDC. This shape of face is more typical of a (110) face from a D or L-diammonium tartrate crystal. These results suggest that some small amount of separation of enantiomers may occured at the monolayer.

Statistical data, SEM and crystal modeling indicate two faces ((020) - Figure 4-23 and (100) - Figure 4-25 and Figure 4-27) of interaction between the DL-diammonium tartrate crystal and the DL-cysteine monolayer. The length of the *a* cell edge of the DL-diammonium tartrate unit cell is 4.855Å. The *b* cell length is 16.326 Å and *c* cell length is 9.696 Å.

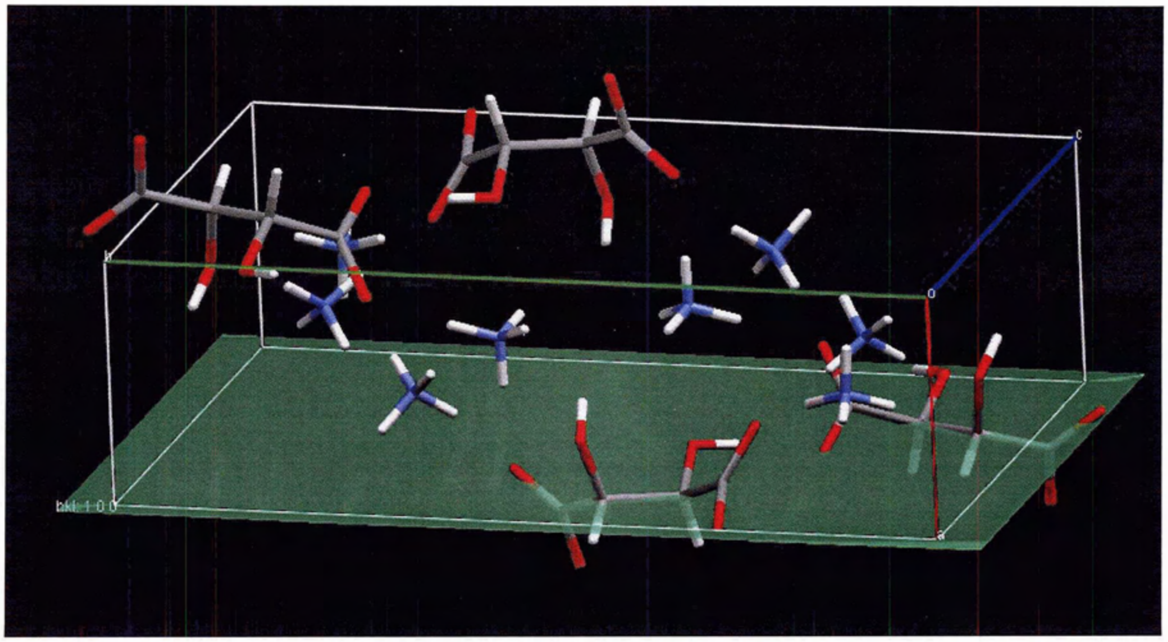

Figure 4-29 - DL-diammonium tartrate unit cell. (100) plane is highlighted in green.

With a sulfur headgroup spacing of 5 Å and the spacing of the headgroups being staggered due to the Au(111) nature of the substrate, five or six cysteine molecules on the surface with a bilayer conformation could theoretically interact with the (100) face of the DL-diammonium tartrate (shown in green in Figure 4-29) unit cell. Analysis of the unit cell reveals that although five or six cysteine molecules are theoretically most likely due to a monolayer arrangement, four cysteine units would be more involved in the hydrogen bonding with the tartrate. Five cysteine moieties could interact with the (100) plane, with the general location of chain indicated by Figure 4-30. Because the *a* cell edge of the unit cell measures 4.855 Å, hydrogen bonding is possible from the SAM to most of the entities contained in the cell. Each of the interactions will occur between the deprotonated cysteine carboxylate (HBA) / protonated ammonium group (HBD) and tartrate backbone carboxylate (HBA) / protonated cysteine amino group (HBD).

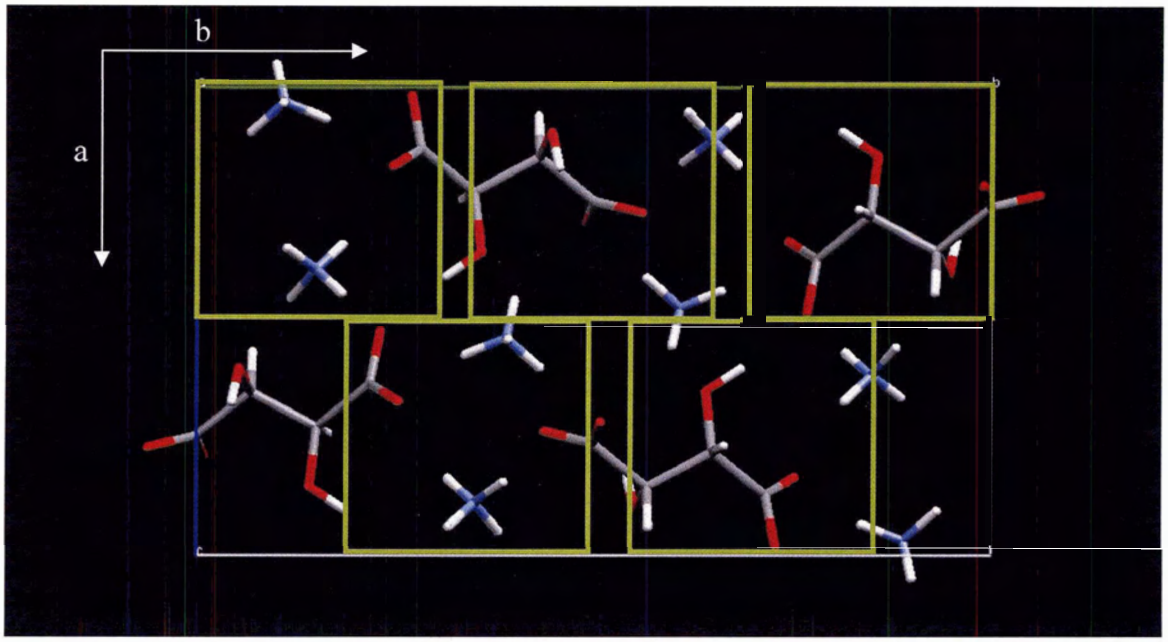

Figure 4-30 - DL-diammonium tartrate unit cell. Possible cysteine interaction locations are highlighted in yellow.

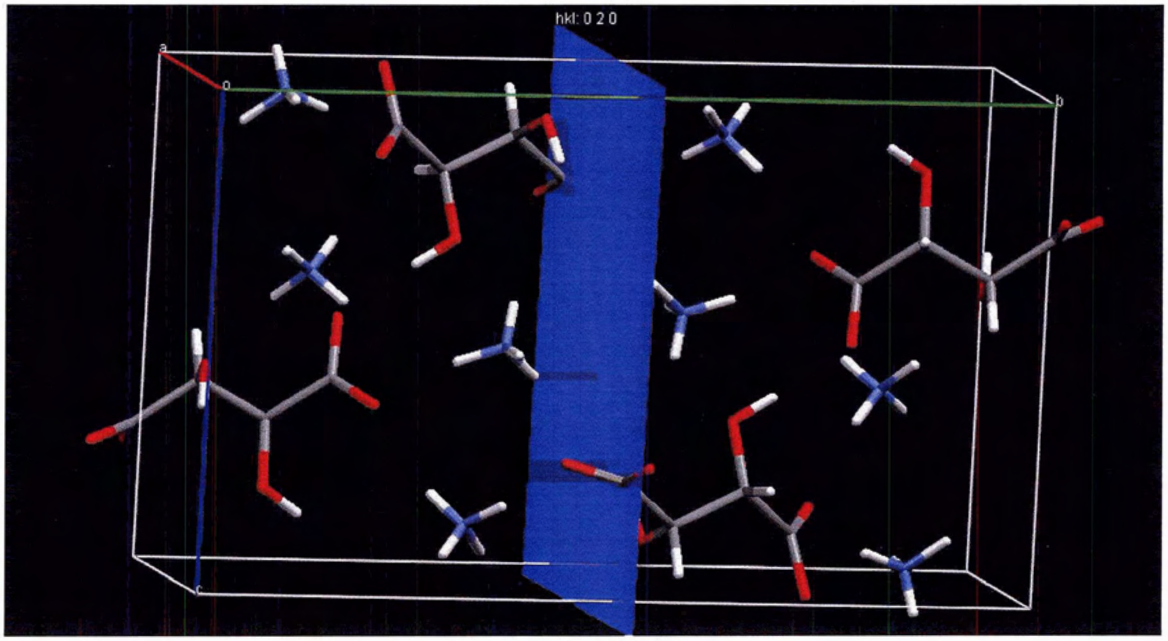

Figure 4-31 - DL-diammonium tartrate unit cell. (020) plane is highlighted in blue.

Another prospective interaction face indicated by SEM and crystal shape modeling for the DL-diammonium tartrate occurs along the (020) plane, as seen in Figure 4-31. In this situation, there are only two cysteine surface molecules that could potentially interact with the DL-diammonium tartrate without steric interference. Further analysis of the molecular arrangement within the unit cell shows that there will only be enough hydrogen acceptors in the DL-diammonium tartrate to interact with one cysteine molecule. Due to the dimensional constraints of the unit cell, there are no arrangements for the DL-diammonium tartrate that would provide an attractive enough interface along the (020) plane to allow for continuous crystallization along a bilayer of adsorbed cysteine molecules. Ultimately, a positive favorable interaction at the (020) plane is unlikely.

The conjectured disagreement between the arrangement of cysteine chains on the substrate and the best theoretical match for hydrogen bonding between the crystallizing substance and the SAM provide reasons for: (1) the large amount of crystals that formed but were misshapen and unidentifiable and (2) the high quantity but small average size of crystals in this system. Accounts from earlier work[133] show that the epitaxial match of the supramolecular system, in particular hydrogen bonding, is of utmost importance to crystallization at a monolayer surface.

There is prior evidence that racemic ammonium tartrates can crystallize from solution with the resultant crystal composition being of one or the other pure enantiomer[134]. If this is indeed the case for this doubly racemic system, then the evidence presented in the previous two systems studied in this thesis would indicate that a homomeric interaction would be most likely. A homomeric interaction for this system not only satisfies favorable supramolecular interactions but provides logic for the pentagonal shaped faces seen in Figure 4-28. If the representative crystal in Figure 4-28 is either pure D or L-diammonium tartrate, the pentagonal face could be identified as the (110) face. Further confirmation for this argument is supplied by the theoretical modeling, as no five sided faces could be produced by varying the DL-diammonium tartrate face growth rates.

The argument as to whether the pure enantiomers crystallized from the racemic solution and whether there is any preference for either a homomeric or heteromeric match between monolayer and diammonium tartrate is further investigated with the next system. In the next system, a racemic solution of diammonium tartrate will be paired with an L-cysteine monolayer.

4.5 DL-Diammonium Tartrate on L-Cysteine

The crystals analyzed in this system were, in the most part, either nicely formed Class E crystals or were indistinguishable. As seen in Figure 4-32, of the 1054 crystals in this statistical population, 505 were classified as Class E and 512 were classified as indistinguishable. These results can be loosely interpreted in the following manner: one enantiomer of the DL-diammonium tartrate interacted favorably with the monolayer, forming well defined crystals, while the opposite enantiomer and the racemate formed misshapen crystals due to a lack of positive interaction with the SAM.

The size histogram for this system tends toward a skewed Gaussian distribution. The majority of the crystals lie in the 100 – 110 μm bin with the average size of the crystals being 140 ± 72 μm, which appears to be in agreement with the average for most of the other tartrate/monolayer systems.

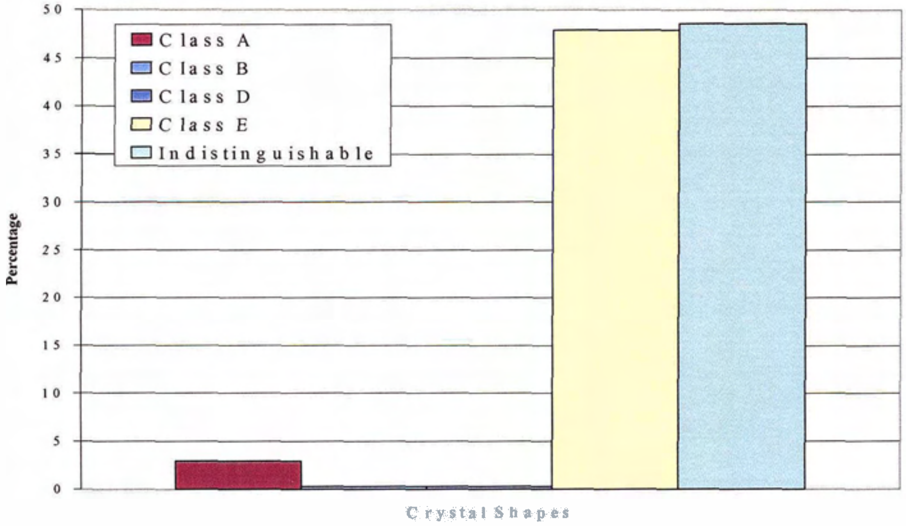

Figure 4-32 - Percentage distribution of shapes for DL-Diammonium tartrate crystals on L-cysteine monolayers

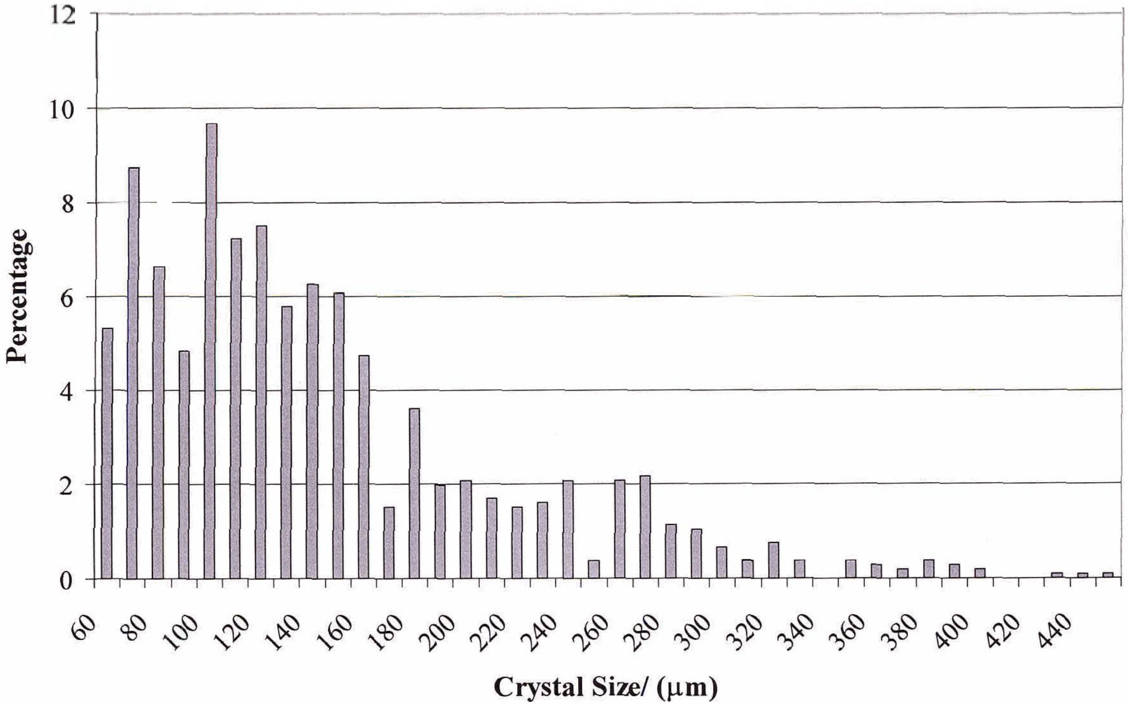

Figure 4-33 - Size percentage distribution of DL-Diammonium tartrate crystals on L-cysteine monolayers

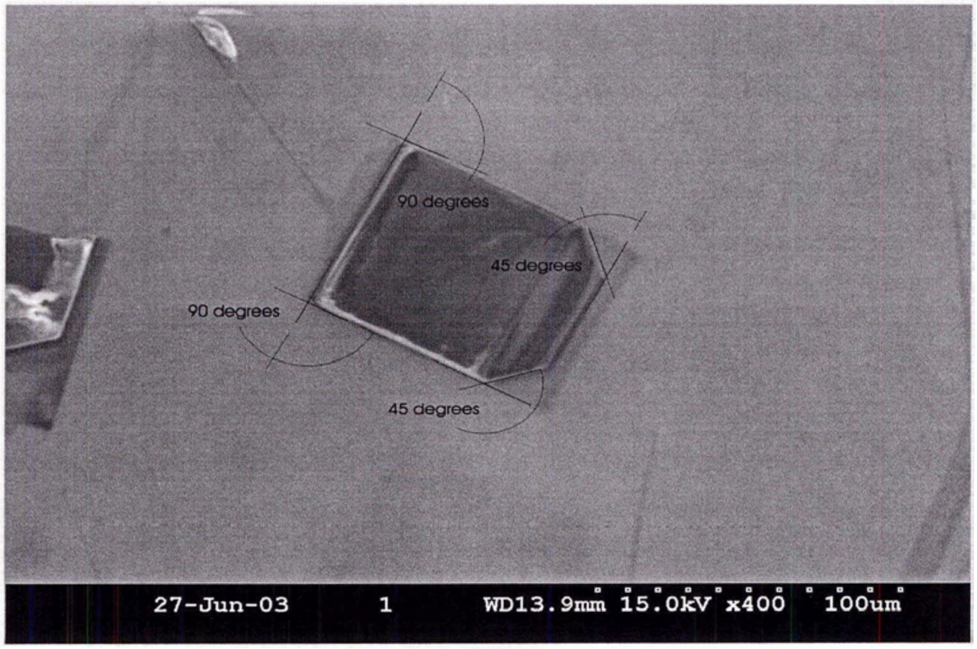

Figure 4-34 - Class E representatives of DL-diammonium tartrate crystal from L-cysteine monolayer.

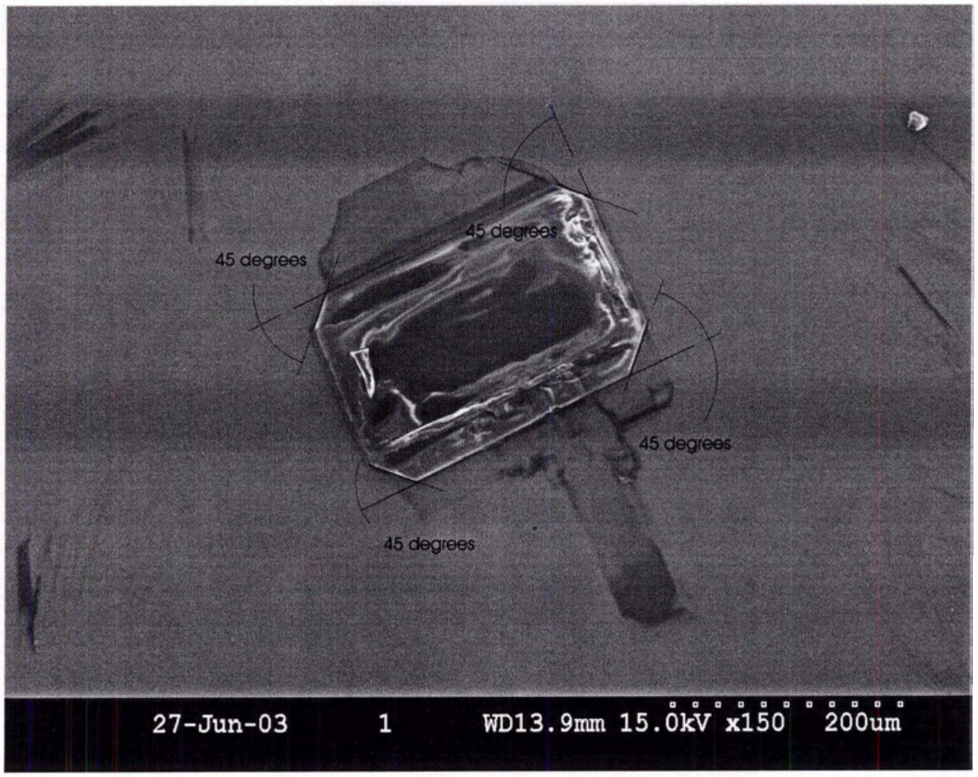

Figure 4-35 - Class E representatives of DL-diammonium tartrate crystal from L-cysteine monolayer.

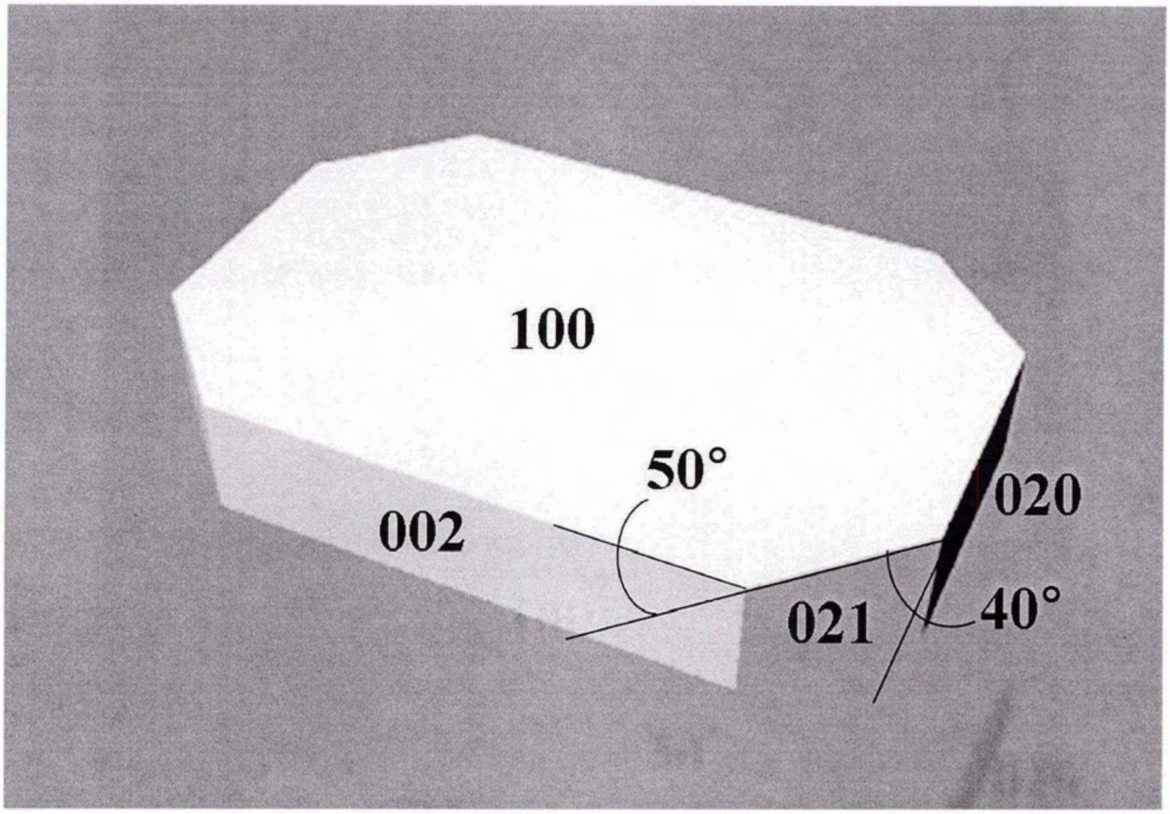

Figure 4-36 - Depiction of DL-diammonium tartrate crystals in Figure 4-34 and Figure 4-35

Figure 4-34 is an SEM image of a crystal from this system which has two blunted ends and Figure 4-35 depicts a crystal with four blunted corners. Figure 4-36 is the corresponding characterization of the crystals produced in Shape® by manipulating the crystal properties (CCDC REFCODE: ZZZJII01[132]) and growth rate ratios, as seen in Table 4-7. Although solutions of racemic mixtures have been shown to have the ability to crystallize the enantiomers separately, crystal modeling was carried out using the parameters of DL-cysteine, as that was the original solute used in this crystallization system. However, the shape could also be produced using the crystal parameters for the pure enantiomer (for instance, see Figure 4-16).

Table 4-7 - Ratio of growth rates used in Shape® software to simulate Class E DL-diammonium tartrate crystal on L-cysteine monolayer.

Crystal Form	Growth Rate Ratio
(01-1)	5
(020)	3.5
(02-1)	3.5
(100)	1
(00-2)	2
(03-1)	8.6
(110)	9.1
(01-2)	9.1

The XPD spectra for diammonium tartrate obtained from different conditions are presented in Figure 4-37. For both the crystals from solution and the synthesized DL-diammonium tartrate there are predominant peaks in the highlighted areas of Figure 4-37. On the other hand, the spectrum for the crystals that came from the L-cysteine monolayer shows a completely different pattern than the ones observed for the crystals from both solution and synthesis. It is apparent that the crystal structure for the diammonium salt obtained from the monolayer is different than the others in Figure 4-37. In fact, an analysis of the angular position of the peaks for the diammonium tartrate crystals from the L-cysteine monolayer (Figure 4-37) shows similarities to the XPD of the crystal from the homomeric systems.

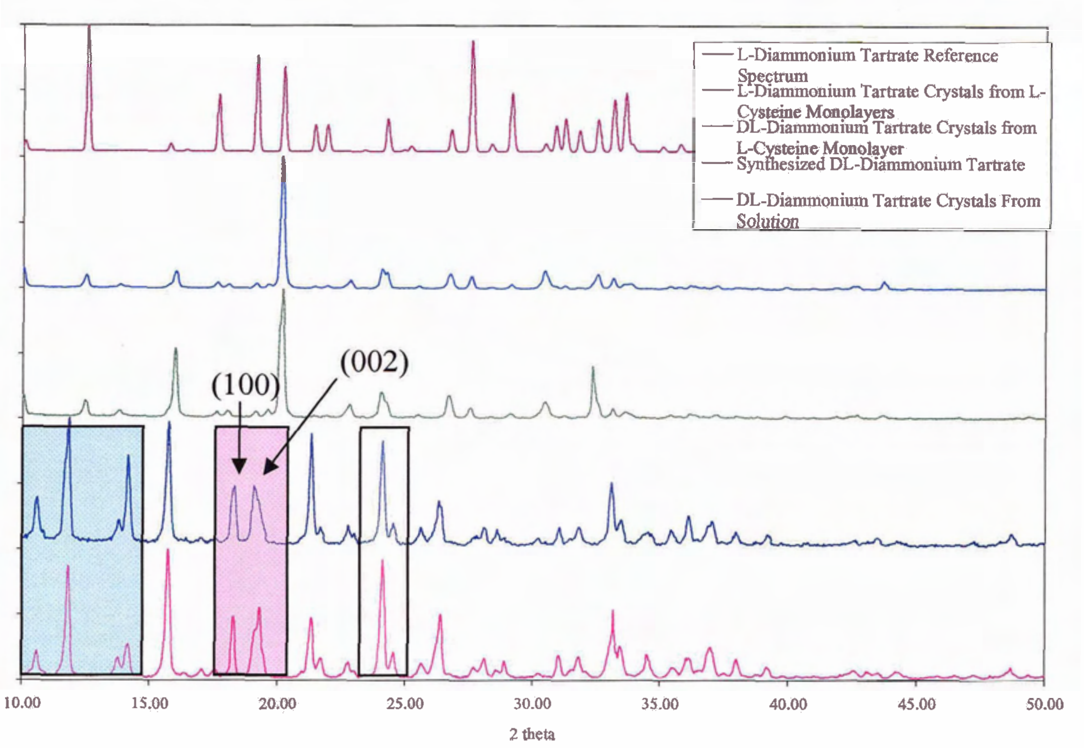

Figure 4-37 - Comparison XPD Spectra of DL-diammonium tartrate from three stages of experimental work. The reference XPD spectrum for L-diammonium tartrate and the XPD spectrum of L-diammonium tartrate crystals from L-cysteine monolayers are as well shown.

On the other hand a correlation between the (100) plane of the DL-diammonium tartrate crystal and the L-cysteine SAM can also be conceived, using a method similar to earlier reports[135]. The interfacial relationship between DL-diammonium tartrate and DL-cysteine has been discussed in the previous section.

Considering that the substituents on the chiral center of cysteine are all relatively small and that each chain of the monolayer can rotate in the cant direction (see section 2.1.2.3), does the change in the form of the monolayer from racemic to pure enantiomer solely justify the significant changes in the shape of the crystals? Previous accounts of selective heterogenous crystallization from homogenous solutions of calcium carbonate in the presence of an alkanethiol monolayer shows the strong influence of the monolayer on the crystal shape[136,137]. Additionally, polarimetry data for the crystals of this system resulted in a +0.018° rotation of the plane polarized light indicating that the L-cysteine SAM preferentially crystallizes the L-diammonium tartrate molecules from a DL-diammonium tartrate crystallizing solution. The homomeric enantioselectivity of the L-cysteine for the L-diammonium tartrate over the D-diammonium tartrate results from the increase in supramolecular bonding, which was discussed previously.

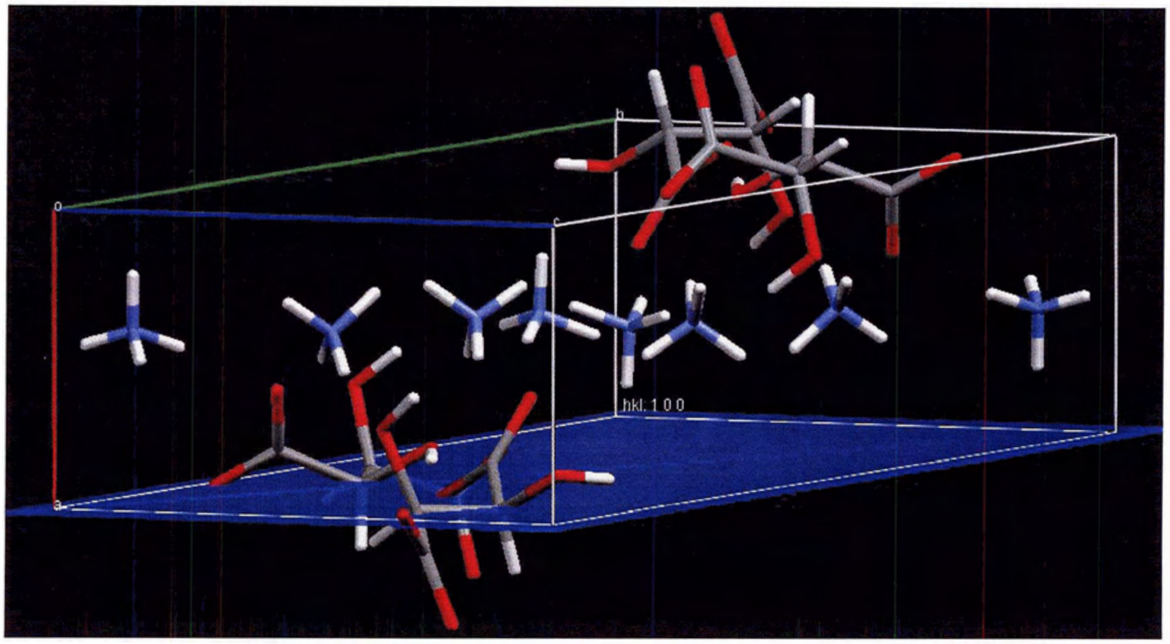

Figure 4-38 - Diagonal view of unit cell of DL-diammonium tartrate. (100) plane is shown in blue.

More arguments for the enantioselective crystallization can be drawn from an analysis of the unit cell of DL-diammonium tartrate, as shown in Figure 4-38. When examining the likely interactions that a group of L-cysteine SAMs would have with the (100) plane of a DL-diammonium tartrate unit cell (most likely nucleation plane, as shown in Figure 4-36), most of the same problems discussed for the DL-cysteine monolayer in section 4.4 are present. The (100) plane bisects the tartrate backbones in the unit cell, as seen by the highlighted plane in Figure 4-38, bringing into question whether the SAM can interact with this plane at all due to the conflict between the preferential H-bonding distance and steric requirements to bond to the HBAs. Due to the intermolecular hydrogen bonding participation (seen in Figure 4-39) of the hydroxyl groups of the tartrate backbone within the crystal, a likely scenario has the deprotonated carboxyl groups of L-cysteine bonding to the ammonium groups in the crystal because of the increased likelihood of an 180° hydrogen-bond forming.

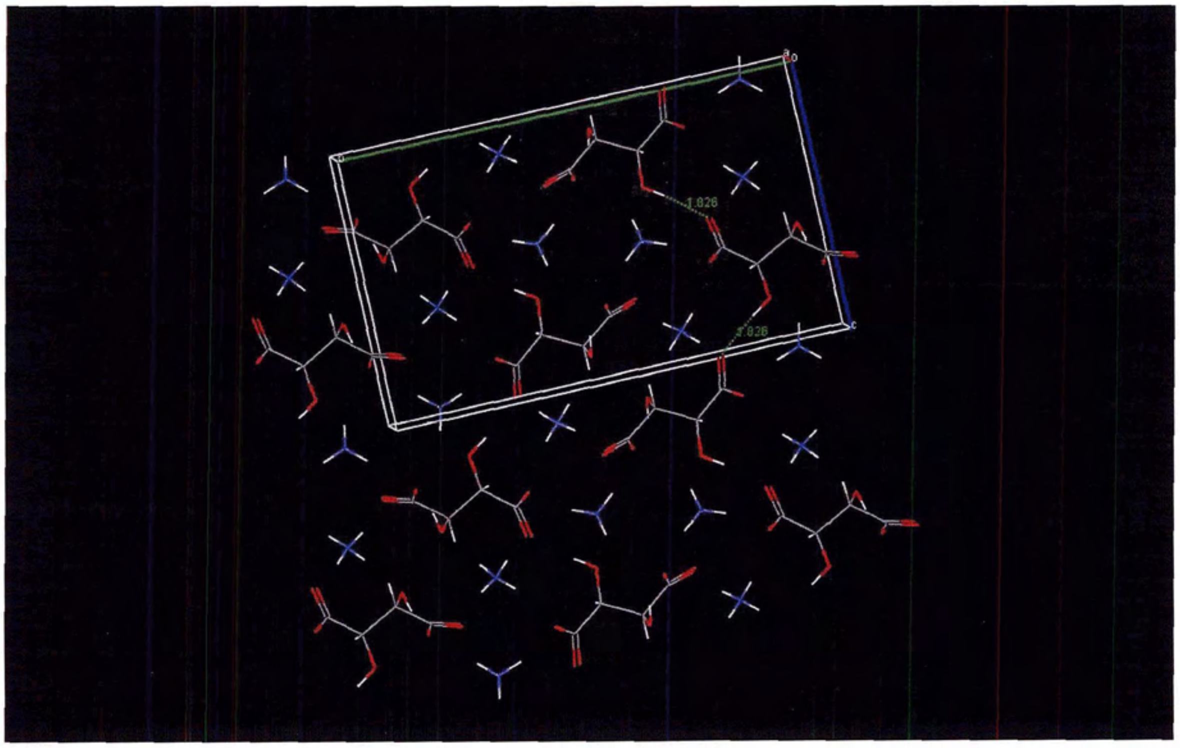

Figure 4-39 - Extended view of the (100) plane for DL-diammonium tartrate

Since the DL-diammonium tartrate will nucleate and tend towards the lowest energy possible in its growth, theoretically it seems more than reasonable that the racemic mixture would separate into its enantiomers for crystal nucleation and growth if energetically favorable[138]. The XPD spectrum in Figure 4-37 for the crystals grown on the L-cysteine monolayer shows a significant change when compared to solution and synthesized DL-diammonium tartrate. The possibility for interaction at the (100) plane of the DL-diammonium tartrate unit cell with the monolayer, causing changes in growth direction and crystal shape, cannot be discarded, since a significant amount of crystals are indistinguishable. The other scenario, which consists of enantioselective crystallization at the L-cysteine interface, is however more likely. The growth in this case would result in crystals shaped similar to that of Figure 4-16 and crystal growth from the (001) face with the L or D-diammonium tartrate unit cell properties. Polarimetry supports this conclusion since the observed rotation of the plane polarized light indicates a chiral solution in favor of the L enantiomer. Previous accounts of racemic solutions crystallizing enantioselectively towards one enantiomer have been published elsewhere[93].

5 Summary, Conclusions and Future Work

Table 5-1 - Comparison between all the systems investigated in this work

	Statistical Survey							
Tartrate / Crystal System	Population Size	Average Size (μm)	Density (crystals/μm^2)	Shape			Interactive Plane	Specific Rotation [α] (°)
				Major Class	Percentage (%)	Average Size (μm)		
L-diammonium tartrate on L-cysteine	1024	83 ± 32	1.09 x 10^{-2}	Class F	78.03	83 ± 33	(001)	+0.201
D-diammonium tartrate on L-cysteine	114	344 ± 288	1.22 x 10^{-3}	Class E	54.39	288 ± 164	(001)	-0.048
DL-diammonium tartrate on DL-cysteine	1187	101 ± 42	2.54 x 10^{-3}	Indistinguishable	78.61	100 ± 41	(020) (-100)	-
DL-diammonium tartrate on L-cysteine	1054	140 ± 72	2.25 x 10^{-3}	Indistinguishable Class E	48.58	129 ± 59	(100)	+0.018

The results of the overall statistical survey are summarized in Table 5-1. By using the XPD data, crystals were simulated to match the SEM and optical images. The simulated crystals gave an indication as to the interaction face(s) between the diammonium tartrate and the cysteine monolayers. Using the indicated faces, theoretical supramolecular models of the specific interactions that occur between the molecules of the diammonium tartrate and those of the cysteine were conceived.

Evidence for the effect of the L-cysteine monolayer on the crystallization of L-diammonium tartrate was provided. The general shape of the crystals varies from that of previously observed L-diammonium tartrate crystals, which appear needlelike when grown from solution. This change in crystal shape for L-diammonium tartrate on L-cysteine monolayers was probed not only by SEM imaging, but by the crystal shape classification in the statistical survey.

It was concluded that L-diammonium tartrate was enantioselectively crystallized from a racemic solution onto L-cysteine monolayers when all the individual sets of data were examined collectively. The statistical survey pointed to a distinct crystal shape for the DL-diammonium tartrate on L-cysteine and indicated that almost half the crystals grew in that fashion. This distinctive crystal shape from the DL-diammonium tartrate crystals on L-cysteine monolayers resembled the crystal shape of the L-diammonium tartrate on L-cysteine monolayers more than the shape of the crystals from the DL-diammonium tartrate on DL-cysteine monolayers. The XPD spectrum for the DL-diammonium tartrate from L-cysteine monolayers was compared to the racemic and L enantiomer crystals from monolayer spectra. The results indicated the presence of L-diammonium tartrate crystal growth from a DL-diammonium tartrate solution when crystallized onto a L-cysteine monolayer. This outcome is reasonable due to the favourable interaction proposed for the L-diammonium tartrate on L-cysteine monolayer system.

As a final measure, polarimetry was conducted on the sample of crystals scraped from the DL-diammonium tartrate on L-cysteine monolayered slides. The positive rotation of the polarized light coincided with previous polarimetry results and provided the final evidence needed to conclude that the L-diammonium tartrate had indeed been enantioselectively crystallized from a DL-diammonium tartrate solution.

Possible future work in this particular research would be primarily focused on crystallization of the various diammonium tartrates on SAMs of D-cysteine. This would provide insight as the crystallization habits on such monolayers. As well, experiments on DL-diammonium tartrate on D-cysteine should conclude whether the monolayer has the capability to crystallize enantioselectively from a racemic solution by producing mirror image crystals of those formed in this research.

6 References

1. A. T. Borchers, P. A. Davis, and M. E. Gershwin, *Experimental Biology and Medicine*, *229*, 21 (2004).
2. Y. Chen, W. Q. Wang, and C. Yu, *Acta Physico-Chimica Sinica*, *20*, 540 (2004).
3. R. M. Hazen and D. S. Sholl, *Nature Materials*, *2*, 367 (2003).
4. J. F. Kang, S. Liao, R. Jordan, and A. Ulman, *Journal of the American Chemical Society*, *120*, 9662 (1998).
5. G. Horneck and C. Baumstark-Khan, *Astrobiology : the quest for the conditions of life*, Springer, Berlin ; New York, 2002.
6. R. N. Orth, T. G. Clark, and H. G. Craighead, *Biomedical Microdevices*, *5*, 29 (2003).
7. M. Watanabe and K. Kajikawa, *Sensors and Actuators B-Chemical*, *89*, 126 (2003).

8. X. Y. Zhu, *Acta Physico-Chimica Sinica*, *18*, 855 (2002).

9. N. K. Chaki and K. Vijayamohanan, *Biosensors & Bioelectronics*, *17*, 1 (2002).

10. T. Wink, S. J. vanZuilen, A. Bult, and W. P. vanBennekom, *Analyst*, *122*, R43 (1997).

11. S. Sampath and O. Lev, *Advanced Materials*, *9*, 410 (1997).

12. P. E. Laibinis and G. M. Whitesides, *Journal of the American Chemical Society*, *114*, 1990 (1992).

13. E. M. Arnett, N. G. Harvey, and P. L. Rose, *Accounts of Chemical Research*, *22*, 131 (1989).

14. R. A. Meyers, *Encyclopedia of analytical chemistry : applications, theory and instrumentation*, Wiley, Chichester, West Sussex, UK ; New York, 2000.

15. A. Ulman, *Chemical Reviews*, *96*, 1533 (1996).

16. I. Willner, A. Riklin, B. Shoham, D. Rivenzon, and E. Katz, *Advanced Materials*, *5*, 912 (1993).

17. H. G. Hong, W. Park, and E. Yu, *Journal of Electroanalytical Chemistry*, *476*, 177 (1999).

18. S. F. Wang and D. Du, *Sensors and Actuators B-Chemical*, *94*, 282 (2003).

19. B. Kazakeviciene, G. Valincius, G. Niaura, Z. Talaikyte, M. Kazemekaite, and V. Razumas, *Journal of Physical Chemistry B*, *107*, 6661 (2003).

20. Z. Dai and H. X. Ju, *Physical Chemistry Chemical Physics*, *3*, 3769 (2001).

21. G. K. Jennings and P. E. Laibinis, *Colloids and Surfaces a-Physicochemical and Engineering Aspects*, *116*, 105 (1996).

22. G. K. Jennings, J. C. Munro, T. H. Yong, and P. E. Laibinis, *Langmuir*, *14*, 6130 (1998).

23. F. P. Zamborini and R. M. Crooks, *Langmuir*, *14*, 3279 (1998).

24. B. A. Mantooth and P. S. Weiss, *Proceedings of the Ieee*, *91*, 1785 (2003).

25. J. J. Gooding, F. Mearns, W. R. Yang, and J. Q. Liu, *Electroanalysis*, *15*, 81 (2003).

26. S. Y. Lee, J. G. Kim, W. S. Shin, H. J. Lee, S. Y. Koo, and H. W. Lee, *Materials Science & Engineering C-Biomimetic and Supramolecular Systems*, *24*, 3 (2004).

27. R. I. Masel, *Priniciples of Adsorption and Reaction on Solid Surfaces*, Wiley, Toronto, 1996.

28. F. Schreiber, *Progress in Surface Science*, *65*, 151 (2000).

29. M. D. Porter, T. B. Bright, D. L. Allara, and C. E. D. Chidsey, *Journal of the American Chemical Society*, *109*, 3559 (1987).

30. C. E. D. Chidsey and D. N. Loiacono, *Langmuir*, *6*, 682 (1990).

31. C. E. D. Chidsey, G. Y. Liu, P. Rowntree, and G. Scoles, *Journal of Chemical Physics*, *91*, 4421 (1989).

32. Y. T. Kim and A. J. Bard, *Langmuir*, *8*, 1096 (1992).

33. A. S. Dakkouri, D. M. Kolb, R. EdelsteinShima, and D. Mandler, *Langmuir*, *12*, 2849 (1996).

34. T. Ichii, T. Fukuma, K. Kobayashi, H. Yamada, and K. Matsushige, *Applied Surface Science*, *210*, 99 (2003).

35. M. C. Leopold, J. A. Black, and E. F. Bowden, *Langmuir*, *18*, 978 (2002).

36. M. C. Bourg, A. Badia, and R. B. Lennox, *Journal of Physical Chemistry B*, *104*, 6562 (2000).

37. J. I. Siepmann and I. R. Mcdonald, *Langmuir*, *9*, 2351 (1993).

38. G. Nelles, H. Schonherr, M. Jaschke, H. Wolf, M. Schaub, J. Kuther, W. Tremel, E. Bamberg, H. Ringsdorf, and H. J. Butt, *Langmuir*, *14*, 808 (1998).

39. C. Schonenberger, J. A. M. Sondaghuethorst, J. Jorritsma, and L. G. J. Fokkink, *Langmuir*, *10*, 611 (1994).

40. C. A. Widrig, C. Chung, and M. D. Porter, *Journal of Electroanalytical Chemistry*, *310*, 335 (1991).

41. E. Sabatani, I. Rubinstein, R. Maoz, and J. Sagiv, *Journal of Electroanalytical Chemistry*, *219*, 365 (1987).

42. C. Schonenberger, J. Jorritsma, J. A. M. Sondaghuethorst, and L. G. J. Fokkink, *Journal of Physical Chemistry*, *99*, 3259 (1995).

43. S. C. Chang, I. Chao, and Y. T. Tao, *Journal of the American Chemical Society*, *116*, 6792 (1994).

44. D. F. Yang, C. P. Wilde, and M. Morin, *Langmuir*, *12*, 6570 (1996).

45. M. Jaschke, H. Schonherr, H. Wolf, H. J. Butt, E. Bamberg, M. K. Besocke, and H. Ringsdorf, *Journal of Physical Chemistry*, *100*, 2290 (1996).

46. J. Noh and M. Hara, *Langmuir*, *18*, 1953 (2002).

47. L. L. Duan and S. J. Garrett, *Langmuir*, *17*, 2986 (2001).

48. K. Aoki and T. Kakiuchi, *Journal of Electroanalytical Chemistry*, *478*, 101 (1999).

49. L. S. Jung and C. T. Campbell, *Journal of Physical Chemistry B*, *104*, 11168 (2000).

50. P. Fenter, P. Eisenberger, and K. S. Liang, *Physical Review Letters*, *70*, 2447 (1993).

51. D. E. Weisshaar, M. M. Walczak, and M. D. Porter, *Langmuir*, *9*, 323 (1993).

52. Y. Kim, K. S. Kim, M. Park, and J. Jeong, *Thin Solid Films*, *341*, 91 (1999).

53. I. Engquist, M. Lestelius, and B. Liedberg, *Langmuir*, *13*, 4003 (1997).

54. T. Sawaguchi, Y. Sato, and F. Mizutani, *Journal of Electroanalytical Chemistry*, *507*, 256 (2001).

55. K. V. G. K. Murty, M. Venkataramanan, and T. Pradeep, *Langmuir*, *14*, 5446 (1998).

56. K. Uvdal, P. Bodo, and B. Liedberg, *Journal of Colloid and Interface Science*, *149*, 162 (1992).

57. A. Ihs and B. Liedberg, *Journal of Colloid and Interface Science*, *144*, 282 (1991).

58. J. D. Zhang, Q. J. Chi, J. U. Nielsen, E. P. Friis, J. E. T. Andersen, and J. Ulstrup, *Langmuir*, *16*, 7229 (2000).

59. Q. M. Xu, L. J. Wan, C. Wang, C. L. Bai, Z. Y. Wang, and T. Nozawa, *Langmuir*, *17*, 6203 (2001).

60. N. Camillone, C. E. D. Chidsey, G. Liu, and G. Scoles, *Journal of Chemical Physics*, *98*, 4234 (1993).

61. G. Dodero, L. De Michieli, O. Cavalleri, R. Rolandi, L. Oliveri, A. Dacca, and R. Parodi, *Colloids and Surfaces a-Physicochemical and Engineering Aspects*, *175*, 121 (2000).

62. J. P. Glusker, M. Lewis, and M. Rossi, *Crystal structure analysis for chemists and biologists*, Vch, N.Y., N.Y [i.e. New York, N.Y.], 1994.

63. J. W. Mullin, *Crystallization*, Butterworth-Heinemann, Oxford ; Boston, 2001.

64. A. G. Walton, *The Formation and Properties of Precipitates*, Vol. 23, Interscience, New York, 1967.

65. D. T. J. Hurle, *Handbook of crystal growth*, North-Holland, Amsterdam, 1993.

66. E. V. Khamski*i, *Crystallization from solutions*, Consultants Bureau, New York,, 1969.

67. I. F. Roberts, *Crystals and Their Structures*, Methuen, London, 1974.

68. S. H. Hurlburt, Klein, C., *Manual of Mineralogy*, John Wiley and Sons, New York, 1977.

69. P. W. Atkins, *Physical chemistry*, W.H. Freeman & Co., New York, 1994.

70. D. Perkins, *Mineralogy*, Simon and Schuster, Upper Saddle River, 1998.

71. P. W. Atkins, *Physical Chemistry*, W.H. Freeman and Company, New York, 1994.

72. D. D. Archibald, S. B. Qadri, and B. P. Gaber, *Langmuir*, *12*, 538 (1996).

73. L. M. Frostman, M. M. Bader, and M. D. Ward, *Langmuir*, *10*, 576 (1994).

74. S. J. Bonafede and M. D. Ward, *Journal of the American Chemical Society*, *117*, 7853 (1995).

75. A. Y. Lee, A. Ulman, and A. S. Myerson, *Langmuir*, *18*, 5886 (2002).

76. H. J. Himmel, C. Woll, R. Gerlach, G. Polanski, and H. G. Rubahn, *Langmuir*, *13*, 602 (1997).

77. L. M. Frostman and M. D. Ward, *Langmuir*, *13*, 330 (1997).

78. J. Aizenberg, A. J. Black, and G. H. Whitesides, *Journal of the American Chemical Society*, *121*, 4500 (1999).

79. S. J. Grabowski, *Journal of Physical Organic Chemistry*, *17*, 18 (2004).

80. G. R. Desiraju, *Accounts of Chemical Research*, *29*, 441 (1996).

81. J. F. Kang, J. Zaccaro, A. Ulman, and A. Myerson, *Langmuir*, *16*, 3791 (2000).

82. B. R. Heywood and S. Mann, *Advanced Materials*, *6*, 9 (1994).

83. L. Addadi, J. Moradian, E. Shay, N. G. Maroudas, and S. Weiner, *Proceedings of the National Academy of Sciences of the United States of America*, *84*, 2732 (1987).

84. L. Addadi and S. Weiner, *Proceedings of the National Academy of Sciences of the United States of America*, *82*, 4110 (1985).

85. S. Feng and T. Bein, *Science*, *265*, 1839 (1994).

86. A. Berman, D. J. Ahn, A. Lio, M. Salmeron, A. Reichert, and D. Charych, *Science*, *269*, 515 (1995).

87. I. A. Aksay, M. Trau, S. Manne, I. Honma, N. Yao, L. Zhou, P. Fenter, P. M. Eisenberger, and S. M. Gruner, *Science*, *273*, 892 (1996).

88. G. Z. Mao, L. Lobo, R. Scaringe, and M. D. Ward, *Chemistry of Materials*, *9*, 773 (1997).

89. L. Yu, S. M. Reutzel, and G. A. Stephenson, *Pharmaceutical Science & Technology Today*, *1*, 118 (1998).

90. K. Q. Yu, Z. S. Li, and J. Z. Sun, *Langmuir*, *18*, 1419 (2002).

91. M. Castonguay, J. R. Roy, A. Rochefort, and P. H. McBreen, *Journal of the American Chemical Society*, *122*, 518 (2000).

92. M. H. Engel and S. A. Macko, *Nature*, *389*, 265 (1997).

93. N. Banno, T. Nakanishi, M. Matsunaga, T. Asahi, and T. Osaka, *Journal of the American Chemical Society*, *126*, 428 (2004).

94. H. Eun and Y. Umezawa, *Analytica Chimica Acta*, *413*, 223 (2000).

95. R. Paolesse, D. Monti, L. La Monica, M. Venanzi, A. Froiio, S. Nardis, C. Di Natale, E. Martinelli, and A. D'Amico, *Chemistry-a European Journal*, *8*, 2476 (2002).

96. S. C. Ng, T. Sun, and H. S. O. Chan, *Tetrahedron Letters*, *43*, 2863 (2002).

97. C. Madec, J. Lauransan, and C. Garrigoulagrange, *Canadian Journal of Spectroscopy*, *25*, 47 (1980).

98. M. H. Dishner, M. M. Ivey, S. Gorer, J. C. Hemminger, and F. J. Feher, *Journal of Vacuum Science & Technology a-Vacuum Surfaces and Films*, *16*, 3295 (1998).

99. H. Ron, S. Matlis, and I. Rubinstein, *Langmuir*, *14*, 1116 (1998).

100. L. J. Basile and J. R. Ferraro, *Fourier transform infrared spectroscopy*, Academic Press, New York, 1978.

101. G. J. Leggett, M. C. Davies, D. E. Jackson, and S. J. B. Tendler, *Journal of Physical Chemistry*, *97*, 5348 (1993).

102. R. Jordan, A. Ulman, J. F. Kang, M. H. Rafailovich, and J. Sokolov, *Journal of the American Chemical Society*, *121*, 1016 (1999).

103. G. E. Poirier, T. M. Herne, C. C. Miller, and M. J. Tarlov, *Journal of the American Chemical Society*, *121*, 9703 (1999).

104. W. J. Miller, Abbott, N.L., *Langmuir*, *13* (1997).

105. R. G. Chapman, E. Ostuni, L. Yan, and G. M. Whitesides, *Langmuir*, *16*, 6927 (2000).

106. T. Kakiuchi, M. Iida, N. Gon, D. Hobara, S. Imabayashi, and K. Niki, *Langmuir*, *17*, 1599 (2001).

107. N. J. Brewer, B. D. Beake, and G. J. Leggett, *Langmuir*, *17*, 1970 (2001).

108. S. Imabayashi, D. Hobara, and T. Kakiuchi, *Langmuir*, *17*, 2560 (2001).

109. D. Losic, J. G. Shapter, and J. J. Gooding, *Langmuir*, *17*, 3307 (2001).

110. S. Imabayashi, M. Iida, D. Hobara, Z. Q. Feng, K. Niki, and T. Kakiuchi, *Journal of Electroanalytical Chemistry*, *428*, 33 (1997).

111. L. Dziri, B. Desbat, and R. M. Leblanc, *Journal of the American Chemical Society*, *121*, 9618 (1999).

112. F. Ronzon, B. Desbat, J. P. Chauvet, and B. Roux, *Colloids and Surfaces B-Biointerfaces*, *23*, 365 (2002).

113. J. M. Chalmers and P. R. Griffiths, *Handbook of vibrational spectroscopy*, J. Wiley, New York, 2002.

114. K. W. Hipps and G. A. Crosby, *Journal of Physical Chemistry*, *83*, 555 (1979).

115. D. D. Popenoe, S. M. Stole, and M. D. Porter, *Applied Spectroscopy*, *46*, 79 (1992).

116. B. J. Barner, M. J. Green, E. I. Saez, and R. M. Corn, *Analytical Chemistry*, *63*, 55 (1991).

117. T. Buffeteau, B. Desbat, and J. M. Turlet, *Applied Spectroscopy*, *45*, 380 (1991).

118. International Summer Course on Material Science Antwerp 1969 and S. Amelinckx, *Modern diffraction and imaging techniques in material science. Proceedings of the International Summer Cource on Material Science, held at Antwerp, Belguim, 28 July-8 August 1969, and sponsored by NATO Scientific Affairs Division. Editors: S. Amelinckx, R. Gevers, G. Rremaut [and others]*, North-Holland Pub. Co., Amsterdam, 1970.

119. R. J. Fessenden and J. S. Fessenden, *Organic chemistry*, Pacific Grove, CA, 1990.

120. P. E. Laibinis, G. M. Whitesides, D. L. Allara, Y. T. Tao, A. N. Parikh, and R. G. Nuzzo, *Journal of the American Chemical Society*, *113*, 7152 (1991).

121. P. Tarakeshwar and S. Manogaran, *Spectrochimica Acta Part a-Molecular and Biomolecular Spectroscopy*, *51*, 925 (1995).

122. A. Fernandez-Ramos, E. Cabaleiro-Lago, J. M. Hermida-Ramon, E. Martinez-Nunez, and A. Pena-Gallego, *Journal of Molecular Structure-Theochem*, *498*, 191 (2000).

123. V. S. Yadava and V. M. Padmanabhan, *Pramana*, *6*, 94 (1976).

124. A. G. Saraf, K. B. Saraf, P. A. Wani, and Bhoraskar, *Crystal Research and Technology*, *21*, 375 (1986).

125. B. R. Heywood and S. Mann, *Chemistry of Materials*, *6*, 311 (1994).

126. J. Aizenberg, A. J. Black, and G. M. Whitesides, *Nature*, *398*, 495 (1999).

127. M. Fix, R. Lauter, C. Lobbe, G. Brezesinski, and H. J. Galla, *Langmuir*, *16*, 8937 (2000).

128. S. De Feyter, A. Gesquiere, P. C. M. Grim, F. C. De Schryver, S. Valiyaveettil, C. Meiners, M. Sieffert, and K. Mullen, *Langmuir*, *15*, 2817 (1999).

129. A. Kuhnle, T. R. Linderoth, B. Hammer, and F. Besenbacher, *Nature*, *415*, 891 (2002).

130. J. P. M. Lommerse, S. L. Price, and R. Taylor, *Journal of Computational Chemistry*, *18*, 757 (1997).

131. E. Delamarche, B. Michel, C. Gerber, D. Anselmetti, H. J. Guntherodt, H. Wolf, and H. Ringsdorf, *Langmuir*, *10*, 2869 (1994).

132. V. S. Yadava and Padmanab.Vm, *Acta Crystallographica Section B-Structural Science*, *B 29*, 493 (1973).

133. P. J. J. A. Buijnsters, J. J. J. M. Donners, S. J. Hill, B. R. Heywood, R. J. M. Nolte, B. Zwanenburg, and N. A. J. M. Sommerdijk, *Langmuir*, *17*, 3623 (2001).

134. L. Pasteur, *Ann Phys*, *24*, 442 (1848).

135. N. Bouropoulos, S. Weiner, and L. Addadi, *Chemistry-a European Journal*, *7*, 1881 (2001).

136. J. Kuther, R. Seshadri, G. Nelles, W. Assenmacher, H. J. Butt, W. Mader, and W. Tremel, *Chemistry of Materials*, *11*, 1317 (1999).

137. J. Kuther and W. Tremel, *Chemical Communications*, 2029 (1997).

138. L. J. Prins, F. De Jong, P. Timmerman, and D. N. Reinhoudt, *Nature*, *408*, 181 (2000).

ACS PUBLICATIONS DIVISION
JUN 23 2004
COPYRIGHT OFFICE

Karen Buehler

From: Alexandre Brolo [agbrolo@uvic.ca]
Sent: Tuesday, June 22, 2004 5:47 PM
To: copyright@acs.org

Dear Sir/Madam,

We would like to request permission to include a Figure from a Journal of the American Chemical Society paper in the introduction of a M.Sc. dissertation. Here are all the pertinent information:

Dissertation title: "Crystallization of Diammonium Tartrates on Self-Assembled Monolayers of Cysteines on Au (111)"
Student Name: Kelly Hannah
Supervisor: Alexandre G. Brolo
Place: Department of Chemistry, University of Victoria
We would like to use Figure 7 (page 4505) from the following reference:
Aizenberg, J.; Black, A. J.; Whitesides, G. H. *J Am Chem Soc* 1999, *121*, 4500-4509.

All my mailing information and fax number are given below.

Alexandre G. Brolo
Department of Chemistry
University of Victoria
P.O.Box 3065, Victoria, BC, Canada,
V8W 3V6
Phone: (250) 721 7167
FAX: (250) 721 7147

Thanks in advance,

Alexandre G. Brolo

Alexandre G. Brolo
Assistant Professor (Physical/Analytical Chemistry)
Department of Chemistry
University of Victoria
P.O.Box 3065, Victoria, BC, Canada,
V8W 3V6
Phone: (250) 721 7167
FAX: (250) 721 7147
http://www.chemistry.uvic.ca/brolo/brolo.html

PUBLICATIONS
Division
ACS
1156 - 16th St., N.W.
Washington, DC 20036

PERMISSION TO REPRINT IS GRANTED BY THE AMERICAN CHEMICAL SOCIETY

ACS COPYRIGHT CREDIT LINE REQUIRED. Please follow this sample: Reprinted with permission from (reference citation). Copyright (year) American Chemical Society.

APPROVED BY_
ACS Copyright Office

6-23-04

☐ If this box is checked, author permission is also required. See original article for address.